Department of Geomatics Engineering

Low-Cost Digital Cameras: Calibration, Stability Analysis, and Applications

(URL: http://www.geomatics.ucalgary.ca/links/GradTheses.html)

by

Anoop Pullivelli

April 2005

UNIVERSITY OF
CALGARY

UNIVERSITY OF CALGARY

Low-Cost Digital Cameras: Calibration, Stability Analysis, and Applications

by

Anoop Manohar Pullivelli

A THESIS

SUBMITTED TO THE FACULTY OF GRADUATE STUDIES

IN PARTIAL FULFILMENT OF THE REQUIREMENTS FOR THE

DEGREE OF MASTER OF SCIENCE

DEPARTMENT OF GEOMATICS ENGINEERING

CALGARY, ALBERTA

APRIL, 2005

ABSTRACT

Increasing resolution and reducing cost of off-the-shelf digital cameras are giving rise to their utilization in traditional and new photogrammetric activities, and allowing amateur users to generate high-quality photogrammetric products. For most, if not all photogrammetric applications, the internal metric characteristics of the implemented camera, customarily known as the Interior Orientation Parameters (IOP), need to be determined and analyzed. The derivation of these parameters is usually achieved by implementing a bundle adjustment with self-calibration procedure.

The stability of the IOP is an issue in digital cameras since they are not built with photogrammetric applications in mind. This thesis introduces four quantitative methods for testing camera stability, where the degree of similarity between reconstructed bundles from two sets of IOP is evaluated. The experiments conducted in this research demonstrate the stability of several digital cameras. In addition, the need for different stability analysis measures for different geo-referencing techniques will be demonstrated. Some potential applications of low-cost digital cameras involving 3-D object space reconstruction will also be discussed.

ACKNOWLEDGEMENTS

DEDICATION

I would like to dedicate this work to my family, especially my parents, and my fiancé. Their support, encouragement, and understanding have been monumental during the course of my education.

TABLE OF CONTENTS

LIST OF TABLES

LIST OF FIGURES AND ILLUSTRATIONS

LIST OF SYMBOLS

x_A, y_A — Observed image coordinates of an image point

X_A, Y_A, Z_A — Ground coordinates of an object point

X_0, Y_0, Z_0
ω, φ, κ — Exterior Orientation Parameters (EOP) − X_0, Y_0 and Z_0 represent the position of perspective center with respect to the ground coordinate system, where ω, φ and κ represent the rotation angles between the ground and image coordinate systems

x_p, y_p, c — Calibrated principal point position and principal distance of the camera with respect to the image coordinate system

K_1, K_2 — Radial lens distortion parameters

P_1, P_2 — De-centric lens distortion parameters

A_1, A_2 — Affine deformation parameters

$r_{11}, r_{12}, ..., r_{33}$ — Elements of a rotation matrix that are a function of ω, φ, κ

σ_o — Square root of the variance component from a least squares adjustment

LIST OF ABBREVIATIONS

2-D	Two Dimensional
3-D	Three Dimensional
CCD	Charge Coupled Device
DEM	Digital Elevation Models
EOP	Exterior Orientation Parameters
GCP	Ground Control Point
GPS	Global Positioning System
INS	Inertial Navigation System
IOP	Interior Orientation Parameters
MIS	MISclosure similarity measure
RMSE	Root Mean Square Error
ROT	ROTation similarity measure
SPR	Single Photo Resection similarity measure
ZROT	Zero ROTation similarity measure

CHAPTER 1

INTRODUCTION

1.1 Background

The fundamental objective of photogrammetry is to generate three-dimensional spatial and descriptive information from two-dimensional imagery. Reliable and accurate recovery of three-dimensional information from imaging systems requires accurate knowledge of the internal characteristics of the involved camera. These characteristics, customarily known as the Interior Orientation Parameters (IOP), include the focal length of the camera, coordinates of the principal point, and distortion parameters. To determine the IOP, a bundle adjustment with self-calibration is the commonly employed technique. The calibration procedure requires control information, which is usually available in the form of a test field. Traditional calibration test fields consist of distinct and specifically marked targets (Fryer, 1996). Alternatively, other techniques have been developed for camera calibration using a test field comprised of linear features. The utilization of linear features for camera calibration provides a means to easily establish the calibration test field, to automatically extract the linear features from digital imagery, and to derive the distortions associated with the implemented camera by observing deviations from

straightness in the captured imagery of object space straight lines (Habib and Morgan, 2003).

Since its inception, the use of film/analog metric cameras has been the norm in photogrammetric applications. However, the role of digital cameras in such applications has been rising along with its rapid development, ease of use, and availability. Analog metric cameras, which are solely designed for photogrammetric applications, proved to possess a strong structural relationship between the elements of the lens system and the focal plane. Practical experience with these cameras showed that they maintain the stability of their IOP over an extended period of time. On the other hand, the majority of commercially available digital cameras are not designed with photogrammetric applications in mind. Therefore, the stability of their internal characteristics should be carefully examined prior to their use in photogrammetric applications. This thesis will present four methodologies for comparing two sets of IOP of the same camera that have been derived from two calibration sessions. The objective of the presented methodologies is to decide whether the two IOP sets are equivalent or not. It should be noted that these methodologies are general enough that they are applicable for stability analysis of analog and digital cameras.

1.2 Scope of Research

The primary purpose of the research is to establish the practical use of off-the-shelf digital cameras by introducing innovative methodologies for the stability analysis of such cameras, conducting experiments with them, and using them in potential applications.

The following points reveal the central objectives of the research required to fulfill the goals of this thesis work.

Objective 1 – Describe the process of camera calibration:

Calibration is used to model and estimate the IOP of a camera, which is required to generate three-dimensional information. In traditional camera calibration activities, control information takes the form of distinct and specifically marked points/targets. A description of this traditional approach as well as the drawbacks of implementing such control will be presented. As an alternative for representing control, a calibration test field consisting of straight lines is used in this research. Several approaches for the representation and utilization of straight lines that have been proposed in literature will be discussed. A mathematical model that incorporates overlapping images with straight line features in a bundle adjustment with self-calibration process will be described. Furthermore, an explanation of how linear features are incorporated in the calibration process will be provided by describing the process of selecting end and intermediate points along the line, the optimal configuration of the lines, and the linear feature extraction process.

Objective 2 – Present new bundle comparison methodologies for analyzing the stability of cameras:

A point of concern in the camera calibration process is the reliability of the estimated IOP. Professional mapping cameras have been designed and built to assure the utmost stability of their internal characteristics over a long period of time. However, in the case

of low-cost digital cameras, their internal characteristics are not given due consideration by the manufacturers. They are designed with amateur applications in mind and hence, the stability of the IOP of these cameras cannot be guaranteed. Therefore, the stability of their internal characteristics needs to be analyzed prior to their use in photogrammetric applications. Since there are no established procedures and standards for evaluating the stability of the IOP, this research focused on developing stability analysis procedures that would be meaningful from a photogrammetric point of view.

Before these proposed measures of stability are described, a basic statistical approach for comparing two sets of IOP derived from two calibration sessions and its drawbacks will be presented. Then the thesis will focus on introducing the four new meaningful, quantitative methods, which are based on evaluating the degree of similarity between two reconstructed bundles that are generated from two sets of IOP. Each method has its own advantages and disadvantages, which will also be explained. The described stability measures are general enough that they can be applied to digital as well as analog cameras.

Objective 3 – Present results of conducted calibration and stability analysis tests:

In this research, a few digital cameras have been calibrated and evaluated for stability over a significant period of time. This thesis will provide these stability results and an analysis of the tested cameras as well as discuss the factors affecting the calibration and stability of their IOP. Additionally, the IOP sets will be compared using three of the four proposed similarity measures. The reason why one measure is not implemented is because it assumes the same principal distance for the two sets of IOP being compared. Furthermore, estimated IOP sets derived from image datasets acquired on the same day

will be compared against different calibration conditions. These conditions involve changing certain settings on the camera (like the focusing method), changing the size of the test field, and altering the number of estimated parameters in the calibration procedure. Based on the experiments conducted, some tips and precautions on performing the calibration and stability analysis will also be presented.

Objective 4 – Discuss stability analysis requirements for different geo-referencing techniques:

The use of different stability analysis methods for direct and indirect geo-referencing techniques will be described. Since direct geo-referencing will introduce constraints regarding the position and attitude of the defined bundles in space, a specific stability analysis method will be applicable depending on the constraints. This idea will be confirmed through experiments involving simulations of an image block using a pre-defined object space and one set of IOP; a reconstruction of the object space using the simulated image block and a different set of IOP; and a comparison of the true object space and the reconstructed one. The thesis will essentially test the hypothesis that using a certain IOP set in the reconstruction procedure will yield an object space whose quality is dependent on the degree of similarity between the IOP set used in simulation and the IOP set used in reconstruction.

Objective 5 – Discuss potential applications:

In this research, a few applications involving the implementation of low-cost digital cameras for 3-D object space reconstruction have been investigated. These applications

necessitate the use of camera calibration and stability analysis measures prior to the recovery of 3-D information and include:

- Generation of 3-D CAD models of a building for archiving

- Measurement of facial features for personal identification

- Photogrammetric measurements used for medical applications like the reconstruction of a human torso for spinal disorders, the measurement of wounds and fixed implant prosthesis

The process of calibration and stability analysis of the implemented cameras is required because the accuracy of the reconstruction is dependent on the accuracy and reliability of the camera's IOP.

1.3 Thesis Outline

The entire thesis is divided into seven chapters. The following list describes the contents of the remaining chapters:

- Chapter 2: Literature Review – A review of some published work related to the thesis topic will be presented, which will include a description of self-calibration distortion models, traditional approaches of calibration, different methods of representation and utilization of straight line features, and a calibration approach where object space straight lines are utilized in a bundle adjustment with self-calibration procedure.

- Chapter 3: Stability Analysis – This chapter will outline the basic methodology for stability analysis using statistical testing, as well as the four proposed methodologies where the degree of similarity is evaluated between reconstructed bundles using two sets of IOP.

- Chapter 4: Experiments and Results – This chapter will provide a description of the test field, the cameras employed in the experiments and the software programs that are used in the calibration and stability analysis process. In addition, an analysis of the experimentation results will also be included.

- Chapter 5: Direct/Indirect Geo-referencing – This chapter will verify the need for different stability analysis measures for different geo-referencing techniques.

- Chapter 6: Applications – This chapter will discuss a few potential applications of low-cost digital cameras involving the calibration and stability analysis of digital cameras.

- Chapter 7: Conclusions and Future Work – A summary of the methodologies and research work will be provided along with some recommendations of future research.

CHAPTER 2

LITERATURE REVIEW

2.1 Introduction

The primary purpose of camera calibration is to determine numerical estimates of the interior orientation parameters of the implemented camera. The interior orientation corresponds to the principal distance (c), location of the principal point (x_p, y_p), and image coordinate corrections that compensate for various deviations from the assumed perspective geometry, which together are known as the IOP of the camera. The image coordinate corrections are modeled as distortion parameters and are described in Section 2.2. The traditional approaches of calibration, which involve the utilization of point targets as a source of control, are then described in Section 2.3. A calibration test field consisting of points is hard to establish and maintain, and requires professional surveyors. For this reason, the calibration test field implemented in this research involves the utilization of linear features. Section 2.4 will look into the advantages of incorporating linear features, various calibration methodologies that utilize straight lines, different methods of representing straight lines, and a mathematical model that incorporates overlapping images with straight line features in a bundle adjustment with self-calibration

procedure (Habib et al., 2002-a). The configuration of the lines in the calibration test field is also an important consideration since it affects the accurate recovery of the distortion parameters being estimated. Thus, an optimal configuration of the straight lines for an effective estimation of the distortion parameters will be put forward. Finally, the automated process of extracting linear features from the imagery will be described in complete detail.

2.2 Calibration Distortion Models

As mentioned above, the IOP consists of the focal length, principal point coordinates, and image coordinate corrections that compensate for various deviations from the assumed perspective geometry. The perspective geometry is established by the collinearity condition, which states that the perspective center, the object point and the corresponding image point must be collinear (Kraus, 1993). A distortion in the image signifies that there is a deviation from collinearity. Potential sources of the deviation from collinearity are the radial lens distortion, de-centric lens distortion, atmospheric refraction, affine deformations and out-of-plane deformations (Fraser, 1997). All these sources of distortion are represented by explicit mathematical models whose coefficients are called the distortion parameters (e.g., K_1, K_2, K_3... for radial lens distortion, P_1, P_2, P_3 for de-centric lens distortion, and A_1, A_2 for affine deformations).

Radial lens distortion (RLD):

The radial lens distortion occurs when the path of a light ray is altered as it passes through the perspective center of the lens. It is caused by large off-axial angles and lens

manufacturing flaws, and takes place along a radial direction from the principal point. The correction for the radial distortion of the measured point is modeled by the polynomial series in the following equations (Kraus, 1997):

$$\Delta x_{RLD} = K_1(r^2 - 1)x + K_2(r^4 - 1)x + K_3(r^6 - 1)x + ...$$
$$\Delta y_{RLD} = K_1(r^2 - 1)y + K_2(r^4 - 1)y + K_3(r^6 - 1)y + ...$$

(2.1)

Where: $r = \sqrt{(x - x_p)^2 + (y - y_p)^2}$, K_1, K_2 and K_3 are the radial lens distortion parameters, x_p and y_p are the image coordinates of the principal point, and x and y are the image coordinates of the measured point. The K_1 term alone will usually suffice in medium accuracy applications and for cameras with a narrow angular field of view. The inclusion of K_2 and K_3 terms might be required for higher accuracy and wide-angle lenses. The decision as to whether incorporate one, two, or three radial distortion terms can be based on statistical tests of significance (Habib et al., 2002-b). Another reason why estimating only K_1 would be preferable is that estimating more than the required amount of distortion parameters could increase the correlation between unknown parameters and this will likely affect the IOP estimates.

De-centric lens distortion (DLD):

The de-centric lens distortion is caused by inadequate centering of the lens elements of the camera along the optical axis. The misalignment of the lens components causes both radial and tangential distortions, which can be modeled by the following correction equations (Brown, 1966):

$$\Delta x_{DLD} = P_1(r^2 + 2x^2) + 2P_2xy$$
$$\Delta y_{DLD} = P_2(r^2 + 2y^2) + 2P_1xy$$

(2.2)

Where: P_1 and P_2 are the de-centric lens distortion parameters.

Atmospheric refraction (AR):

Atmospheric refraction occurs when a light ray from the object point to the perspective center passes through atmospheric layers that vary in temperature, pressure and humidity. To remove the effect of atmospheric refraction, standard correction formulas are applied to the image measurements prior to the adjustment. If there are any remaining atmospheric refraction effects in the measurements, it can be compensated for by the radial lens distortion coefficients in view of the fact that both distortions occur along the radial direction.

Affine deformations (AD):

Affine deformations are deformations that occur in the focal plane and usually originate from non-uniform scaling along the x and y directions, and sometimes from non-orthogonality between the x-y axes. They could be caused by non-square pixels, which will lead to scale differences if considered square, and by the non-orthogonality of the rows and columns in the CCD array. The correction equations for affine deformations are:

$$\Delta x_{AD} = -A_1x + A_2y$$
$$\Delta y_{AD} = A_1y$$

(2.3)

Where: A_1 corresponds to half of the scale difference along the x and y axes, and A_2 represents the non-orthogonality angle.

The relative magnitude of the distortions listed above is an indication of the condition and quality of the camera. The mathematical model equations that represent the combination of the distortions are:

$$\Delta x = \Delta x_{RLD} + \Delta x_{DLD} + \Delta x_{AR} + \Delta x_{AD} + ...$$
$$\Delta y = \Delta y_{RLD} + \Delta y_{DLD} + \Delta y_{AR} + \Delta y_{AD} + ...$$

(2.4)

Where: Δx and Δy are the total compensations for the various distortions. During experimentation, different combinations of distortion parameters are included in the calibration. The number of included parameters will depend on the type of camera implemented and the accuracy required for the intended application.

2.3 Traditional Calibration Approach

Camera calibration requires control information, which is usually available in the form of a test field. Traditional calibration test fields consist of distinct and specifically marked points or targets (Fryer, 1996), Figure 2.1. These targets are established and precisely measured in a test field using surveying techniques. The number and distribution of the targets are vital for the recovery of the IOP of the implemented camera.

Figure 2.1: Traditional calibration test field

In traditional camera calibration, convergent imagery is acquired over a test field. A large number of control points on the test field are measured in the image space along with common points in overlapping imagery, which are otherwise known as tie points. The extended collinearity equations (Equations 2.5) are used to define the relationship between image and ground coordinates of a point in the image. They are used in a bundle adjustment with self-calibration to solve for the object coordinates of the tie points, the exterior orientation parameters of the involved imagery, and the interior parameters of the involved camera (Kraus, 1993; Habib et al., 2002-b).

$$
\begin{aligned}
x_a &= x_p - c \frac{r_{11}(X_A - X_O) + r_{21}(Y_A - Y_O) + r_{31}(Z_A - Z_O)}{r_{13}(X_A - X_O) + r_{23}(Y_A - Y_O) + r_{33}(Z_A - Z_O)} + \Delta x \\
y_a &= y_p - c \frac{r_{12}(X_A - X_O) + r_{22}(Y_A - Y_O) + r_{32}(Z_A - Z_O)}{r_{13}(X_A - X_O) + r_{23}(Y_A - Y_O) + r_{33}(Z_A - Z_O)} + \Delta y
\end{aligned}
\tag{2.5}
$$

Where:

x_a and y_a are the observed image coordinates of an image point a,

X_A, Y_A and Z_A are the ground coordinates of the corresponding object point A,

Δx and Δy are image coordinate corrections (See Equations 2.4),

x_p, y_p and c are the principal point coordinates and principal distance of the camera,

X_O, Y_O, Z_O are the object coordinates of the perspective center of the camera, and

r_{11}, $r_{12}\dots$, r_{33} are the elements of a rotation matrix that are a function of the rotation angles ω, φ and κ.

2.4 Calibration Approach using Linear Features

A major drawback of establishing and maintaining a conventional calibration test field as well as carrying out the calibration procedure is that it requires professional surveyors and photogrammetrists. Since establishing and maintaining such a test field is an expensive procedure, an alternative approach for camera calibration using an easy-to-establish test field comprised of a group of straight lines as well as some tie points is implemented in this research, Figure 2.2 (Habib and Morgan, 2004). Points are also included in this test field to establish the scale in the datum for the calibration process by incorporating distance measurements between any two points.
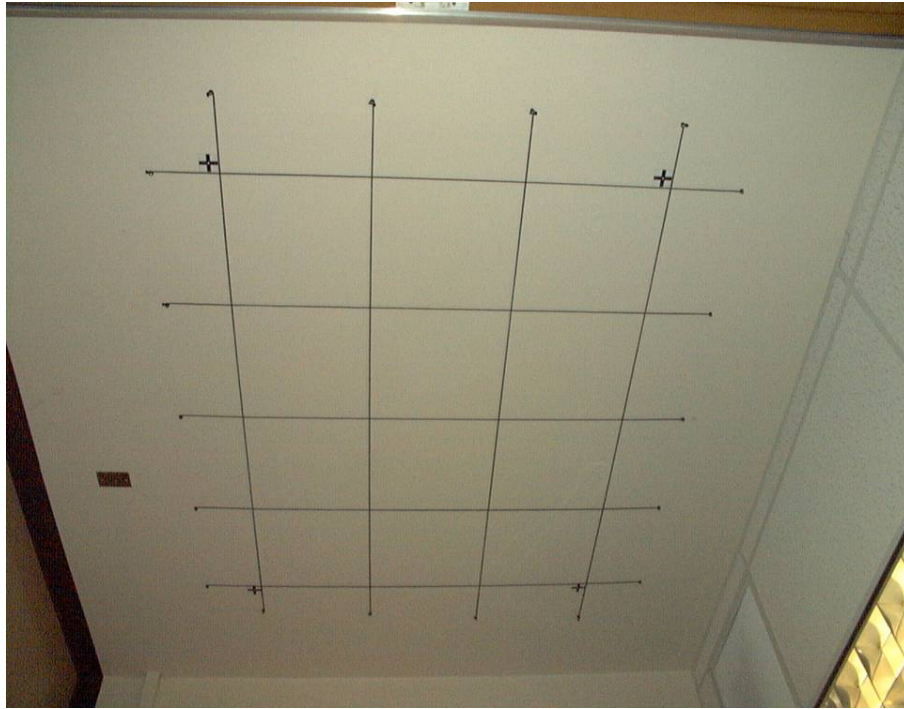
Figure 2.2: New camera calibration test field consisting of straight lines

Using straight line features as an alternative for representing control information in a calibration test field is not a relatively new concept. They offer several advantages over utilizing point targets. They can be easily established in a calibration test field. Corresponding lines in the image space can be precisely extracted using image-processing techniques such as image resampling and application of edge detection filters. Furthermore, linear features, which essentially consist of a set of connected points, increase the system redundancy and consequently enhance the geometric strength and robustness in terms of the ability to detect blunders. For camera calibration purposes, object space straight lines will project into the image space as straight lines in the absence of distortion, Figure 2.3. Therefore, deviations from straightness in the image space can

be modeled and attributed to various distortion parameters (e.g., radial and de-centric lens distortions) in a near-continuous way along the line.
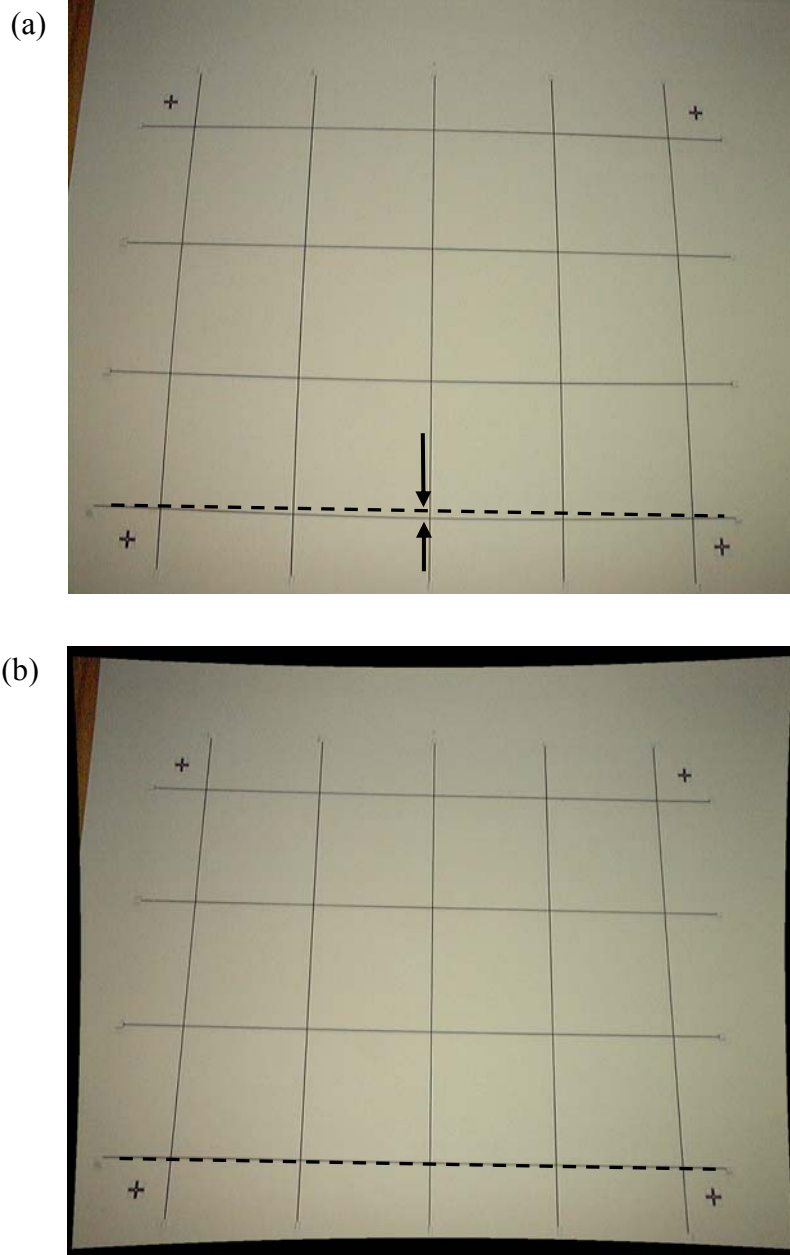
Figure 2.3: (a) An image before calibration with distortion and (b) an image after calibration without distortion

Several approaches for the utilization of straight lines have been proposed in literature and all suffer from a number of drawbacks. Brown (1971) introduced the plumb-line method, which is based on straight lines, to derive an estimate of the radial and de-centric lens distortions. The plumb-line method removes deviations from straightness in image space straight lines using radial and de-centric lens distortion models, whose parameters are estimated through an adjustment procedure. This is a rapid and practical approach for computing lens distortion parameters. However, the results would be contaminated by uncorrected systematic errors, and a separate calibration procedure for determining the principal distance and other systematic distortions such as affine deformations is still needed. Guoqing et al (1998) and Prescott and McLean (1997) used straight lines in a multi-stage calibration strategy (i.e., the IOP were sequentially estimated). Heuvel (1999-b) proposed another approach using straight lines to recover the IOP of the camera. This method can only be applied when dealing with imagery containing parallel and perpendicular lines. Similar to the plumb-line methods, the above approaches start by estimating radial and de-centric lens distortion, and then determining the principal point coordinates and the focal length. Bräuer-Burchardt and Voss (2001) developed a methodology for detecting image space circles while considering them as distorted straight lines. These circles are used later for estimating the distortion parameters. However, lens distortions do not necessarily result in a circular effect of one radius of curvature along the line. Chen and Tsai (1990) introduced another method for incorporating straight lines instead of points for camera calibration purposes. However, this approach requires the knowledge of the parametric equations of the object space straight lines, which mandates additional fieldwork.

2.4.1   Representation of Straight Lines

Prior to incorporating straight lines in the bundle adjustment procedure, the representation of the lines in the image and object space must be considered (Habib and Morgan, 2003). There are essentially three ways of representing a 3-D straight line in the object space. One approach is a six-dimensional representation where the linear features are defined as line segments (i.e. by any two points along the line). The second approach is a five-dimensional representation where object space straight lines are represented by a unit vector along the line together with a point that belongs to the line. Lastly, the third approach is to define them as infinite lines using optimal (or minimal) representation. In the optimal representation approach, only a minimal number of parameters (i.e. four parameters) are required to define the line. There are numerous alternatives of optimal representations of 3-D lines as described by the work of Roberts (1988) and Faugeras and Hebert (1986). For example, in one approach, the object space line is represented by the coordinates of a point on the line closest to the origin of the coordinate system and an angle that defines the orientation of the line with respect to a certain reference line. In the approach adopted by Faugeras and Hebert (1986), a 3-D line is represented as the intersection of two planes, Equations 2.6.

$$
\begin{aligned}
x &= az + p \\
y &= bz + q
\end{aligned}
\tag{2.6}
$$

Where the first equation represents a plane that is parallel to the x-axis, the second equation represents a plane that is parallel to the y-axis, and the 3-D line is represented by the four-dimensional vector (a, b, p, q). It can be proven that the intersection point of the

line with the X-Y plane is represented by (p, q, 0) and the direction vector of this line is represented by (a, b, 1). However, this representation is incapable of representing lines parallel to the X-Y plane since the z-component of the direction vector of such a line would be zero.

These optimal representations of an object space line as an infinite one pose a number of problems. They will always have singularities since they cannot represent all three-dimensional lines in the object space. The mathematical models that can incorporate infinite lines would require complicated algorithms for the perspective transformation between the image and object space. Hence, it would be difficult to implement such models in existing bundle adjustment programs. Furthermore, the error measures that pertain to infinite lines might be completely different from those associated with line segments, which are more relevant. Based on these drawbacks, it is imperative to consider the uniqueness and singularities of the defined object space straight lines when choosing a way to represent them.

With regard to the representation of straight lines in the image space, the formulation of the perspective transformation between corresponding object and image space straight lines depends on the image space representation methodology (Habib and Morgan, 2003). There are three ways to represent a 3-D straight line in the image space. The first method represents image space linear features with any two points along the line (i.e. line segments) while the second method represents them with polar coordinates (ρ, θ). These two methods of representation assume that a straight line in the object space will appear as a straight line in the image space. However, this will only be the case if distortions in

the image are not present. Therefore, these approaches require prior removal of various distortions, which can be determined through a calibration procedure, from the input imagery. In the third method, image space lines are represented by a sequence of points along the line. This method of representation is more convenient since it can handle raw images captured by the camera in the presence of distortions. Therefore, the distortions, which cause deviations from straightness in the image space features, can be recovered at each point along the line in a bundle adjustment with self-calibration procedure.

2.4.2   Incorporation of Linear Features in a Bundle Adjustment Procedure

The optimal representation approach was adopted by Mikhail and Weerawong (1994) who proposed a straight-line constraint, which ensures that a unit vector defining the object space line, the vector from the perspective center to a point on the object line and the vector from the perspective center to the image point are coplanar. Other literary work such as that of Mulawa and Mikhail (1988), Tommaselli and Lugnani (1988), Ayache and Faugeras (1989), Tommaselli and Tozzi (1992), Habib (1998), Heuvel (1999-a) and Tommaselli and Poz (1999), also define an object line as an infinite line segment.

For the reasons mentioned in the previous section, representing an object space straight line using two points along the line is a more convenient and suitable approach since well-defined line segments can be modelled with relatively simple perspective transformation functions between the image and object space and such a representation will have no singularity (i.e. all possible line segments in space can be represented).

Therefore, in this research, object space straight lines are incorporated in the calibration procedure by representing them with any two points along the line such as points *A* and *B* in Figure 2.4 (Habib et al., 2002-a). These points are monoscopically measured in one or two images within which this line appears (i.e. points *a'* and *b'* in Figure 2.4). The relationship between these points and the corresponding object space points is modeled by the collinearity equations. In the image space, the lines are defined by a sequence of intermediate points such as point *d* in Figure 2.4. Therefore, the distortion at each point along the line can be independently modeled. In order to restrict the points to form a straight line, a mathematical constraint is adopted to establish the perspective relationship between image and object space lines, Equation 2.7.

$$\left(\mathbf{v}_A \times \mathbf{v}_B\right) \circ \mathbf{v}_d = \left(\begin{bmatrix} X_A - X_0 \\ Y_A - Y_0 \\ Z_A - Z_0 \end{bmatrix} \times \begin{bmatrix} X_B - X_0 \\ Y_B - Y_0 \\ Z_B - Z_0 \end{bmatrix}\right) \circ \left(R(\omega, \varphi, \kappa) \begin{bmatrix} x_d - x_p - \Delta x \\ y_d - y_p - \Delta y \\ -c \end{bmatrix}\right) = 0 \quad (2.7)$$

Where: v_A and v_B are the vectors connecting the perspective center of the image and the end points A and B, respectively, along the object space line, and v_d is the vector connecting the perspective center of the image to an intermediate point (x_d and y_d) along the line in the image.

This straight-line constraint signifies that the vectors v_A, v_B and v_d are coplanar, as shown in Figure 2.4. It can be written for each intermediate point along the image line, and therefore, the number of constraints will be equal to the number of measured intermediate points along the line. The constraint will not introduce any new parameters and it essentially plays a role in the estimation of the distortion parameters.
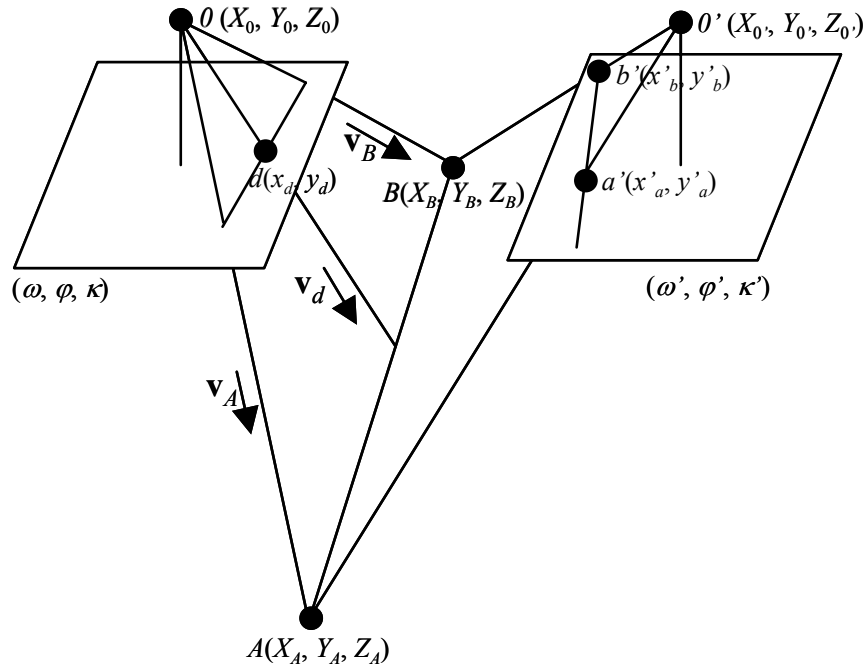
Figure 2.4: Use of the coplanarity condition for incorporating straight line features in
camera calibration

It should be noted that the recovery of object space coordinates of an end point is
dependent on the orientation of the baseline with respect to the object space line. The end
points of a line can be defined in one or two images. As shown in Figure 2.5, for each one
of these end points, the corresponding object point (A) will lie on a single infinite light
ray (v_A) defined by the perspective center (PC_{II}) and the measured image point (a). In
each of the remaining images, the perspective center (PC_I) and intermediate points (d and
e) define a plane. The coordinates of point A in the object space is derived through the
intersection of the light ray and the plane. If the light ray and the plane are coplanar, the
object point coordinates of point A cannot be recovered. This will occur if the object
space line is parallel to the baseline.
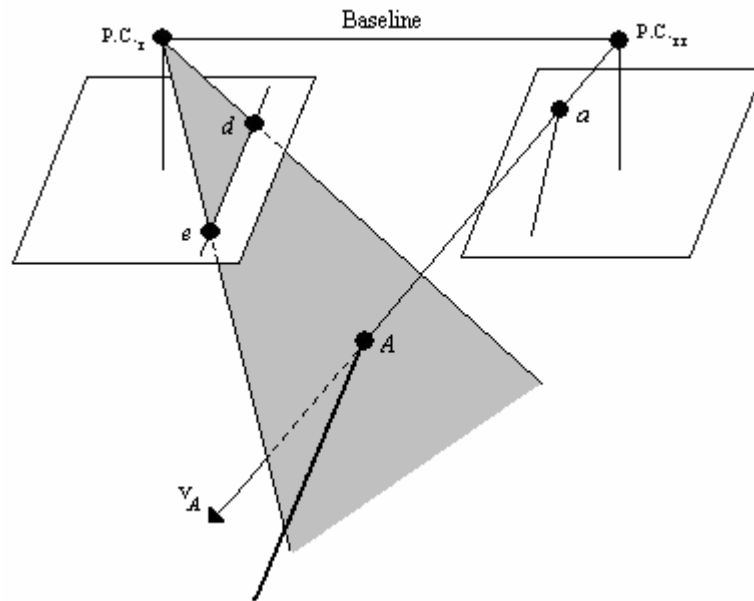
Figure 2.5: A diagram illustrating the recovery of the coordinates of an end point of a

   straight line in the object space

For self-calibration using straight lines, the end points (points *a* and *b* in Figure 2.6) can

be selected in any of the images where the straight line appears. These points need not be

identifiable or even visible in other images. Four collinearity equations will be written

using the measured end points for each line. The intermediate points (points marked with

an X in Figure 2.6) are measured in all the overlapping images and need not be conjugate.

As previously mentioned, a straight-line constraint will be written for each intermediate

point according to Equation 2.7. Figures 2.6 and 2.7 below show different scenarios for

the selection of end points. In Figure 2.6, the end points of the straight line are selected in

one image (Image 1), while in Figure 2.7, they are selected in different images (Images 1

and 4).
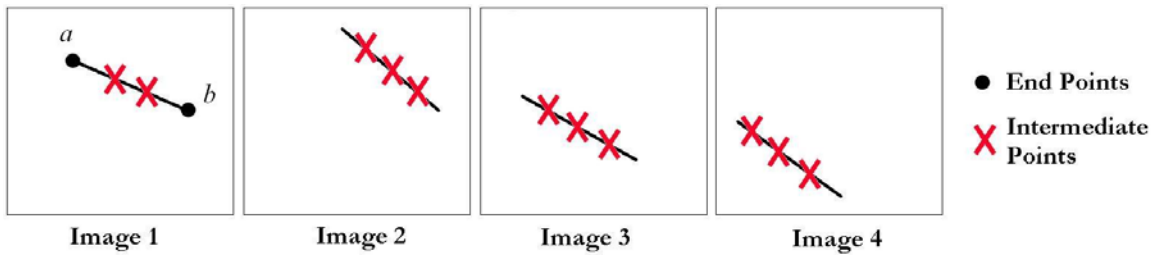
Figure 2.6: A point selection scenario where end points are chosen in just one image
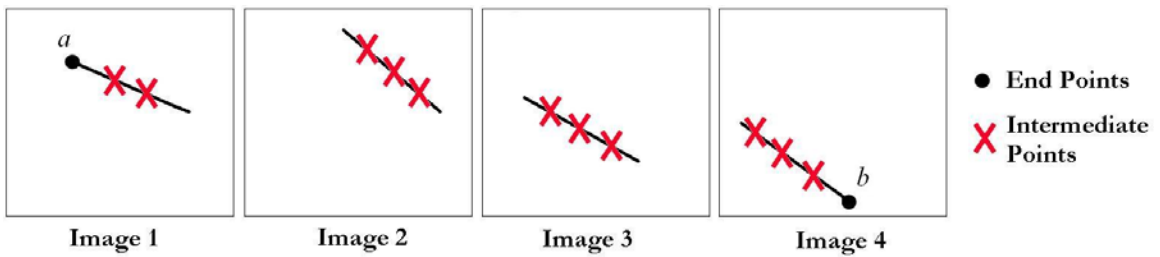
Figure 2.7: A point selection scenario where end points are chosen in two images

In a calibration test field consisting of straight lines, the configuration of the lines plays an important part in the estimation of the distortion parameters. The optimal configuration is the one that will cause more deviations from straightness in the image space (Habib et al., 2002-b). Two types of configurations of straight lines, box-type (Figure 2.8) and X-type (Figure 2.9), are used to illustrate the effects of three distortion models. From analyzing Figures 2.8 and 2.9, the box-type is the more useful configuration since it causes a larger deviation from straightness when compared to the X-type. For example, the radial lens distortion parameter can be recovered if a test field composed of a grid of straight lines is defined along the rows and columns of the captured calibration images.
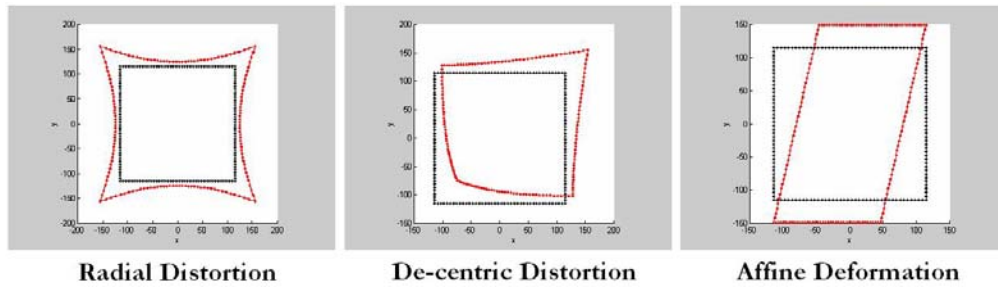
Figure 2.8: Distortions in box-type configuration of straight lines
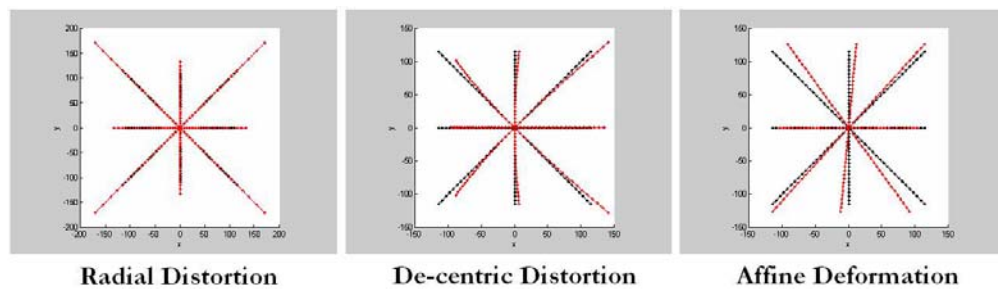
Figure 2.9: Distortions in X-type configuration of straight lines

2.4.3 Linear Feature Extraction

Automation of tasks like the extraction of linear features can be a reliable and time-saving approach in digital camera calibration. It is appealing to utilize linear features since they can be automatically and easily extracted from calibration imagery. The extraction and measurement of the end and intermediate points along the linear features in the imagery can proceed according to the following strategy (Figure 2.10 shows the original image):

i.   Resample the images to reduce their size since it helps in speeding up the extraction process, Figure 2.11.
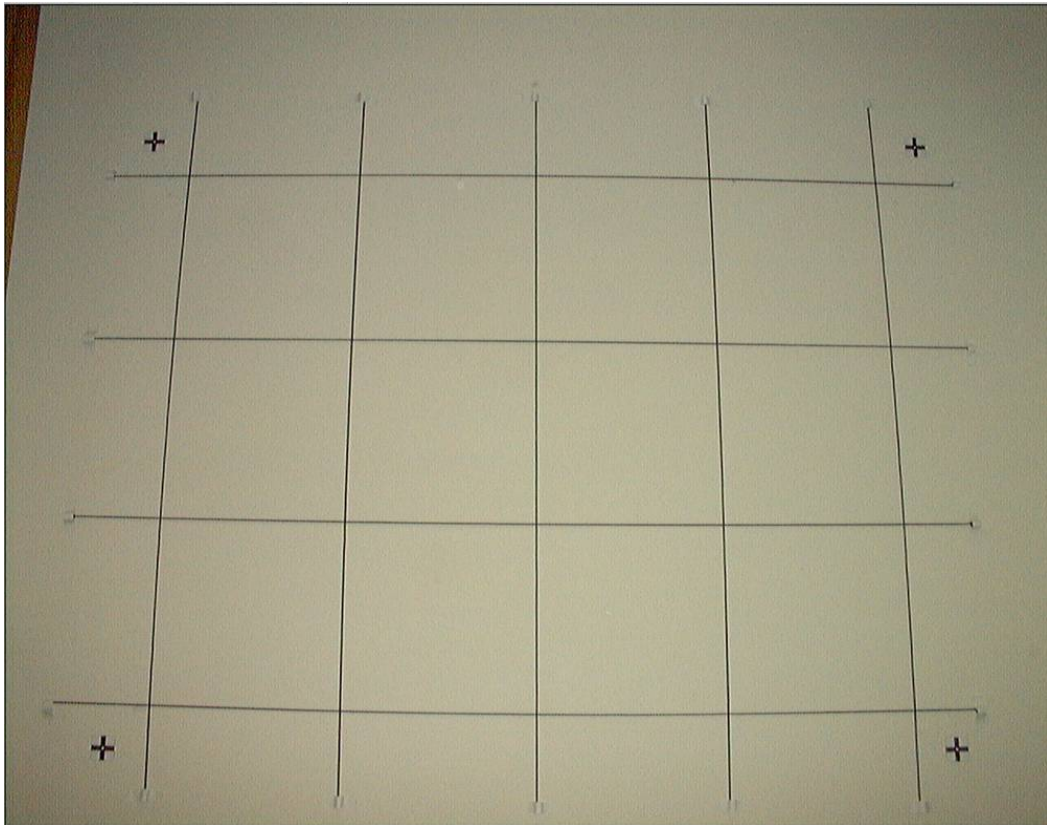
Figure 2.10: Original image captured for the purpose of camera calibration
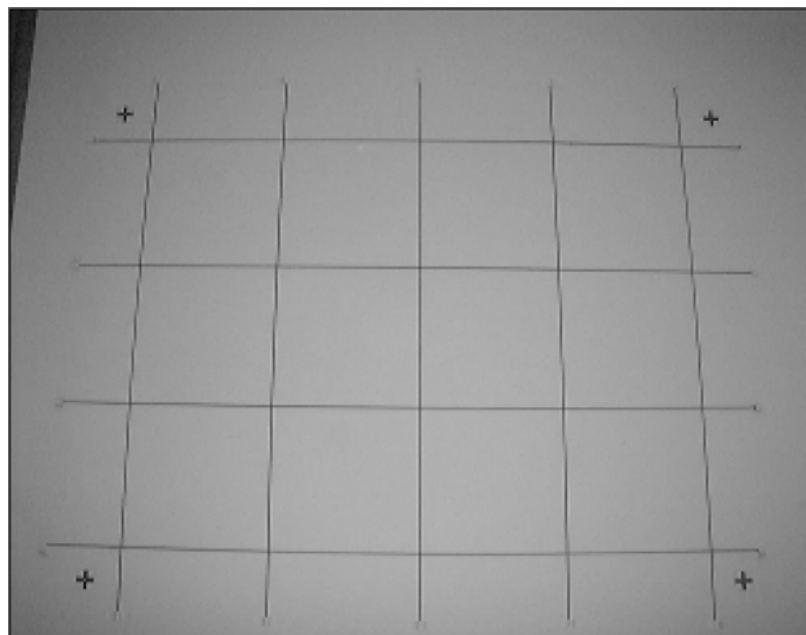
Figure 2.11: Image reduced in size through resampling

ii. Apply an edge detection operator. For example, Canny edge detection can be implemented to identify the linear features in the image (Canny, 1986), Figure 2.12.
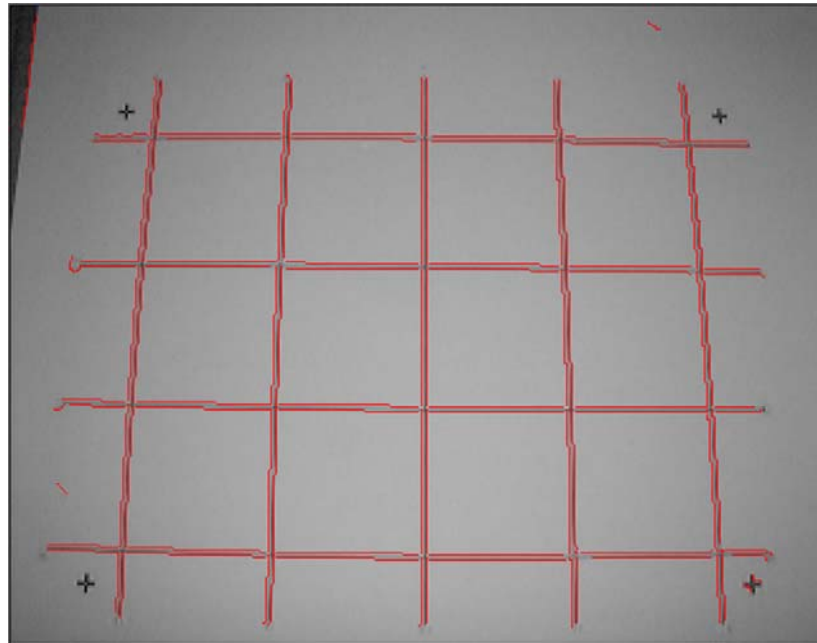
Figure 2.12: Application of a Canny edge detection operator to the Image

iii. Use a feature extraction technique called the Hough transform to identify straight lines in the image (Hough, 1962). In the procedure of the Hough transform, a parameter domain is introduced where a sinusoidal curve is used to represent the edge pixels that were extracted in step ii and these edge pixels are used to populate the parameter space, Figure 2.13. Peaks in the parameter space correspond to edge pixels along image space linear features, Figure 2.14. Due to distortions, lines with small deviations from straightness need to be found and therefore, clusters rather than well-defined peaks are sought for in the parameter space. The size of the cluster depends on the expected deviation from straightness in imagery of object space straight lines.
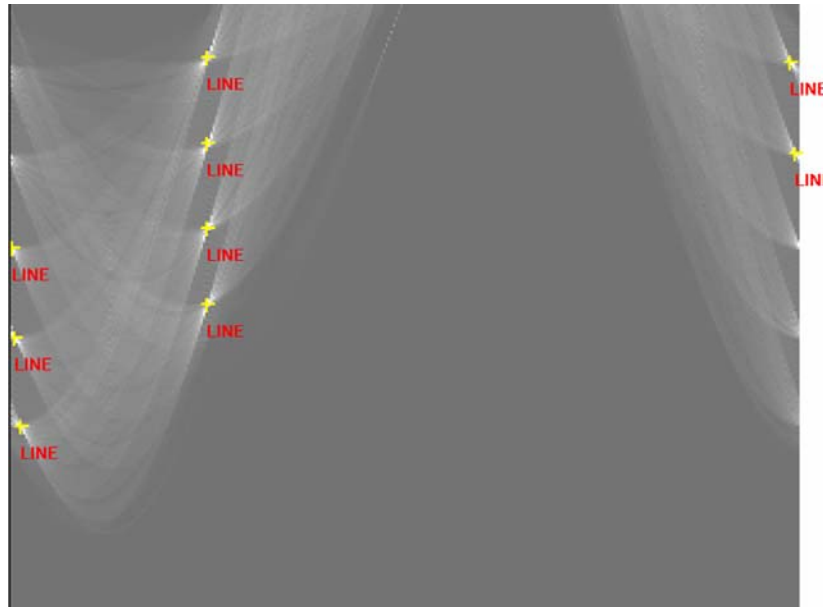
Figure 2.13: Corresponding Hough Space to the detected edges in Figure 2.12
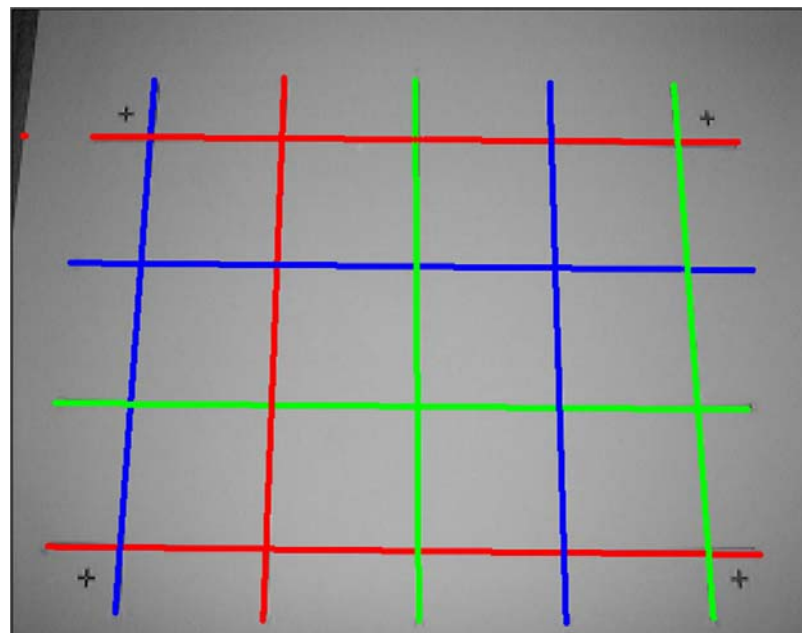
Figure 2.14: Detected straight lines as represented by the peaks in the Hough Space

iv. Establish connectivity among the involved pixels and identify the end points along

each line, Figure 2.15.
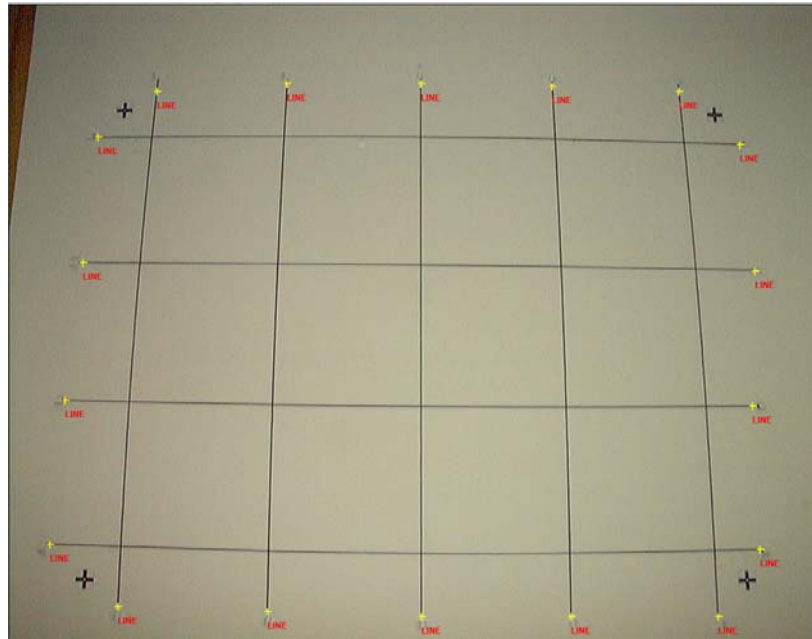
Figure 2.15: Detected end points in the image

v. In the original image at full resolution, extracted end points are then used to define a search space for the intermediate points along the lines. Profiles perpendicular to the line connecting the end points are inspected to determine the location of the intermediate points with sub-pixel accuracy by means of weighted average. Since straight lines in the test field are established by using dark ropes on a bright background, the location of the minimum gray value along the profile will be searched for (See upper left corner of Figure 2.16). By repeating this step, numerous points can be extracted along each line, Figure 2.17.
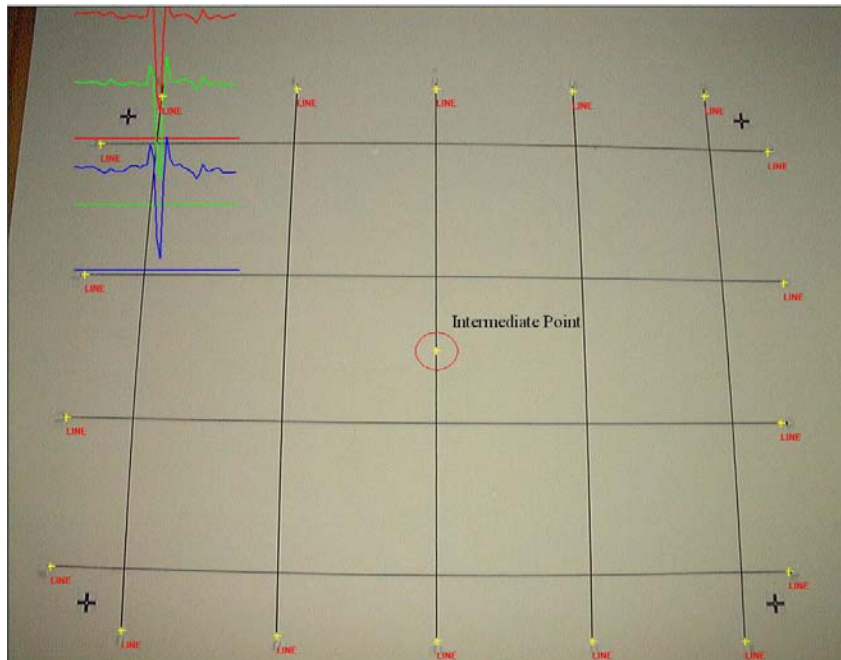
Figure 2.16: Gray value profile along an intermediate point
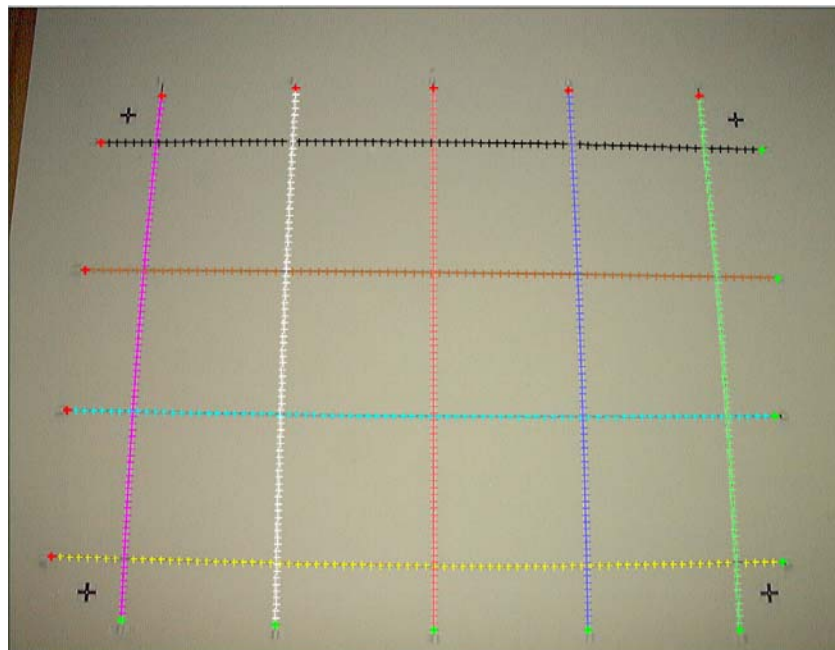
Figure 2.17: Final extracted end and intermediate points of straight lines in the image

The final extracted end and intermediate points of the lines are used in a bundle adjustment with self-calibration procedure to estimate the IOP of the camera. Once the calibration procedure has been carried out, the focus can move to the stability analysis of the implemented camera. The following chapter comprehensively discusses possible alternatives for checking camera stability by inspecting the IOP of the camera that are derived from two different calibration sessions.

CHAPTER 3

STABILITY ANALYSIS

3.1 Introduction

A point of concern in the camera calibration process is the stability of the internal geometry of the camera. If a camera is calibrated at one point in time (i.e. in one calibration session) and the derived IOP values are compared to those obtained from another calibration session, there should not be a significant difference between the two IOP sets for the camera to be considered stable. When dealing with analog metric cameras, the issue of their stability has been rarely addressed since they have been carefully designed and built to assure the utmost stability of their internal characteristics. However, the stability of digital cameras needs to be investigated since these cameras are not built with photogrammetric applications in mind and hence, the stability of the internal geometry of these cameras cannot be guaranteed. Shortis et al. (2001) described a method for evaluating digital camera stability by using the ratio of the mean precision of target coordinates to the largest dimension of the target array. However, to the best of the author's knowledge, there has not been a comprehensive study to quantify and introduce meaningful measures for analyzing the stability of digital cameras for photogrammetric

applications. This void in the literature can be attributed to the absence of standards for quantitative analysis of camera stability.

In this research, four meaningful, quantitative methods for comparing two IOP sets derived from two temporally-spaced calibration sessions are presented. The underlying concept behind camera calibration is to reconstruct a bundle of light rays that are defined by the perspective center and image points along the focal plane in such a way that it is similar to the incident bundle on the camera at the moment of exposure, Figure 3.1. Therefore, the four proposed similarity measures are based on evaluating the degree of similarity between two reconstructed bundles that are generated from two sets of IOP. However, the more straightforward and basic approach for checking camera stability can be achieved through statistical testing. The following section briefly summarizes the use of statistical testing to compare two IOP sets and reveals the drawbacks of this method.
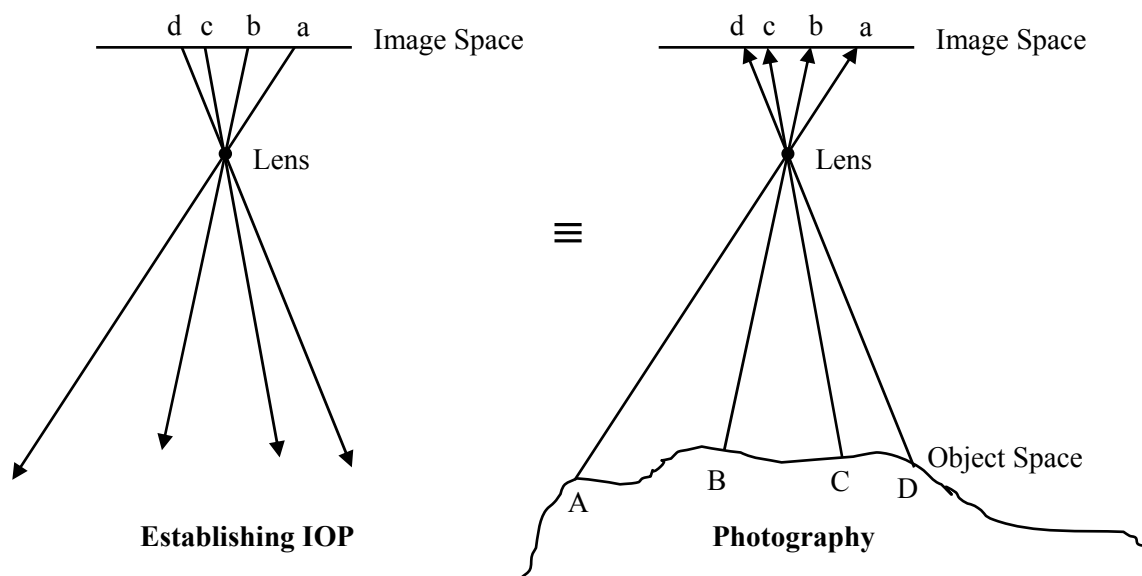
Figure 3.1: The reconstruction of a bundle of light rays, which is the basis for

establishing interior orientation for camera calibration

3.2 Statistical Testing

The statistical properties of two IOP sets can be described by an assumed normal distribution, which has a mean of the true IOP (IOP_T) of the implemented camera and can be mathematically described as:

$$IOP_I \sim (IOP_T, \Sigma_I) \text{ and } IOP_{II} \sim (IOP_T, \Sigma_{II}) \tag{3.1}$$

Where: IOP_I and IOP_{II} are the estimated IOP sets from the two calibration sessions, Σ_I and Σ_{II} are the corresponding variance-covariance matrices, and IOP_T is the true IOP.

For stability analysis, a null hypothesis (H_o) can be tested for possible rejection under the assumption that the two IOP sets are equivalent. Accepting the null hypothesis simply affirms that there is no significant difference between the two IOP sets and the internal characteristics of the camera are stable. Assuming that IOP_I and IOP_{II} are uncorrelated and that the true IOP of the camera does not change between the two calibration sessions, the null hypothesis is:

$$H_o: IOP_I = IOP_{II} \quad \text{or} \quad H_o: e = IOP_I - IOP_{II} \sim (0, \Sigma_I + \Sigma_{II}) \tag{3.2}$$

A test statistic (T), which is used to determine whether or not the null hypothesis is rejected, follows a χ^2 distribution with degrees of freedom that is equal to the rank of the matrix - $\Sigma_I + \Sigma_{II}$ (Koch, 1999). The test statistic is computed as:

$$T = e^T (\Sigma_I + \Sigma_{II})^{-1} e \tag{3.3}$$

The acceptance or rejection of the test statistic will partly depend on the assumed level of significance, which is the probability of rejecting a true null hypothesis. Assuming a certain level of significance, if the computed value is greater than the critical value (T_c) of the test statistic (i.e., $T > T_c$), the null hypothesis is rejected and hence, the two IOP sets are deemed to be significantly different from each other.

Statistical testing for the purposes of evaluating camera stability includes a number of assumptions that make it impractical to use. It assumes a normal distribution for the estimated IOP without any biases and that the variance-covariance matrices associated with the IOP sets are available, which might not be always the case (e.g., calibration certificates do not contain this information). It does not take any possible correlation between IOP and EOP into consideration. Furthermore, Habib and Morgan (2004) demonstrated that statistical testing generally gives pessimistic results for stability analysis even though the two sets of IOP may be similar from a photogrammetric point of view. Lastly, the differences in IOP should be evaluated by quantifying the discrepancy between reconstructed bundles in terms of the dissimilarity of the reconstructed object space. This will provide a more meaningful measure of the differences between the IOP sets. Due to these shortcomings of statistical testing, four alternative techniques for evaluating camera stability are utilized in this research and explained in the next section.

3.3 Similarity of Reconstructed Bundles

As mentioned earlier, the primary objective of camera calibration is to reconstruct a bundle of light rays that are defined by the perspective center and image points along the

focal plane in such a way that it is similar to the incident bundle on the camera at the moment of exposure. Therefore, stability analysis using IOP derived from different calibration sessions should be based on reconstructed bundles from connecting the perspective center to distortion-free points along the focal plane and evaluating the degree of similarity between them, Figure 3.2. In this research, four methods for evaluating the similarity are introduced. Each method constrains the position and orientation of the bundles in a certain way. These methods are explained in detail in the following sub-sections.
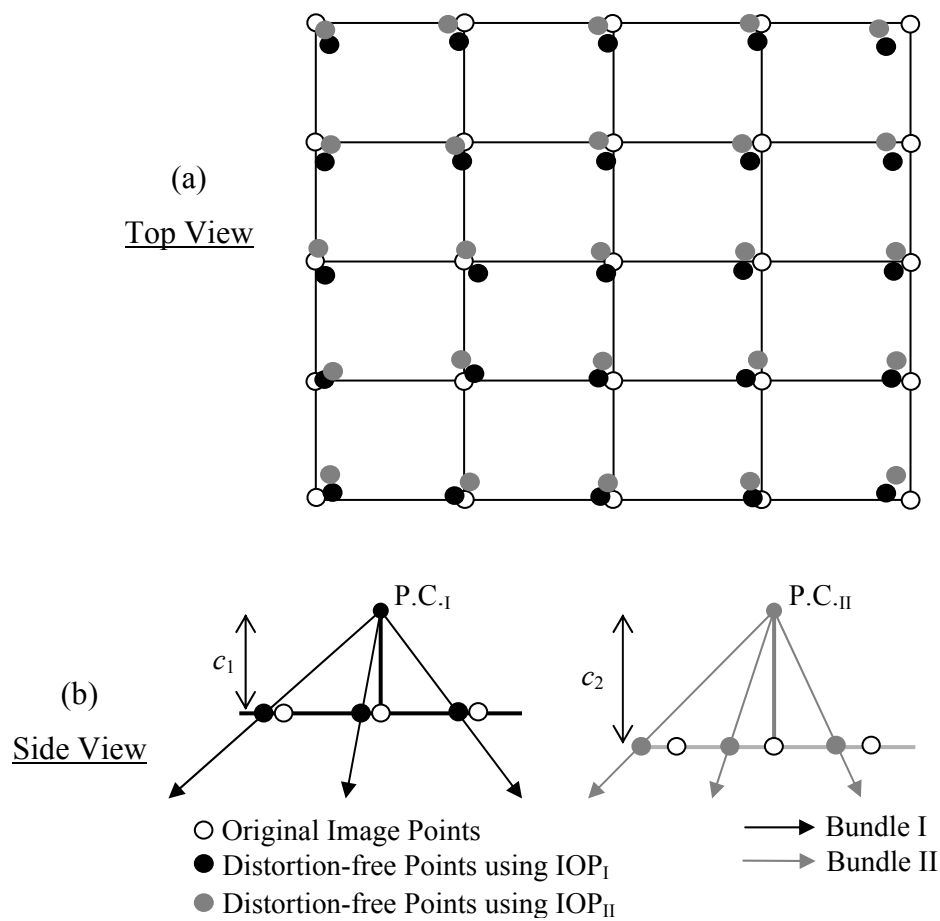
Figure 3.2: (a) Original and distortion-free image points (top view), and (b) distortion-free bundles using IOP sets derived from two calibration sessions (side view)

3.3.1   Misclosure (MIS) Method

A bundle of light rays is typically defined by the principal point coordinates, the principal distance, and points along the image plane. The Misclosure (MIS) method assumes the same principle distance for the two IOP sets being compared. Hence, the comparison is essentially confined to a two-dimensional plane that involves only the principal point coordinates and distortion parameters of the derived IOP.

The procedure starts off by first defining a synthetic regular grid in the two-dimensional image plane, Figure 3.3. The user can specify the size of the grid cells and the extent of the grid with respect to the image size. The extent of the grid is given by the percentage of the image occupied by the test field, which should optimally be at 100% in order to acquire reliable IOP estimates. If the test field does cover the entire image, the extent of the grid can be specified at 100%. However, it is difficult to have the test field occupying the entire image. Hence, the percentage for the grid extent must be specified at a value that is a balance between the optimum coverage (100%) and the true values of the coverage (which could be anywhere from 70% to 100%). Once the grid is defined, various distortions at the defined grid vertices are removed using the two sets of IOP to be compared. The result will be the creation of two distortion-free points for each grid point, Figure 3.3.
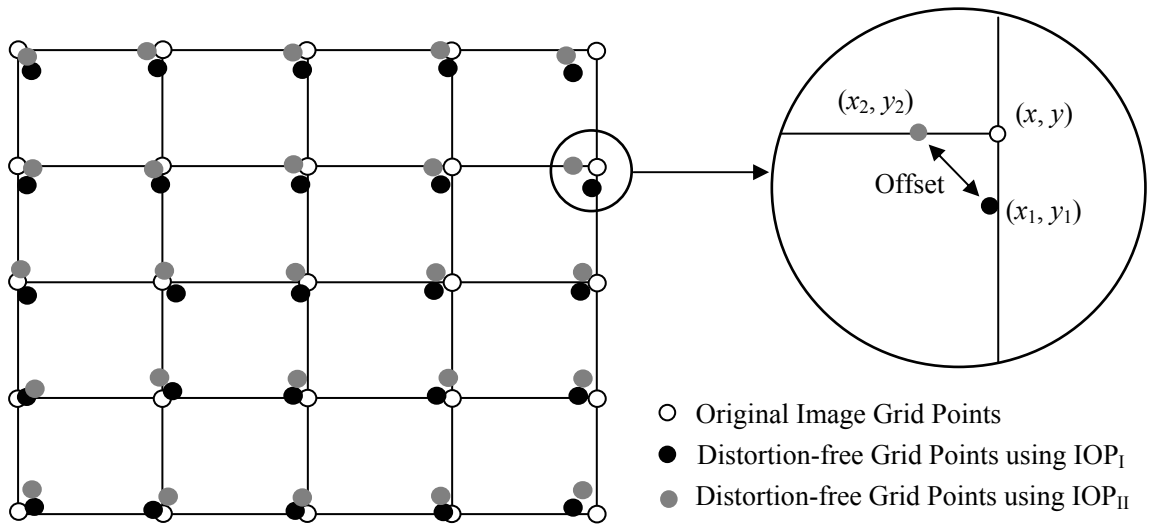
Figure 3.3: The offset between distortion-free coordinates in the Misclosure method

To estimate the offset between the two IOP sets, the x and y coordinate difference between the two distortion-free points of each grid point is computed, Figure 3.3. The degree of similarity is given by the root mean square error (RMSE) of these computed x and y coordinate differences. If the RMSE is within the range defined by the expected standard deviation of the image coordinate measurements, the two sets of IOP are considered similar. Since the principal distances are assumed to be equal, it is expected that this method will give unrealistic or unreliable results. The method described in the next sub-section takes the estimated principle distance into consideration.

3.3.2 Zero Rotation (ZROT) Method

Unlike the MIS method, the analysis for stability using the Zero Rotation (ZROT) method is initiated by defining a bundle of light rays for each of the two sets of IOP that are being tested for similarity. The two bundles will share the same perspective center and have parallel image coordinate systems, Figure 3.4. To create the two bundles, the

procedure starts off by first defining a synthetic regular grid in the two-dimensional image plane. This is followed by removing various distortions at the defined grid vertices using the two IOP sets that are being compared. The result will be the creation of two distortion-free points for each grid point.
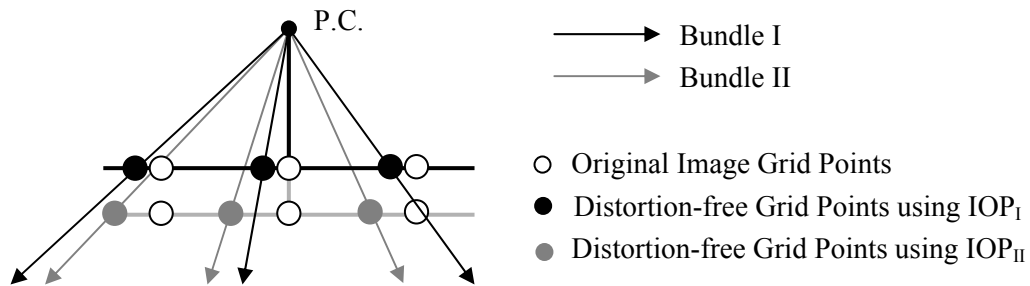
Figure 3.4: Two bundles of light rays with same perspective center and parallel image coordinate systems defined by two sets of IOP

To estimate the offset between the two IOP sets, the x and y coordinate difference between the two distortion-free points of each grid point is computed, Figure 3.5. However, the two distortion-free points may not necessarily be on the same plane since the principal distance of the two IOP sets could be different. Hence, the distortion-free grid points of one IOP set have to be projected onto the image plane of the other IOP set. This is accomplished by the formulas provided in Equations 3.4, where (x_2, y_2) are the distortion-free coordinates of a grid point according to the second IOP set, (x'_2, y'_2) are the same coordinates projected onto the image plane of the first IOP set, and c_1 and c_2 are the principal distances of the first and second IOP set, respectively.

$$x'_2 = x_2 \frac{c_1}{c_2}; \qquad y'_2 = y_2 \frac{c_1}{c_2} \qquad\qquad (3.4)$$

Once all the points are on the same plane, the offset (i.e. the x and y coordinate differences) between the two distortion-free points of each grid point is computed, Figure 3.5. As was the case in the MIS method, the degree of similarity is given by the RMSE of these computed offsets. If the RMSE is within the range defined by the expected standard deviation of the image coordinate measurements, the two sets of IOP are considered similar. It is expected that the ZROT method will yield conservative RMSE values since the position and orientation of the bundles are fixed.
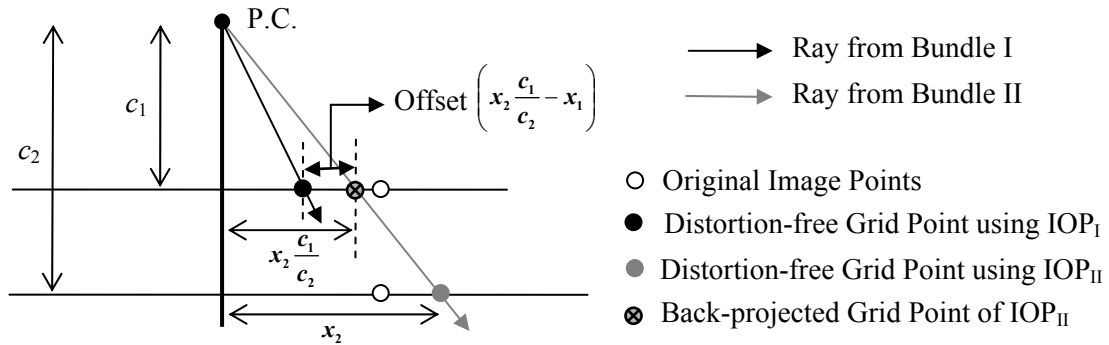
Figure 3.5: The offset between distortion-free coordinates in the Zero Rotation method

As previously mentioned, the image coordinate systems associated with the two bundles are assumed to be parallel to each other. The method described in the next sub-section does not make this assumption, and in fact, determines a set of rotation angles that would make the two bundles coincide with each other as much as possible.

3.3.3 Rotation (ROT) Method

The ZROT method of comparison assumes the coincidence of the optical axes of the reconstructed bundles defined by the two IOP sets. However, stability analysis should be

concerned with determining whether conjugate light rays coincide with each other regardless of the orientation of the respective image coordinate systems. Therefore, one has to check if there is a unique set of rotation angles (ω, φ, κ) that can be applied to the first bundle to produce the second one while maintaining the same perspective center, Figure 3.6.
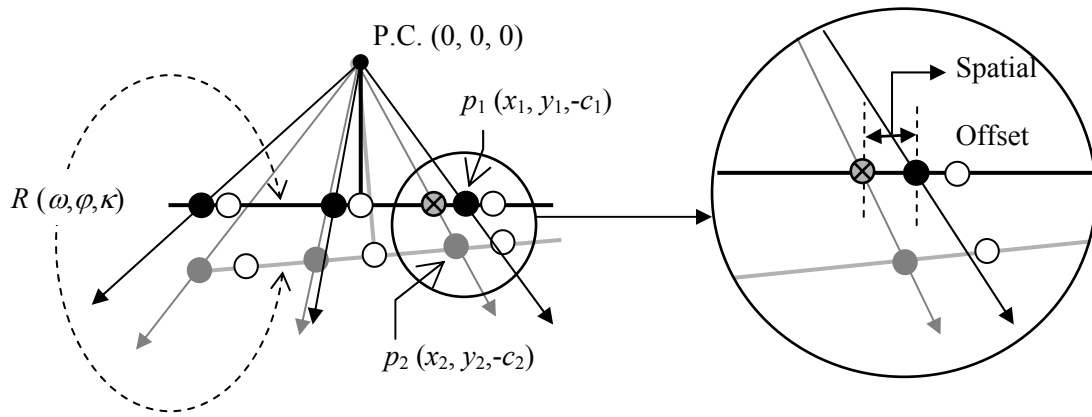
Figure 3.6: The two bundles in the ROT method are rotated to reduce the angular offset

between conjugate light rays

As shown in Figure 3.6, (x_1, y_1, $-c_1$) and (x_2, y_2, $-c_2$) are the three-dimensional vectors connecting the perspective center and the distortion-free coordinates of the same image point according to IOP_I and IOP_{II}, respectively. To make the two vectors coincide with each other, the first vector has to be rotated until it is aligned along the second vector. The coincidence of the two vectors after applying the rotation angles can be mathematically expressed by Equation 3.5.

$$\begin{bmatrix} x_1 \\ y_1 \\ -c_1 \end{bmatrix} = \lambda \; R^T(\omega,\phi,\kappa) \begin{bmatrix} x_2 \\ y_2 \\ -c_2 \end{bmatrix} \tag{3.5}$$

To eliminate the scale factor (λ), the first two rows in Equation 3.5 are divided by the third one producing Equations 3.6.

$$x_1 = -c_1 \frac{r_{11}\, x_2 + r_{21}\, y_2 - r_{31}\, c_2}{r_{13}\, x_2 + r_{23}\, y_2 - r_{33}\, c_2}$$

$$y_1 = -c_1 \frac{r_{12}\, x_2 + r_{22}\, y_2 - r_{32}\, c_2}{r_{13}\, x_2 + r_{23}\, y_2 - r_{33}\, c_2}$$

(3.6)

Equations 3.6 represent the necessary constraints for making the two bundles defined by IOP_I and IOP_{II} coincide with each other as well as possible. Having (n) conjugate points, one can produce (2n) constraints of the form in Equations 3.6. These constraints can be used to solve for the rotation angles (ω, φ, κ) using a least-squares adjustment. The variance component (σ_o^2), which is the variance of an observation of unit weight, resulting from the adjustment procedure represents the quality of the coincidence between the two bundles after applying the estimated rotation angles. The smaller the variance component, the more similar the two bundles are to each other. A closer investigation of the estimated residuals from Equations 3.6 would reveal a more meaningful clue regarding the value of the estimated variance component (σ_o^2).

Assuming that (x_1, y_1) in Equations 3.6 are the observed values, the corresponding residuals represent the spatial offset between the two bundles, after applying the rotation angles, along the image plane defined by the first IOP set, Figure 3.6. Therefore, assigning a unit weight to all the constraints resulting from various image points yields a variance component that represents the variance of the spatial offset between the two bundles along the image plane. A relative comparison between the computed variance

component and the expected variance of image coordinate measurements would reveal whether the two bundles are significantly different from each other or not. If the variance component lies within the range defined by the variance of image coordinate measurements, the two bundles can be considered to be similar. The evaluation of the degree of similarity between the two bundles can be summarized as follows:

i. Define a synthetic regular grid in the image plane.

ii. Remove various distortions at the defined grid vertices using the derived IOP from two calibration sessions.

iii. Define two bundles of light rays using the principal distance, principal point coordinates, and distortion-free coordinates of the grid vertices.

iv. Assuming the bundles share the same perspective centre, derive an estimate of the rotation angles (ω, φ, κ) that are needed to make the two bundles coincide with each other as well as possible according to the constraints in Equations 3.6.

v. Compare the estimated variance component (σ_o^2), resulting from the adjustment procedure in the previous step, to the expected variance of the image coordinate measurements. If the variance component is within the range defined by the variance of the image coordinate measurement, the two IOP sets are deemed to be similar.

The ROT method provides a meaningful measure for evaluating the degree of similarity between two bundles of light rays, defined by two sets of IOP, sharing the same origin (perspective center) regardless of their orientation in space. However, it is possible that

the IOP and the positional component of the EOP (X_O, Y_O, Z_O in Equations 2.5) are correlated. Therefore another methodology has been developed to compare the two bundles while allowing for the de-correlation between the IOP and EOP.

3.3.4   Single Photo Resection (SPR) Method

In contrast to the ROT method, the SPR method evaluates the quality of fit between the two bundles at a given object space while allowing for spatial and rotational offsets between the respective image coordinate systems. In other words, the two bundles are permitted to have different perspective centers. The methodology for evaluating the degree of similarity between the two bundles in terms of their fit at a given object space can proceed as follows:

i. Define a regular grid in the image plane.

ii. Use the available IOP sets to derive two sets of distortion-free coordinates of the grid vertices.

iii. Define a bundle of light rays for the first IOP set using the perspective center together with the corresponding distortion-free grid vertices.

iv. Intersect the defined bundle with an arbitrary object space to produce a set of object points, as shown in Figure 3.7.

v. Use the derived object points and the corresponding distortion-free grid vertices, according to the second set of IOP, in a Single Photo Resection (SPR) procedure to

estimate the position and the attitude of the second bundle that fits the object space as defined by the given set of object points.

vi. The variance component resulting from the SPR procedure represents the variance of the spatial offset between the distortion-free grid vertices that are defined by the second set of IOP, and the computed image coordinates from back projecting the object points onto the respective image plane, Figure 3.7.
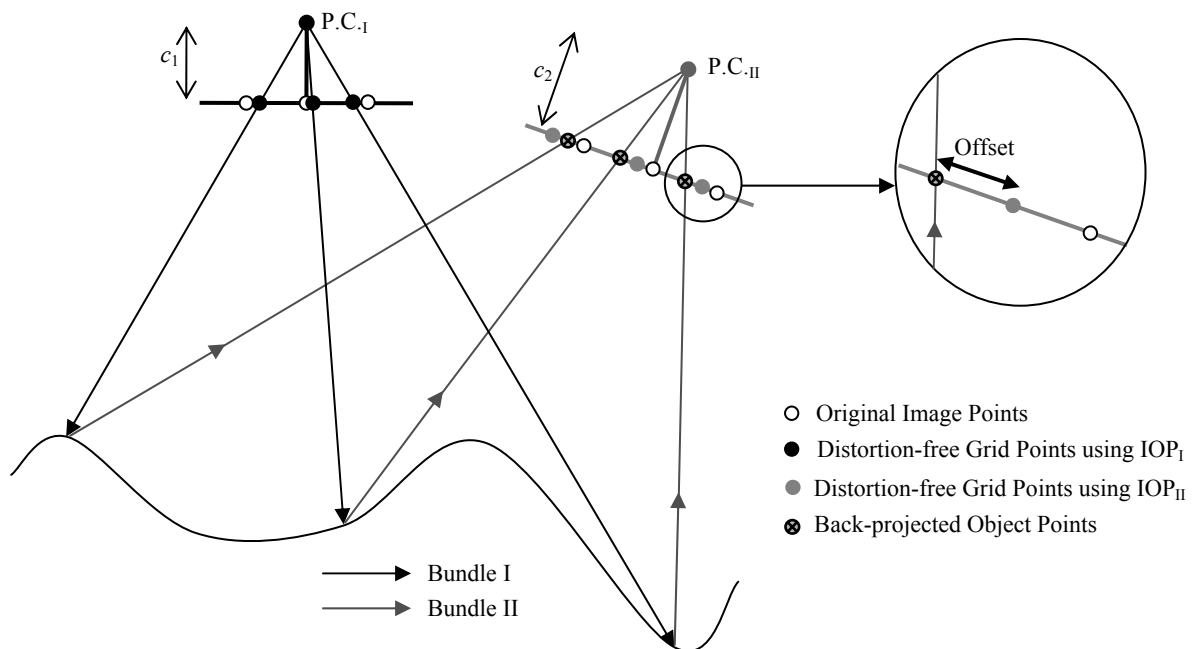
Figure 3.7: SPR method allows for spatial and rotational offsets between the two bundles to achieve the best fit at a given object space

Similar to the MIS, ZROT, and ROT methodologies, if the estimated variance component lies within the range defined by the expected variance of image coordinate measurements, the two bundles are deemed to have a good fit at the given object space. It is expected that the SPR method with a relatively flat terrain will lead to a good fit

between the two bundles at the object space, even if the two IOP sets are significantly different from each other. This will be the case since the estimated EOP will adapt (shift and rotate) in a way to absorb the differences between the involved IOP. On the other hand, a rugged terrain would allow for the de-correlation between the IOP and EOP, and give a more strict measure for the degree of similarity between the two bundles.

CHAPTER 4

EXPERIMENTS AND RESULTS

4.1 Introduction

The experiments conducted in this research were geared towards calibrating and analyzing the stability of various digital cameras ranging in quality, features, and price. This was done over a period of thirteen months. Based on the results, a number of inferences are made about the tested cameras. In the following sections, an illustration of the calibration test field, a few technical details on each camera used in the experiments, and a brief description of the calibration and stability analysis software are presented. This is then followed by the results of the stability analysis tests of the implemented cameras and the analysis of the dependence of IOP comparisons on the manipulation of certain conditions in the calibration procedure. In addition, the similarity measures are compared to one another in terms of their effect on the defined bundles in space and the computed RMSE and standard deviation values.

4.2 Experiment Description

To perform calibration and stability analysis on the cameras, a specific detailed procedure was carried out. A test field consisting of straight lines and points was used for calibration, as discussed in Chapter 2, Section 2.4. The number of images taken by each camera as well as the approximate position and orientation of each image was pre-determined and there were a total of ten digital cameras tested in the experiments.

4.2.1 Test Field Configuration

For calibration purposes, a two-dimensional test field with straight line features and points was used. The test field was created in TerraPoint Canada, formerly known as the Mosaic Mapping Corporation, in Calgary, Figure 4.1. Lines and points were established on a 4.0 x 7.5 meter section of a white wall.

Figure 4.1: Creation of the calibration test field

The lines are thin and dark ropes that are stretched between nails on the wall. The straightness of the ropes is assured by using light material and applying adequate tension. The points are signalized targets that are in the form of crosses and are used as tie points in the calibration procedure. Distances between the points have also been measured with an accuracy of ±2.0mm to be used as check distances and to help establish the datum. As described in Chapter 2, Section 2.4.1, the optimum configuration of the calibration test field is used. There are eight horizontal lines, twelve vertical lines and twenty-one points well-dispersed throughout the test field as shown in Figure 4.2.
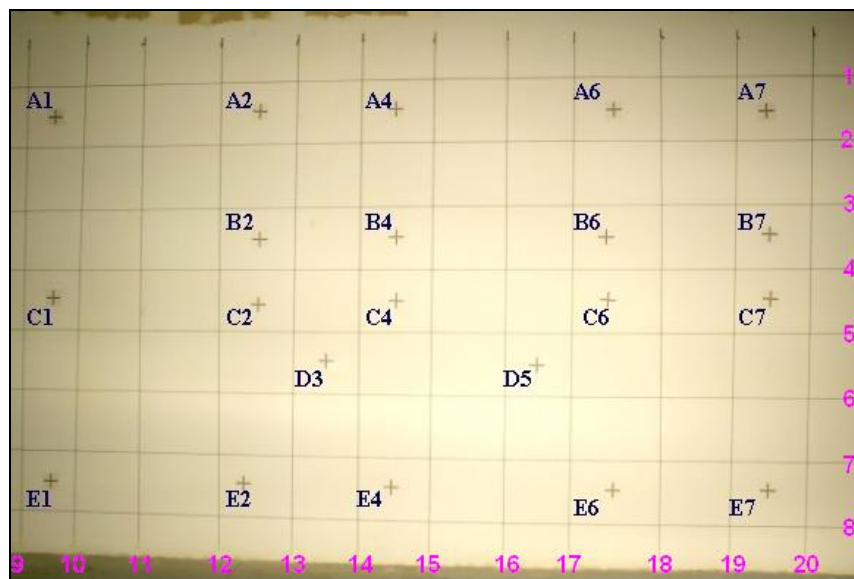
Figure 4.2: Calibration test field with 20 lines and 21 points

The datum for the calibration procedure is established by fixing a certain number of points as control points that are distributed in a specific way. To establish a datum, the origin, orientation, and scale need to be fixed. The fixed coordinates of three points are shown in Figure 4.3. By fixing the X, Y and Z coordinates of point E1, the origin is established. By fixing the Y and Z coordinates of points E1 and E7 as well as the Y

coordinate of point A4, the orientation is established. Finally, the scale is established by incorporating a distance measurement between any two points.
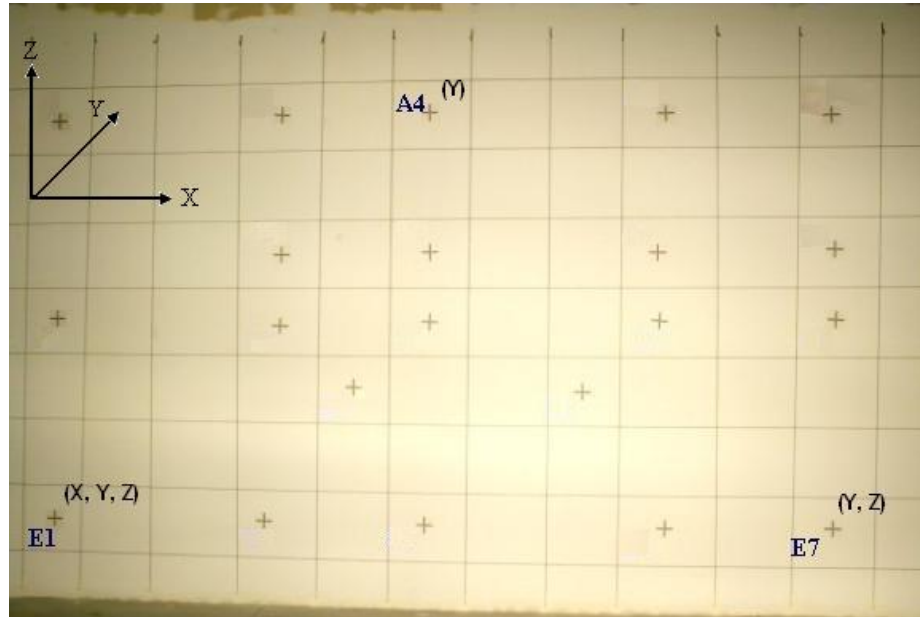
Figure 4.3: Coordinates of the points that are fixed to help establish the datum for

    calibration

If a three-dimensional test field is used for calibration, images would not have to be convergent and taken at different angles. However, for a two-dimensional test field, convergent images (images with 80% to 100% overlap) are important since they strengthen the geometry of the system. They also reduce the correlation between the depth and the focal length by changing the scale within the captured images. In addition, images are taken with the camera rotated 90° to avoid correlation between the IOP of the camera and the EOP of the imagery. This rotated portrait-oriented image does not cover the entire or at least a significant amount of the test field and that is the reason why two rotated shots are taken at each position, Figure 4.4. Furthermore, horizontal lines on the

test field should not be parallel to the baseline, which is the line joining the exposure stations (i.e. camera positions), as discussed in Chapter 2, Section 2.4.1. To avoid this parallelism, images are captured at two different heights.

For the conducted camera calibration experiments, eighteen converging and overlapping images are captured at locations that are roughly four to five meters away from the closest point on the test field. The position and orientation of each captured image are shown in Figure 4.4. Images are taken from six positions: two in the center, two from the left and two from the right side of the test field. At the center and each side location, images are captured at two different heights. Nine images are captured on the floor level and another nine are captured at a height of about ten feet above the floor. One landscape-style image and two portrait-style images are captured at each position.
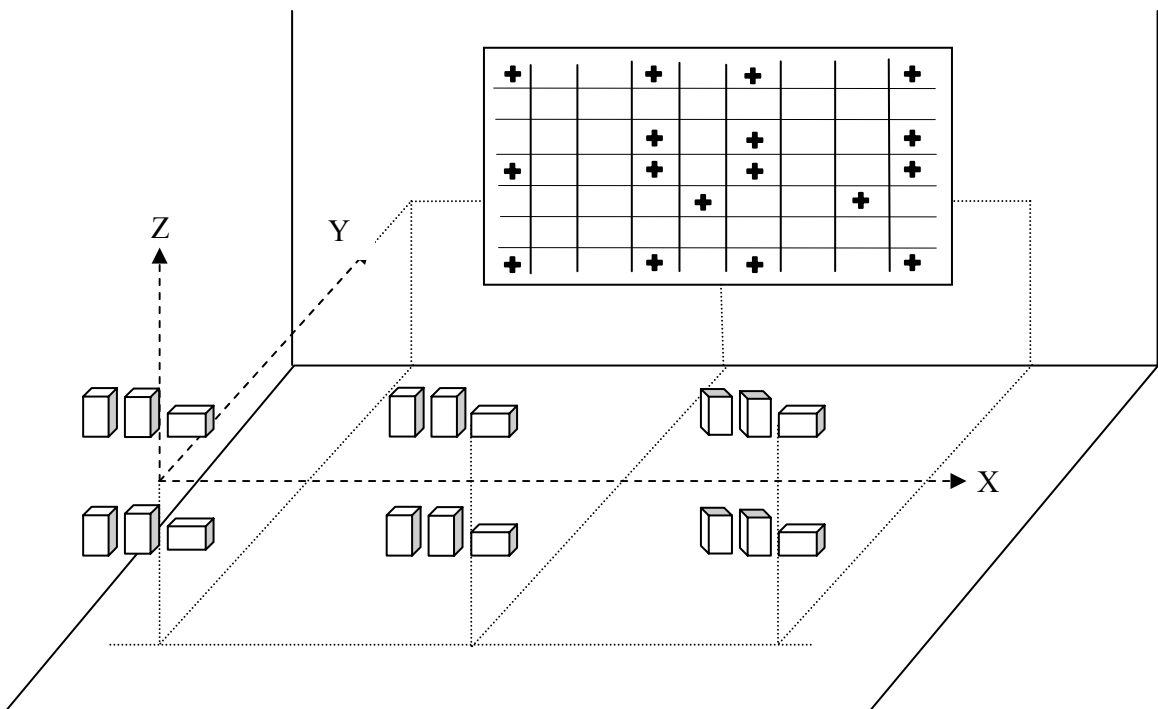
Figure 4.4: Position and orientation of 18 images captured for a calibration dataset

4.2.2 Tested Cameras

The cameras implemented for calibration and stability analysis are digital cameras ranging in price from $650 to $8000 CDN. They are all Single-lens Reflex (SLR) cameras with Charged-coupled Device (CCD) sensors. SLR cameras have just one lens that is used for both composing the frame (viewing) and capturing the image to memory. A CCD sensor is a semiconductor light detector which converts light to electrical impulses, and is commonly found in many electronic devices including digital cameras. The five different types of cameras tested in this research include:

- Canon EOS 1D – It is a professional SLR digital camera whose body is made of a magnesium alloy with magnetic shielding of its electronic components, Figure 4.5. This makes it extremely strong, durable, and weather-resistant. It has a 28.7 x 19.1 mm CCD sensor with a 2.0" color monitor. It has a continuous shooting speed of eight frames per second and can sustain this for 21 frame bursts.

Figure 4.5: Canon's EOS 1D professional SLR digital camera

- Nikon Coolpix 4500 – It is an amateur digital camera with a 1/1.8" high density CCD combined with a 4x optical (38-155 mm in 35 mm photography) Zoom-Nikkor lens, Figure 4.6. It has a swivel-lens design and a 1.5" TFT LCD monitor.

Figure 4.6: Nikon Coolpix 4500 amateur digital camera

- Rollei d7 – It is a professional metric camera specially made for photogrammetric use, Figure 4.7. It is made in Germany and can only be acquired from the company on special order. It has a 2/3" CCD Chip with a 2.5" color display, and uses a Rollei D-Apogon 7.3mm f 2.8 HFT lens (equivalent 28mm for 35mm film cameras).

Figure 4.7: Rollei d7 professional metric camera

- Sony DSC-F707 is a high-end amateur camera, Figure 4.8. It features a 5x optical Carl Zeiss lens with a focal length range of 9.7 - 48.5 mm (38 - 190 mm

equivalent). It has a 2/3" CCD sensor and a 1.8" LCD display. It has many unique image capturing features like NightFraming, Hologram AF and true TTL flash metering.

Figure 4.8: Sony DSC-F707 high-end amateur camera

- Sony DSC-P9 is a lightweight amateur camera, Figure 4.9. It has a 3x optical zoom lens with a focal range of 8 - 24 mm (39 - 117 mm equivalent). It has a 1/1.8" CCD and a 1.5" LCD display.

Figure 4.9: Sony DSC-P9 amateur camera

Table 4.1 summarizes the characteristics of the cameras mentioned above. The maximum output resolution, which corresponds to the image size, is required for the calibration and stability analysis procedures since all images are captured at the maximum resolution of the camera.

Table 4.1: Characteristics of implemented cameras

Camera	Price Range ($ Cdn.)	Maximum Output Resolution	Pixel Size	Effective Pixels
Canon EOS 1D	$7000	2464x1648 pixels	11.5 μm	4.15 megapixels
Nikon 4500	$650 - $800	2272x1704 pixels	3.1 μm	3.87 megapixels
Rollei d 7 metric	$8000 (special order)	2552x1920 pixels	4.0 μm	4.90 megapixels
Sony DSC-F707	$900 - $1100	2560x1920 pixels	4.0 μm	4.92 megapixels
Sony DSC-P9	$650	2272x1704 pixels	4.0 μm	3.90 megapixels

There were a total of ten individual cameras tested in the experiments. The following list contains the designated names used in this report for these cameras:

- Two Canon EOS 1D cameras denoted as CanonOne and CanonTwo

- Five Nikon 4500 cameras denoted as Nikon288616, Nikon288894, Nikon288895, Nikon288896, and Nikon288990

- One Rollei d7 metric camera denoted as Rollei

- One Sony DSC-F707 camera denoted as SonyF707

- One Sony DSC-P9 camera denoted as SonyP9

4.2.3   Software Description

There are three pieces of software that are involved in the entire process of calibration and stability analysis: AutoMeasure, MSAT, and CAST. These programs were developed by the Photogrammetry research group at the University of Calgary. Each program accomplishes a certain task in either the calibration or stability analysis procedures. With regard to the use of the software, there are three basic steps to follow: measurements, calibration and similarity comparisons.

The AutoMeasure program is utilized for defining and measuring points and automatically detecting and measuring lines. Once the measurements have been done, the calibration of the camera is carried out using the Multi-Sensor Aerial Triangulation (MSAT) program. Using the IOP results from the calibration, the CAST program is used to perform the bundle comparisons to evaluate the similarity between the IOP sets.

4.3 Stability of Implemented Cameras

As previously mentioned, a total of ten digital cameras were calibrated and evaluated for stability over a thirteen-month period. For each camera, with the exception of three Nikon 4500 cameras, image datasets were acquired in two or more of the following months: July 2003, October 2003, January 2004, February 2004, August 2004, and October 2004. Since datasets from at least two different calibration sessions are available, the stability of the IOP of the cameras can be evaluated.

Three of the four proposed similarity measures, ZROT, ROT, and SPR, are implemented in these experiments. The MIS method is not used because it assumes the same principal distance for the two sets of IOP being compared and hence, will give an unrealistic or unreliable measure for the degree of similarity. In these similarity measures, the percentage of the image occupied by the test field is used as an indication of the expected quality of the estimated IOP (refer to Chapter 3, Section 3.3.1). For example, a test field occupying 95% of the image will produce more reliable IOP estimates than that occupying 70% of the image. Theoretically, the test field should occupy 100% of the image and the extent of the grid (in the stability analysis methods) should not have a bearing on the validity of the computed similarity measures. However, it is difficult to have the test field occupying the entire image. Hence, for the conducted experiments, the percentage specified for the grid extent was 90%, which is a balance between the optimum coverage and the true values of the coverage. Tables 4.2 to 4.7 below reveal the actual coverage percentages for all image datasets captured in the four calibration sessions during the thirteen-month period.

Table 4.2: Percentage of image occupied by the test field for the July 2003 calibration session

Camera	Camera/Calibration Settings	Number of Images	Percentage occupied by Test Field
CanonOne	Lens and Filter On	18	77.82%
	Filter Off	18	75.05%
	Lens Off/On & Filter Off	18	73.18%
CanonTwo	Lens and Filter On	16	74.25%
	Filter Off	18	71.17%

	Lens Off/On & Filter Off	18	72.03%
Rollei	Small Test Field	14	91.54%
	Big Test Field	14	67.81%
SonyF707	Small Test Field	19	95.05%
	Big Test Field	18	82.15%
SonyP9	One Set	17	74.05%

Table 4.3: Percentage of image occupied by the calibration test field for the October 2003 calibration session

Camera	Camera/Calibration Settings	Number of Images	Percentage occupied by Test Field
CanonOne	Lens and Filter On	18	69.81%
	Filter Off	18	70.02%
	Lens Off/On & Filter Off	18	68.34%
	Filter On	18	67.16%
CanonTwo	Lens and Filter On	18	69.58%
	Filter Off	18	67.88%
	Lens Off/On & Filter Off	18	66.57%
	Filter On	18	67.81%
Rollei	One Set	14	55.28%
SonyF707	Manual Focus	16	68.42%
	Auto Focus	17	79.00%

Table 4.4: Percentage of image occupied by the calibration test field for the January 2004 calibration session

Camera	Camera/Calibration Settings	Number of Images	Percentage occupied by Test Field
CanonOne	Lens and Filter On	17	75.36%
	Filter Off	16	76.75%
	Lens Off/On & Filter Off	18	74.42%
	Filter On	18	73.22%
CanonTwo	Lens and Filter On	17	75.29%
	Filter Off	18	74.84%
	Lens Off/On & Filter Off	18	72.63%
	Filter On	18	73.56%
Nikon288616	Set 1	18	75.59%
	Set 2	18	78.09%
Nikon288895	Set 1	18	78.94%
	Set 2	18	81.82%
Rollei	One Set	14	66.35%
SonyP9	Set 1	18	79.49%
	Set 2	18	79.22%

Table 4.5: Percentage of image occupied by the calibration test field for the February 2004 calibration session

Camera	Camera/Calibration Settings	Number of Images	Percentage occupied by Test Field
Nikon288616	Set 1	18	76.06%
	Set 2	18	76.43%
Nikon288895	Set 1	18	76.67%
	Set 2	18	76.27%
Rollei	Set 1	14	63.89%
	Set 2	14	63.99%
SonyF707	Set 1	18	77.75%
	Set 2	18	79.09%

Table 4.6: Percentage of image occupied by the calibration test field for the August 2004 calibration session

Camera	Camera/Calibration Settings	Number of Images	Percentage occupied by Test Field
CanonOne	Set 1	18	77.82%
	Set 2	18	78.56%
CanonTwo	Set 1	18	75.88%
	Set 2	18	78.26%
Nikon288990	Set 1	18	81.68%
	Set 2	18	83.20%
	Set 3	18	83.01%
Nikon288616	Set 1	18	81.92%
	Set 2	18	80.08%

Nikon288894	Set 1	18	78.60%
	Set 2	18	80.96%
Rollei	Set 1	14	71.97%
	Set 2	14	74.57%
SonyF707	Set 1	18	83.14%
	Set 2	18	83.30%
	Set 3	18	86.43%
SonyP9	Set 1	18	79.78%
	Set 2	18	83.07%

Table 4.7: Percentage of image occupied by the calibration test field for the October 2004 calibration session

Camera	Camera/Calibration Settings	Number of Images	Percentage occupied by Test Field
Nikon288616	Set 1	18	78.44%
	Set 2	18	77.44%
SonyF707	Set 1	18	79.73%
	Set 2	18	80.84%

To check the stability of the cameras over a significant period of time, the degree of similarity between reconstructed bundles of two sets of IOP is evaluated. As mentioned in Chapter 3, Section 3.3.2, in the ZROT method, the measure of the spatial offset between two bundles obtained from two sets of IOP is represented by the RMSE of the coordinate differences between the distortion-free points of the two IOP sets. In addition, in Section 3.3.3, the estimated square root of the variance component (σ_o) resulting from

the adjustment procedure, either from the ROT or the SPR techniques, represents the standard deviation of the spatial offset between the two bundles along the image plane. If these values (RMSE or σ_o) are not significantly larger than the expected image coordinate measurement accuracy, which can be considered to be approximately one-half to two-thirds of a pixel, then the two sets of IOP are deemed similar. For example, in the case of the Canon camera, the pixel size is 11.5 μm. Hence, the RMSE obtained from ZROT and the standard deviation of the spatial offset (σ_o) from ROT and SPR must be less than 7.70 μm, which corresponds to two-thirds of a pixel, for the IOP sets to be considered similar. Table 4.8 shows the range of acceptable image coordinate measurement accuracies for each of the implemented cameras in terms of their assumed pixel sizes.

Table 4.8: Acceptable image coordinate measurement accuracies in terms of the pixel sizes of the implemented cameras

(<u>Note</u>: If RMSE or σ_o < Two-Third Pixel Size, IOP sets considered similar)

Camera	Pixel Size (μm per pixel)	Half Pixel Size (μm per ½ pixel)	Two-Third Pixel Size (μm per ⅔ pixel)
Canon EOS 1D	11.50 x 11.50	5.75	7.70
Nikon 4500	3.10 x 3.10	1.55	2.10
Rollei d7 metric	4.00 x 4.00	2.00	3.00
Sony DSC-F707	4.00 x 4.00	2.00	3.00
Sony DSC-P9	4.00 x 4.00	2.00	3.00

The stability results for the ten digital cameras (denoted by their experiment names) are listed in Tables 4.9 to 4.15. As mentioned earlier, the similarity measures implemented

are the ZROT, ROT, and SPR (where the flying height = 1000 m and the terrain height variation = 100 m).

i. CanonOne – From Table 4.9, it can be seen that CanonOne is stable according to the ROT and SPR methods. However, the camera fails the test of stability under the ZROT method. It is expected that the ZROT method will give such conservative results since the bundles are not allowed to shift and rotate in space relative to each other in order to get a better fit.

Table 4.9: Stability comparison of IOP sets for CanonOne

(<u>Note</u>: If RMSE or $\sigma_o < 7.70$ μm, IOP sets considered similar)

ID	Date		ZROT		ROT		SPR	
	IOP Set I	IOP Set II	RMSE (μm)	Similar	σ_o (μm)	Similar	σ_o (μm)	Similar
1	Jul 03	Oct 03	22.13	No	2.56	Yes	1.96	Yes
2	Jul 03	Jan 04	9.66	No	1.42	Yes	0.55	Yes
3	Oct 03	Jan 04	35.22	No	4.69	Yes	2.52	Yes
4	Jul 03	Aug 04	31.30	No	2.36	Yes	1.71	Yes
5	Oct 03	Aug 04	37.77	No	2.02	Yes	1.76	Yes

ii. CanonTwo – Similar to CanonOne, the RMSE and σ_o components must be less than 7.70 μm for the IOP sets to be considered similar. From observing Table 4.10, all IOP set comparisons reveal that the IOP of this camera is stable over short and long periods of time based on the results derived from the ROT and SPR methods. Once again, the ZROT yielded results that are too conservative.

Table 4.10: Stability comparison of IOP sets for CanonTwo

(<u>Note</u>: If RMSE or σ_o < 7.70 μm, IOP sets considered similar)

ID	Date		ZROT		ROT		SPR	
	IOP Set I	IOP Set II	RMSE (μm)	Similar	σ_o (μm)	Similar	σ_o (μm)	Similar
1	Jul 03	Oct 03	39.34	No	2.93	Yes	2.66	Yes
2	Jul 03	Jan 04	73.71	No	4.80	Yes	3.79	Yes
3	Oct 03	Jan 04	32.27	No	6.14	Yes	2.81	Yes
4	Jul 03	Aug 04	46.06	No	4.66	Yes	2.89	Yes
5	Oct 03	Aug 04	10.09	No	3.56	Yes	0.62	Yes

iii. Rollei − The results in Table 4.11 demonstrate that the IOP sets of the Rollei are similar for all ten comparisons done from July of 2003 to August of 2004 based on the ROT and SPR results. However, the IOP sets were considered different according to the ZROT results similar to the case of the Canon cameras.

Table 4.11: Stability comparison of IOP sets for Rollei

(<u>Note</u>: If RMSE or σ_o < 3.00 μm, IOP sets considered similar)

ID	Date		ZROT		ROT		SPR	
	IOP Set I	IOP Set II	RMSE (μm)	Similar	σ_o (μm)	Similar	σ_o (μm)	Similar
1	Jul 03	Oct 03	26.81	No	2.90	Yes	1.56	Yes
2	Jul 03	Jan 04	15.69	No	1.47	Yes	0.92	Yes
3	Oct 03	Jan 04	14.30	No	1.46	Yes	0.92	Yes
4	Jul 03	Feb 04	27.43	No	2.01	Yes	1.51	Yes
5	Oct 03	Feb 04	15.69	No	1.80	Yes	0.95	Yes
6	Jan 04	Feb 04	12.15	No	1.03	Yes	0.75	Yes
7	Jul 03	Aug 04	18.11	No	1.97	Yes	1.19	Yes
8	Oct 03	Aug 04	11.08	No	1.16	Yes	0.92	Yes
9	Jan 04	Aug 04	3.29	No	0.60	Yes	0.39	Yes
10	Feb 04	Aug 04	11.21	No	1.35	Yes	0.92	Yes

iv. SonyF707 – The SonyF707 was the only camera that was tested over the longest period of time (fifteen months) from July of 2003 to October of 2004. Based on the results in Table 4.12, all comparisons of IOP sets indicate that the IOP of this camera did not change since σ_o (obtained from ROT and SPR) was within the acceptable image coordinate measurement accuracy of 3.00 μm. As expected, the ZROT results suggest that the camera did not maintain the stability of its IOP.

Table 4.12: Stability comparison of IOP sets for SonyF707

(<u>Note</u>: If RMSE or σ_o < 3.00 μm, IOP sets considered similar)

ID	Date		ZROT		ROT		SPR	
	IOP Set I	IOP Set II	RMSE (μm)	Similar	σ_o (μm)	Similar	σ_o (μm)	Similar
1	Jul 03	Oct 03	18.00	No	2.06	Yes	1.06	Yes
2	Jul 03	Feb 04	18.77	No	1.76	Yes	1.09	Yes
3	Oct 03	Feb 04	3.49	No	2.91	Yes	0.31	Yes
4	Jul 03	Aug 04	15.97	No	1.61	Yes	1.07	Yes
5	Oct 03	Aug 04	8.00	No	2.75	Yes	0.37	Yes
6	Feb 04	Aug 04	9.03	No	0.34	Yes	0.27	Yes
7	Jul 03	Oct 04	23.92	No	1.67	Yes	1.06	Yes
8	Oct 03	Oct 04	6.80	No	2.80	Yes	0.39	Yes
9	Feb 04	Oct 04	5.43	No	0.31	Yes	0.28	Yes
10	Aug 04	Oct 04	13.68	No	0.52	Yes	0.49	Yes

v. SonyP9 – Only three calibrations of the SonyP9 were done. However, the sessions were well spread out, going from July of 2003 to August of 2004, as shown in Table 4.13. The ROT and SPR results in this table show that the IOP comparisons of this

camera yielded a σ_o component well below the required image coordinate measurement accuracy of 3.00 μm. Hence, this camera is also considered stable.

Table 4.13: Stability comparison of IOP sets for SonyP9

(<u>Note</u>: If RMSE or σ_o < 3.00 μm, IOP sets considered similar)

ID	Date		ZROT		ROT		SPR	
	IOP Set I	IOP Set II	RMSE (μm)	Similar	σ_o (μm)	Similar	σ_o (μm)	Similar
1	Jul 03	Jan 04	14.19	No	1.45	Yes	0.49	Yes
2	Jul 03	Aug 04	3.61	No	1.46	Yes	0.19	Yes
3	Jan 04	Aug 04	11.18	No	0.44	Yes	0.38	Yes

vi. Five Nikon Cameras – For the Nikon cameras, only two (Nikon288616 and Nikon288894) were tested for long-term stability, Table 4.14. Based on these results, all Nikon cameras did not show good long-term stability according to the ZROT and ROT methods. However, it did show good stability according to the SPR method, but this is deceiving since SPR provides a very relaxed degree of similarity because of the assumption of a relatively low terrain height variation with respect to the flying height. Hence, further experiments were conducted to see whether this camera had good short-term stability (i.e. comparing sets that were acquired on the same day by switching the camera off and on between dataset acquisitions), Table 4.15. The majority of the short-term stability results indicate that the Nikons do not maintain the same IOP values according to the ZROT and ROT methods, even in a short time period, and therefore, is considered unstable.

Table 4.14: Long-term stability comparison of IOP sets for Nikon cameras

(<u>Note</u>: If RMSE or σ_o < 2.10 μm, IOP sets considered similar)

ID	Camera	Date		ZROT		ROT		SPR	
		IOP Set I	IOP Set II	RMSE (μm)	Similar	σ_o (μm)	Similar	σ_o (μm)	Similar
1	288616	Jan 04	Aug 04	6.74	No	5.66	No	0.62	Yes
2	288616	Jan 04	Oct 04	2.99	No	2.85	No	0.31	Yes
3	288616	Aug 04	Oct 04	4.80	No	2.80	No	0.32	Yes
4	288894	Feb 04	Aug 04	5.48	No	2.96	No	0.38	Yes

Table 4.15: Short-term stability comparison of IOP sets for Nikon cameras

(<u>Note</u>: If RMSE or σ_o < 2.10 μm, IOP sets considered similar)

ID	Camera	Date / Set No.		ZROT		ROT		SPR	
		IOP Set I	IOP Set II	RMSE (μm)	Similar	σ_o (μm)	Similar	σ_o (μm)	Similar
1	288616	Jan 04 / Set 1	Jan 04 / Set 2	8.04	No	6.18	No	0.67	Yes
2	288616	Aug 04 / Set 1	Aug 04 / Set 2	118.15	No	55.33	No	6.99	No
3	288616	Oct 04 / Set 1	Oct 04 / Set 2	2.54	No	0.61	Yes	0.09	Yes
4	288894	Feb 04 / Set 1	Feb 04 / Set 2	6.66	No	4.75	No	0.54	Yes
5	288894	Aug 04 / Set 1	Aug 04 / Set 2	4.29	No	3.45	No	0.38	Yes
6	288895	Jan 04 / Set 1	Jan 04 / Set 2	7.32	No	3.11	No	0.39	Yes
7	288896	Feb 04 / Set 1	Feb 04 / Set 2	21.18	No	16.03	No	1.95	Yes
8	288990	Aug 04 / Set 1	Aug 04 / Set 2	4.34	No	0.86	Yes	0.19	Yes
9	288990	Aug 04 / Set 1	Aug 04 / Set 3	6.63	No	3.15	No	0.40	Yes
10	288990	Aug 04 / Set 2	Aug 04 / Set 3	4.35	No	3.98	No	0.42	Yes

4.3.1 Stability Analysis using Statistical Testing

As mentioned in Section 3.2, it is expected that statistical testing will give pessimistic results for stability analysis since it only determines whether two sets of IOP are numerically similar. To verify this, a statistical test was performed for CanonOne based on the procedure outlined in Section 3.2. The test starts by introducing the null hypothesis (H_o: $IOP_I = IOP_{II}$). It is assumed that the IOP values follow a χ^2-distribution where there are 4 degrees of freedom since there are four IOP values (x_p, y_p, c, K_1) in each set. Using the two IOP sets as well as their associated variance-covariance matrices, the test statistic (T) is computed according to Equation 3.3. Assuming a level of significance of 0.005 (0.5%), the test statistic critical value (T_c) for accepting the null hypothesis is 18.55 (i.e., If T < 18.55, the null hypothesis is accepted and IOP sets are considered similar).

The IOP sets that were tested are the same ones that were compared in Table 4.9. The results in Table 4.9 showed that all IOP comparisons proved the stability of CanonOne according to the ROT and SPR methods. However, based on the test statistics computed in Table 4.16, all IOP comparisons except one indicate that the camera is not stable. In the one comparison where the IOP sets were similar (ID 2), the values of the two IOP sets are numerically similar. Hence, these tests prove that statistical testing does in fact provide conservative results even though two set of IOP may be similar from a photogrammetric point of view.

Table 4.16: Stability comparison of IOP sets for CanonOne using Statistical Testing

(<u>Note</u>: If $T < T_c$, null hypothesis accepted and IOP sets considered similar)

ID	Date		Test Statistic (T)	Similar
	IOP Set I	**IOP Set II**		
1	Jul 03	Oct 03	106.05	No
2	Jul 03	Jan 04	18.10	Yes
3	Oct 03	Jan 04	243.45	No
4	Jul 03	Aug 04	220.81	No
5	Oct 03	Aug 04	272.99	No

4.4 Manipulation of Calibration/Camera Conditions

The IOP of a camera can be estimated in a number of different ways based on the camera settings, test field size and number of parameters estimated in the calibration procedure. Hence, estimated IOP sets within the same month (i.e. same calibration session) are compared against different calibration conditions. These conditions involve changing certain settings on the camera, changing the size of the test field, and altering the number of estimated parameters in the calibration procedure. The settings that are changed on the camera are the focusing method (auto/manual), and the manipulation of an SLR lens (e.g., taking it off and putting it back on) and a lens filter. Furthermore, the size of the test field is reduced to include fourteen points and fifteen lines as opposed to the original test field size of twenty-one points and twenty lines. Finally, a constraint on the number of distortion parameters estimated is changed.

The following sub-sections demonstrate whether there is any dependence of the estimated IOP on these factors. If the IOP sets are similar, it proves that there is no dependence. For these experiments, only one similarity measure is implemented, which is the ROT method, since it provides a very realistic measure of similarity based on the stability analysis results discussed in Section 4.3. This is due to the fact that the ROT method allows the bundles to rotate till the best coincidence is achieved, which does not make it as stringent as the ZROT method. Yet, it still forces both bundles to maintain the same position, which does not make it as relaxed as the SPR method and makes it more pragmatic from a photogrammetric point of view.

4.4.1   Alteration of Camera Settings

The settings for the Canon cameras and the SonyF707 are the only cameras whose settings were changed during image acquisition. The Canon cameras have mountable SLR lenses and UV filters that protect the front element of the lens and help improve the quality of the captured image. For each Canon camera, four sets of images were captured in the following way:

- Lens and Filter On (Set1) – This is the original configuration with both the lens and filter mounted on the camera.

- Filter Off (Set2) – Filter is then taken off.

- Lens Off/On and Filter Off (Set3) – With the filter still off, the lens is taken off and then mounted back on.

- Filter On (Set 4) – Filter is finally put back on, which essentially matches the original configuration of Set1.

The experimental results with these incorporated changes are provided in Tables 4.17 to 4.20.

i. CanonOne – Based on the results in Table 4.17, it can be seen that each camera configuration is compared with another, and since the standard deviation of the spatial offset (σ_o) lies within the acceptable range of the expected image coordinate measurement accuracy (6.00 to 7.70 μm), the IOP sets are considered similar. In addition to these tests, some tests of long-term stability of the cameras are carried out where IOP sets from different months with the same camera configuration are compared. From Table 4.18, it can be seen that the IOP sets of IDs 4 (Jul 03 and Jan 04) and 7 (Oct 03 and Jan 04) are not similar. In January, when the first set of images was taken with the lens and filter on, the components or configuration of the camera may not have been set properly. This could be the reason behind the dissimilarity of the IOP sets when the January dataset is compared to the July and October datasets. However, based on the other results, it is safe to conclude that mounting and removing the lens and filter does not play a role in changing the IOP estimates.

Table 4.17: Comparison of IOP sets obtained within the same month for CanonOne with

different camera settings

(<u>Note</u>: If $\sigma_o < 7.70$ μm, IOP sets considered similar)

ID	IOP Set I		IOP Set II		ROT	Similar
	Date	**Camera Settings**	**Date**	**Camera Settings**	σ_o (μm)	
1	Oct 03	Lens and Filter On	Oct 03	Filter Off	5.35	Yes
2	Oct 03	Filter Off	Oct 03	Lens Off/On & Filter Off	4.34	Yes
3	Oct 03	Lens Off/On & Filter Off	Oct 03	Filter On	3.17	Yes
4	Jan 04	Lens and Filter On	Jan 04	Filter Off	1.96	Yes
5	Jan 04	Filter Off	Jan 04	Lens Off/On & Filter Off	1.67	Yes
6	Jan 04	Lens Off/On & Filter Off	Jan 04	Filter On	1.94	Yes

Table 4.18: Stability comparison of IOP sets obtained from different months for CanonOne with same camera settings

(Note: If σ_o < 7.70 μm, IOP sets considered similar)

ID	IOP Set I		IOP Set II		ROT σ_o (μm)	Similar
	Date	Camera Settings	Date	Camera Settings		
1	Jul 03	Lens and Filter On	Oct 03	Lens and Filter On	2.56	Yes
2	Jul 03	Filter Off	Oct 03	Filter Off	3.55	Yes
3	Jul 03	Lens Off/On & Filter Off	Oct 03	Lens Off/On & Filter Off	3.85	Yes
4	Jul 03	Lens and Filter On	Jan 04	Lens and Filter On	7.86	No
5	Jul 03	Filter Off	Jan 04	Filter Off	5.64	Yes
6	Jul 03	Lens Off/On & Filter Off	Jan 04	Lens Off/On & Filter Off	1.42	Yes
7	Oct 03	Lens and Filter On	Jan 04	Lens and Filter On	9.79	No
8	Oct 03	Filter Off	Jan 04	Filter Off	7.61	Yes
9	Oct 03	Lens Off/On & Filter Off	Jan 04	Lens Off/On & Filter Off	4.69	Yes
10	Oct 03	Filter On	Jan 04	Filter On	4.65	Yes

ii. CanonTwo – From examining the results in Table 4.19 and 4.20, it can be seen that the spatial offset standard deviation (σ_o) values for CanonTwo are even better than those for CanonOne. All comparisons reveal that the IOP sets of all camera configurations are similar to each other. Hence, IOP estimation does not depend on the mounting and removal of the lens and the filter elements for this camera as well.

Table 4.19: Comparison of IOP sets obtained within the same month for CanonTwo with different camera settings

(<u>Note</u>: If σ_o < 7.70 μm, IOP sets considered similar)

ID	IOP Set I		IOP Set II		ROT σ_o (μm)	Similar
	Date	Camera Settings	Date	Camera Settings		
1	Oct 03	Lens and Filter On	Oct 03	Filter Off	0.99	Yes
2	Oct 03	Filter Off	Oct 03	Lens Off/On & Filter Off	2.05	Yes
3	Oct 03	Lens Off/On & Filter Off	Oct 03	Filter On	2.40	Yes
4	Jan 04	Lens and Filter On	Jan 04	Filter Off	4.01	Yes
5	Jan 04	Filter Off	Jan 04	Lens Off/On & Filter Off	0.86	Yes
6	Jan 04	Lens Off/On & Filter Off	Jan 04	Filter On	0.89	Yes

Table 4.20: Stability comparison of IOP sets obtained from different months for CanonTwo with same camera settings

(<u>Note</u>: If σ_o < 7.70 μm, IOP sets considered similar)

ID	IOP Set I		IOP Set II		ROT σ_o (μm)	Similar
	Date	Camera Settings	Date	Camera Settings		
1	Jul 03	Lens and Filter On	Oct 03	Lens and Filter On	2.93	Yes
2	Jul 03	Filter Off	Oct 03	Filter Off	3.93	Yes
3	Jul 03	Lens Off/On & Filter Off	Oct 03	Lens Off/On & Filter Off	5.53	Yes
4	Jul 03	Lens and Filter On	Jan 04	Lens and Filter On	6.26	Yes
5	Jul 03	Filter Off	Jan 04	Filter Off	5.73	Yes
6	Jul 03	Lens Off/On & Filter Off	Jan 04	Lens Off/On & Filter Off	4.80	Yes
7	Oct 03	Lens and Filter On	Jan 04	Lens and Filter On	6.19	Yes
8	Oct 03	Filter Off	Jan 04	Filter Off	3.47	Yes
9	Oct 03	Lens Off/On & Filter Off	Jan 04	Lens Off/On & Filter Off	6.14	Yes
10	Oct 03	Filter On	Jan 04	Filter On	6.85	Yes

iii. SonyF707 – In the month of October 2003, two datasets were captured, one using manual focus and the other using auto focus. In the manual focus mode, the focus was set at infinity, and in the auto focus mode, the focus is expected to be infinity because of a relatively large object distance. Therefore, it is expected that the internal geometry of the camera will not change. This is confirmed by the results provided in Table 4.21 where σ_o is considerably less than two-thirds of a pixel (3.00 μm). Hence, the use of auto or manual focus does not affect the IOP estimation.

Table 4.21: Camera setting comparison of IOP sets for SonyF707

(<u>Note</u>: If $\sigma_o < 3.00$ μm, IOP sets considered similar)

ID	IOP Set I		IOP Set II		ROT	Similar
	Date	Camera Settings	Date	Camera Settings	σ_o (μm)	
1	Oct 03	Auto Focus	Oct 03	Manual Focus	0.69	Yes

4.4.2 Changing the Test Field Size

To test the dependence of the similarity results on the size of the test field, the tests were carried only for the Rollei and SonyF707 cameras in the month of July 2003. As mentioned earlier, the size of the original (big) test field includes twenty-one points and twenty lines while the size of the small test field includes fourteen points and fifteen lines, as shown in Figure 4.10.
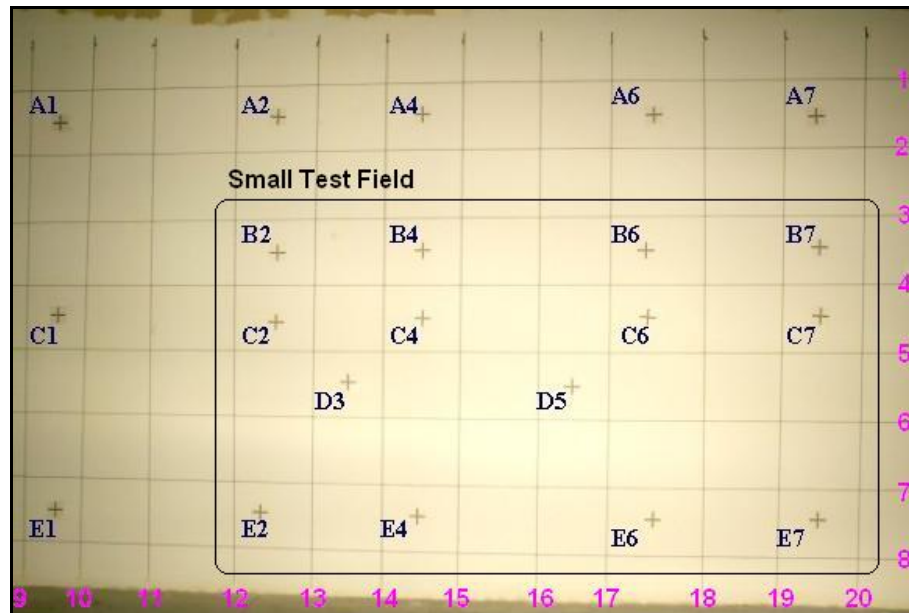
Figure 4.10: The small calibration test field

i. Rollei – From Table 4.22, it can be seen that the standard deviation of the spatial offset (σ_o) is not within the two-third pixel measurement accuracy (3.00 µm) for the first IOP comparison (ID 1) where the grid extent is specified as 90%. This can be explained by the fact that the small test field covers a larger percentage (91.54%) of the image than that of the big test field (67.81%) as revealed by Table 4.2 in Section 4.3. This is a significant difference and is the reason why the estimated IOP from the two datasets are dissimilar when the percentage of image occupied by the test field is specified as 90%. However, when the percentage is specified as 67% (ID 2), the IOP sets pass the test for similarity. This suggests that the test field must occupy as much of the image as possible during the acquisition of all images to avoid inaccurate estimations of the IOP.

Table 4.22: Test field size comparison of IOP sets for Rollei while changing the specified grid extent

(Note: If σ_o < 3.00 µm, IOP sets considered similar)

ID	Date / Specified Grid Extent	Test Field Size		ROT σ_o (µm)	Similar
		IOP Set I / True Coverage	IOP Set II / True Coverage		
1	Jul 03 / 90%	Big / 67.81%	Small / 91.54%	5.92	No
2	Jul 03 / 67%	Big / 67.81%	Small / 91.54%	2.12	Yes

ii. SonyF707 – From Table 4.23, it can be seen that σ_o is well within the two-third pixel measurement accuracy (3.00 µm) for both instances when the grid extents specified in the ROT similarity measure are 90% and 67%. This is because both the big and small test fields cover a relatively good percentage (82.15% and 95.05% respectively) of the image. Hence, the size of the test field did not affect the IOP estimation for this camera. However, it is important to note that the size of test field will play a role in the IOP estimation if it is not big enough to occupy a large percentage of the image while the camera is still focused at infinity.

Table 4.23: Test field size comparison of IOP sets for SonyF707 while changing the specified grid extent

(Note: If RMSE or σ_o < 3.00 µm, IOP sets considered similar)

ID	Date / Specified Grid Extent	Test Field Size		ROT σ_o (µm)	Similar
		IOP Set I / True Coverage	IOP Set II / True Coverage		
1	Jul 03 / 90%	Big / 82.15%	Small / 95.05%	1.46	Yes
2	Jul 03 / 67%	Big / 82.15%	Small / 95.05%	1.35	Yes

4.4.3 Variation of Distortion Parameters Estimated

The MSAT program uses a 6-parameter calibration model (refer to Chapter 2, Section 2.2). It estimates six distortion parameters, which compensate for radial lens distortion, de-centric lens distortion, and affine deformations. However, some of these distortion parameters can be fixed by giving them a low variance value. The reason why it may be a good idea to fix some parameters is that estimating only K_1 might be sufficient. As discussed in Chapter 2, Section 2.2, if more than the required amount of parameters is estimated or in other words, if over-parameterization occurs, it could increase the correlation between unknown parameters, which would likely affect the IOP estimates. In this experiment, the parameters are estimated in one of the following scenarios:

- K_1

- K_1, K_2, P_1

- All parameters ($K_1, K_2, P_1, P_2, A_1, A_2$)

All digital cameras involved in the research with the exception of Nikon288990 were used in this experiment. The results of these tests are provided in Tables 4.24 to 4.31.

i. CanonOne – For this camera, the results presented in Table 4.24 indicate that the IOP sets are similar with the exception of ID 2. This is due to the fact that the test field covers approximately 5-8% less of the image in the imagery captured in October than those captured in other months, which can be seen by comparing Table 4.3 with Tables 4.2, 4.4 and 4.5 in Section 4.3. This lesser coverage results in K_1, K_2

and P_1 not being recovered reliably since the effect of these parameters is manifested on the borders of the image. If the extent of the grid in the stability method (See Chapter 3, Section 3.3.1) is specified as 70% (instead of 90%), σ_o becomes 6.79 μm, which is within the similarity threshold of 7.70 μm. Based on the degree of similarity between the "K_1, K_2, P_1" and "All" sets (IDs 4 and 5), it can be deduced that estimating P_2, A_1, and A_2 is not necessary. Furthermore, the results of all comparisons in Table 4.24 signify that K_1 sufficiently describes the distortion parameters associated with this camera and there is no need to estimate any additional parameters.

Table 4.24: Estimated distortion parameters comparison of IOP sets for CanonOne

(<u>Note</u>: If $\sigma_o < 7.70$ μm, IOP sets considered similar)

ID	IOP Set I		IOP Set II		ROT σ_o (μm)	Similar
	Date	Parameters Estimated	Date	Parameters Estimated		
1	Jul 03	K_1	Jul 03	K_1, K_2, P_1	4.28	Yes
2	Oct 03	K_1	Oct 03	K_1, K_2, P_1	9.87	No
3	Jan 04	K_1	Jan 04	K_1, K_2, P_1	4.13	Yes
4	Jul 03	K_1, K_2, P_1	Jul 03	All	2.00	Yes
5	Oct 03	K_1, K_2, P_1	Oct 03	All	2.60	Yes

ii. CanonTwo – For this camera, the results presented in Table 4.25 reflect the results obtained for CanonOne. All comparisons indicate that the IOP sets are similar and hence, K_1 will sufficiently describe the distortion parameters for this camera and estimating K_2, P_1, P_2, A_1, and A_2 is not necessary.

Table 4.25: Estimated distortion parameters comparison of IOP sets for CanonTwo

(<u>Note</u>: If $\sigma_o < 7.70$ μm, IOP sets considered similar)

ID	IOP Set I		IOP Set II		ROT σ_o (μm)	Similar
	Date	**Parameters Estimated**	**Date**	**Parameters Estimated**		
1	Jul 03	K_1	Jul 03	K_1, K_2, P_1	4.40	Yes
2	Oct 03	K_1	Oct 03	K_1, K_2, P_1	5.87	Yes
3	Jan 04	K_1	Jan 04	K_1, K_2, P_1	5.33	Yes
4	Jul 03	K_1, K_2, P_1	Jul 03	All	1.44	Yes
5	Oct 03	K_1, K_2, P_1	Oct 03	All	2.66	Yes

iii. Rollei – From Table 4.26, it can be seen that the degree of similarity between the "K_1" and the "K_1, K_2, P_1" sets (IDs 1-4) is significantly worse than the degree of similarity between the "K_1, K_2, P_1" and "All" sets (IDs 5 and 6) when the ROT method is used with the extent of the grid specified as 90%. However, this is misleading since it does not mean that more parameters need to be estimated. As shown in Tables 4.2 to 4.5 in Section 4.3, the percentage of the image occupied by the test field ranges from 55% to 67%, which is not enough to accurately derive estimates for the distortion parameters since their effect is manifested on the borders of the image. If the extent of the grid is specified as 60% (as shown in the last two columns of Table 4.26), the comparisons indicate that the IOP sets are similar. This signifies that the IOP sets are similar only in the central portions of the image since K_2 and P_1 were not reliably estimated in the calibration process. Similar to the previous discussion, estimating P_2, A_1, and A_2 is not necessary based on the degree of similarity between the "K_1, K_2, P_1" and "All" sets (IDs 5 and 6).

Table 4.26: Estimated distortion parameters comparison of IOP sets for Rollei

(<u>Note</u>: If σ_o < 3.00 μm, IOP sets considered similar)

ID	IOP Set I		IOP Set II		ROT-90% grid		ROT-60% grid	
	Date	Parameters Estimated	Date	Parameters Estimated	σ_o (μm)	Similar	σ_o (μm)	Similar
1	Jul 03	K_1	Jul 03	K_1, K_2, P_1	5.46	No	2.43	Yes
2	Oct 03	K_1	Oct 03	K_1, K_2, P_1	7.96	No	2.95	Yes
3	Jan 04	K_1	Jan 04	K_1, K_2, P_1	4.95	No	2.43	Yes
4	Feb 04	K_1	Feb 04	K_1, K_2, P_1	4.51	No	1.26	Yes
5	Jul 03	K_1, K_2, P_1	Jul 03	All	2.82	Yes	1.42	Yes
6	Oct 03	K_1, K_2, P_1	Oct 03	All	2.35	Yes	1.00	Yes

iv. SonyF707 – The results presented in Table 4.27 indicate that the IOP sets of all comparisons are similar. Unlike the Rollei camera, the test field occupies a good percentage of the image in the imagery captured by the SonyF707. Therefore, estimating only K_1 is sufficient enough to describe the distortion parameters and it is not necessary to estimate additional parameters.

Table 4.27: Estimated distortion parameters comparison of IOP sets for SonyF707

(<u>Note</u>: If σ_o < 3.00 μm, IOP sets considered similar)

ID	IOP Set I		IOP Set II		ROT σ_o (μm)	Similar
	Date	Parameters Estimated	Date	Parameters Estimated		
1	Jul 03	K_1	Jul 03	K_1, K_2, P_1	2.42	Yes
2	Oct 03	K_1	Oct 03	K_1, K_2, P_1	2.29	Yes
3	Feb 04	K_1	Feb 04	K_1, K_2, P_1	2.01	Yes
4	Jul 03	K_1, K_2, P_1	Jul 03	All	0.13	Yes
5	Oct 03	K_1, K_2, P_1	Oct 03	All	0.73	Yes

v. SonyP9 – For this camera, the degree of similarity between the "K_1, K_2, P_1" and
"All" sets (ID 3) shown in Table 4.28 indicate that estimating P_2, A_1, and A_2 is not
necessary. However, the results of IDs 1 and 2 in Table 4.28 indicate that K_2 and P_1
should be taken into consideration since both comparisons failed the test for
similarity. The percentage of the image occupied by the test field was adequate (75%
to 80%). So, these results signify that K_1 does not adequately describe the distortion
parameters for this camera. Since this is the only tested camera with a telescopic
lens, it is possible that there is a misalignment of its lens elements that causes a
significant distortion (i.e. a de-centric lens distortion – P_1). However, further
investigation is required to confirm whether this is the case.

Table 4.28: Estimated distortion parameters comparison of IOP sets for SonyP9

(Note: If σ_o < 3.00 µm, IOP sets considered similar)

ID	IOP Set I		IOP Set II		ROT σ_o (µm)	Similar
	Date	Parameters Estimated	Date	Parameters Estimated		
1	Jul 03	K_1	Jul 03	K_1, K_2, P_1	4.35	No
2	Jan 04	K_1	Jan 04	K_1, K_2, P_1	3.51	No
3	Jul 03	K_1, K_2, P_1	Jul 03	All	1.69	Yes

vi. Nikon cameras – The experimental results in Table 4.29 reveal that the σ_o value of
the IOP comparisons between "K_1 free" and "K_1, K_2, P_1" sets for all cameras fell
within 0.61 and 1.95 µm, which are less than the two-third pixel image coordinate
measurement accuracy of 2.1 µm. Hence, this indicates that the distortion parameters

associated with the cameras will be sufficiently described by the radial lens distortion parameter (K_1).

Table 4.29: Estimated distortion parameters comparison of IOP sets for Nikon cameras

(<u>Note</u>: If $\sigma_o < 2.10$ μm, IOP sets considered similar)

ID	Camera	IOP Set I		IOP Set II		ROT σ_o (μm)	Similar
		Date	Parameters Estimated	Date	Parameters Estimated		
1	Nikon288616	Jan 04	K_1	Jan 04	K_1, K_2, P_1	0.61	Yes
2	Nikon288894	Feb 04	K_1	Feb 04	K_1, K_2, P_1	1.06	Yes
3	Nikon288895	Jan 04	K_1	Jan 04	K_1, K_2, P_1	1.61	Yes
4	Nikon288896	Feb 04	K_1	Feb 04	K_1, K_2, P_1	1.95	Yes

4.5 Comparison of Similarity Measures

This section examines the effect of implementing different similarity measures on the IOP comparison results. It particularly looks into the stability of a Nikon camera that fails the test of stability according to the ZROT and ROT methods, but may not under the SPR method depending on the terrain chosen. The ZROT and ROT methods take two parameters into consideration before computing the similarity measure: the grid dimension and the grid extent. The SPR method takes these same two parameters into consideration, but also considers the height from the perspective center and a height variation parameter. The height variation parameter essentially represents the average variation in the terrain height. For the SPR method, since the two bundles are compared by checking their fit at a given object space, the height variation of the object points and the height of the exposure stations must be specified.

For the experiment in Table 4.30, an IOP comparison was first done using the ZROT and ROT methods for the Nikon288616. As previously mentioned, the IOP sets are considered dissimilar according to both these methods (RMSE = 8.04 μm for ZROT and σ_o = 6.18 μm for ROT) since both measures are well above the required image coordinate measurement accuracy of 2.1 μm. However, when the SPR method is implemented, the results differ depending on the chosen height variation. For the SPR method, two extreme object space configurations were used where the flying height was specified as 1000 m. The first object space represented a hilly terrain with a height variation of ± 800 m and the second object space represented a flat terrain with a height variation of ± 100 m. For the hilly terrain, the standard deviation of the spatial offset (σ_o) was 6.19 μm, which is close to that estimated by the ROT method (6.18 μm). However, for the flat terrain, σ_o was only 0.67 μm, which is well below the threshold for similarity.

These results can be explained by the estimated position and orientation components of the origins of the two bundles from the adjustment. As shown in Table 4.30, in the ZROT method, there is no shift or rotation and that is why it yielded the strictest measure of similarity. In the ROT method, it can be seen that the position remains fixed but the orientation of the bundle has changed to compensate for the differences in IOP, which explains why its measure of similarity is more relaxed than that of ZROT's. When the SPR method with a hilly terrain is used, the high variation in height of the terrain with respect to the flying height would decouple any correlation between the IOP and EOP. Thus, the position of the bundle will not significantly change as can be seen by the small shift components between the origins of the two bundles in Table 4.30. In the case of a

flat terrain, there would be high correlations between the IOP and EOP. As a result, although the two bundles may be significantly different from each other, the position of the bundle will adapt to absorb the differences between the two IOP sets to produce a good fit at the object space as can be seen by the bigger shift components between the origins of the two bundles in Table 4.30. Therefore, for the SPR method, the type of terrain should be chosen in such a way that it is similar to the expected object space to be photographed by the calibrated camera.

Table 4.30: Comparison of similarity measures for Nikon288616

(<u>Note</u>: If RMSE or σ_o < 2.10 µm, IOP sets considered similar)

Position & Orientation of the Bundle	ZROT (RMSE = 8.04 µm)	ROT (σ_o = 6.18 µm)	SPR	
			Hilly: ±800 m (σ_o = 6.19 µm)	Flat: ±100 m (σ_o = 0.67 µm)
X_0 (m)	0.000 ± 0.000	0.000 ± 0.000	0.001 ± 0.000	-0.139 ± 0.004
Y_0 (m)	0.000 ± 0.000	0.000 ± 0.000	0.001 ± 0.000	0.002 ± 0.004
Z_0 (m)	0.000 ± 0.000	0.000 ± 0.000	0.003 ± 0.001	3.635 ± 0.002
ω (″)	0.00 ± 0.00	-37.94 ± 0.89	-38.12 ± 1.25	-34.99 ± 0.84
ϕ (″)	0.00 ± 0.00	176.68 ± 0.87	176.54 ± 1.22	146.97 ± 0.78
κ (″)	0.00 ± 0.00	-0.40 ± 3.09	-0.46 ± 4.32	-0.33 ± 0.33

As shown by the results above, different constraints on the position and orientation of the bundles have different implications on the degree of similarity. These constraints in the similarity measures can also give us an indication of which one will be applicable in the reconstruction of an object space where different geo-referencing techniques are implemented. The details of this premise will be discussed in the following chapter.

CHAPTER 5

STABILITY MEASURES AND GEO-REFERENCING TECHNIQUES

5.1 Introduction

The four measures of similarity discussed in Chapter 3 limit the position and orientation of the bundles in a different way. Hence, each method will be applicable for a specific geo-referencing technique. In the MIS method, the principal distance is ignored while evaluating the degree of similarity and hence, is not considered. In the ZROT method, the two IOP bundles are assumed to have parallel image coordinate systems with no shifts or rotation allowed between them. This method would be ideal for direct geo-referencing with GPS and INS data since it imposes the same constraints where the position and attitude of the bundles are fixed. The ROT method allows rotation between the bundles while still maintaining the same perspective center, which is similar to the case where only GPS data is used in the bundle adjustment since GPS data would only fix the position of the bundles and have no constraint on their orientation. In the SPR method, both spatial and rotational offsets are permitted, which makes it ideal for indirect geo-referencing with ground control points since the position and attitude of the bundles are not fixed and can be estimated in the adjustment. These constraints imposed in the

similarity measures and by the geo-referencing techniques are summarized in Tables 5.1 and 5.2.

Table 5.1: Constraints of stability analysis measures on the reconstructed bundles

Stability Method	Constraints	
ZROT	Shift	✗
	Rotation	✗
ROT	Shift	✗
	Rotation	✓
SPR	Shift	✓
	Rotation	✓

Table 5.2: Constraints imposed by different geo-referencing techniques

Geo-referencing Technique	Constraints	
Direct - GPS/INS	Shift	✗
	Rotation	✗
Direct – GPS	Shift	✗
	Rotation	✓
Indirect – GCP	Shift	✓
	Rotation	✓

5.2 Hypothesis Description

The foremost issue being addressed is whether two sets of IOP are similar. If the IOP sets are similar, the object space reconstructed using one IOP set will be equivalent to the object space reconstructed using the other IOP set. As per the discussion in the previous section, there are different measures of similarity each with its own constraints. Likewise,

there are different geo-referencing techniques that can be implemented in the reconstruction process each with its own constraints. Based on corresponding constraints, each similarity measure can be used for a certain geo-referencing technique (i.e. ZROT for direct geo-referencing using GPS/INS since compared bundles are fixed in position and orientation; ROT for direct geo-referencing using GPS since compared bundles are fixed in position but allowed to rotate; SPR for indirect geo-referencing since compared bundles are allowed to both shift and rotate). If the IOP sets are similar according to a certain similarity method, the relative quality of the object space that is reconstructed based on the corresponding geo-referencing technique using either IOP set will also be similar. For example, if two IOP sets are deemed similar according to the SPR method, the corresponding geo-referencing technique to be used in reconstruction will be indirect geo-referencing. Hence, the object space that is reconstructed based on indirect geo-referencing using either IOP set will be of similar quality.

This correspondence between the stability methods and the geo-referencing techniques is the basis for the hypothesis being tested in this research. The procedure to test the hypothesis involves the simulation of an image block using one set of IOP, a reconstruction of the object space of the simulated block using a different set of IOP, and the comparison of the true object space with the reconstructed one. This three-step process is illustrated in Figure 5.1 and can be described as follows:

i. For a given object space, simulate an image block using one set of IOP (denoted as IOP_I in these tests) by carrying out the following:

- Generate a DEM (i.e. generate estimates for the ground coordinates of points in the DEM).

- Provide estimates for the position and orientation of the images.

- Generate image coordinate measurements of points in the DEM.

ii. Reconstruct the object space of the simulated block using the same or a different set of IOP that was used in the simulation (IOP_I, IOP_{II}, or IOP_{III} in these tests). The reconstruction is done using the following scenarios:

- Indirect geo-referencing using GCP (±10cm accuracy)

- Direct geo-referencing using GPS observations (±4cm accuracy)

- Direct geo-referencing using GPS/INS observations (±4cm / ±7″ accuracy)

iii. Compute the root mean square error (RMSE) difference between the 3-D ground coordinates of the tie/check points of the true object space and those of the reconstructed object space. These values ($RMSE_I$, $RMSE_{II}$, or $RMSE_{III}$ in Figure 5.1) represent the quality or accuracy of the reconstructed object space.
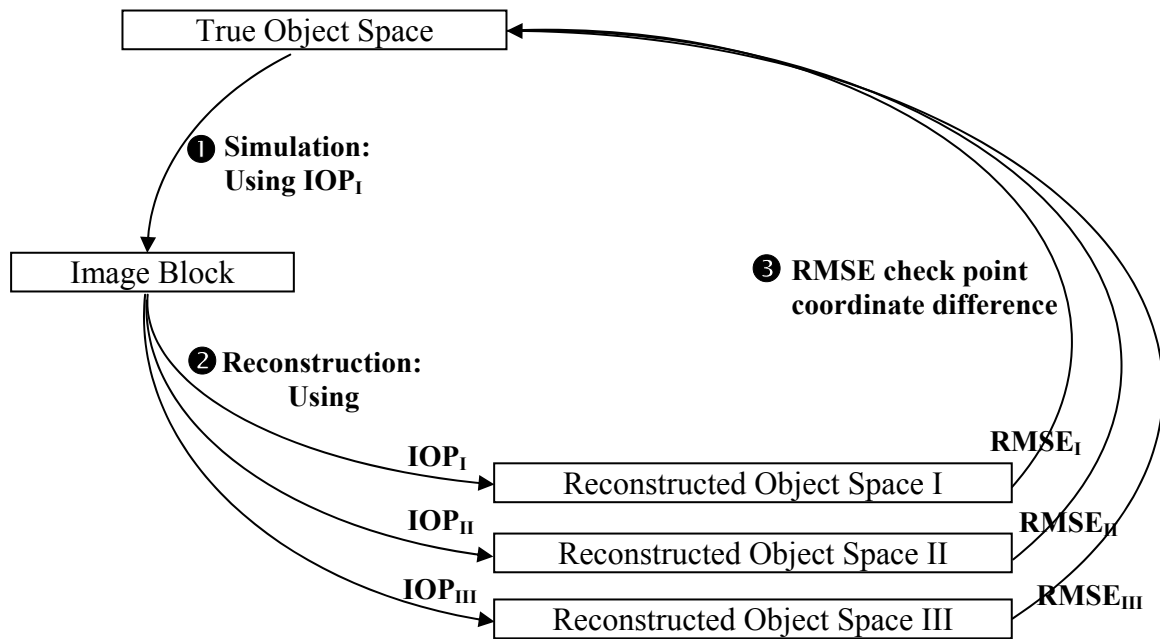
Figure 5.1: Testing procedure to verify the application of different stability analysis methods for different geo-referencing techniques

The three IOP sets (IOP_I, IOP_{II}, and IOP_{III}) are used in the reconstruction of the object space (i.e. three reconstructions performed) for each of the geo-referencing scenarios described above for a total of nine reconstructions for a particular image block. IOP_{II} and IOP_{III} are picked in such a way that IOP_{II} should have a closer degree of similarity to IOP_I (i.e. the IOP set used in simulation) than IOP_{III}. Table 5.3 shows the degree of similarity between these three IOP sets based on the ZROT, ROT and SPR similarity measures.

Table 5.3: Similarity of IOP sets (IOP_I, IOP_{II} and IOP_{III}) used in reconstruction to the

IOP set used in simulation (IOP_I)

Similarity Measure	Similarity of simulation IOP set to reconstruction IOP sets		
	IOP_I	IOP_{II}	IOP_{III}
ZROT	Same	Different	Different
ROT	Same	Similar	Different
SPR	Same	Similar	Similar

Based on this configuration of IOP sets, it is expected that using a certain IOP set in the reconstruction procedure will yield an object space whose quality will be dependent on the degree of similarity between the true IOP set used in simulation and the IOP set used in reconstruction. As mentioned earlier, the quality of the object space is given by the RMSE coordinate difference of the check points of the true object space and those of the reconstructed object space. As illustrated in Figure 5.2, the expected RMSE results for the three sets of IOP (IOP_I, IOP_{II} and IOP_{III}) are provided below.

- Reconstructed object space using IOP_I – Since this is the same set that is used in the simulation, the expected RMSE of the check points is used as a base for comparison to the RMSE results of the other IOP sets.

- Reconstructed object space using IOP_{II} – The position and orientation of the bundles are fixed in ZROT, which is analogous with the constraints in the direct geo-referencing technique where GPS/INS data are available. Based on the similarity results given in Table 5.3, it can be seen that IOP_{II} is considered different from IOP_I according to the ZROT method. Hence, in Figure 5.2, *H* should be

higher than *G*. However, since IOP_{II} is considered similar to IOP_I according to the ROT and SPR methods, *B* and *E* should be close to *A* and *D*, respectively.

- Reconstructed object space using IOP_{III} – Based on the similarity results given in Table 5.3, it can be seen that IOP_{III} is considered different from IOP_I according to the ZROT and ROT methods. Hence, in Figure 5.2, *I* and *F* should be higher than *G* and *D*, respectively. It is also expected that *I* will be higher than *H* because IOP_{III} has a lesser degree of similarity to IOP_I (the simulation IOP set) than does IOP_{II}. As was the case with IOP_{II}, *C* should remain close to *A* since IOP_I and IOP_{III} are considered similar according to the SPR method.
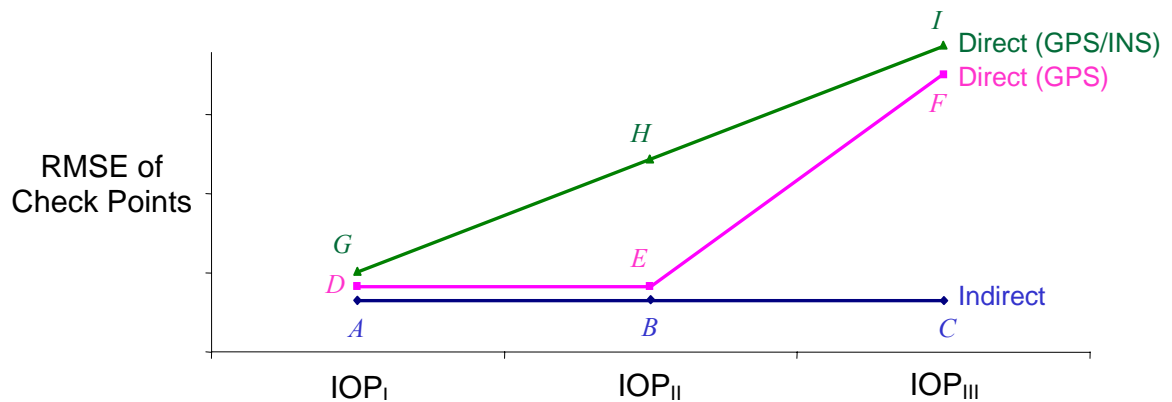
Figure 5.2: Expected quality of the reconstructed object space for different sets of IOP and different geo-referencing methodologies used in reconstruction

5.3 Experiment Results

There were two cameras used for the tests described in the previous section – a 9 inch by 9 inch (large format) frame camera and a Sony F707 (small/medium format) camera. For

these cameras, different configurations of the image block were implemented in the simulation.

i. The size of the image block was changed:

- 6 image block – 6 images in 2 flight lines

- 32 image block – 32 images in 4 flight lines

ii. The orientation of the images was altered:

- Portrait images

- Landscape images

1.   9 x 9 inch Frame (large format) camera:

The portrait and landscape orientations did not apply for the 9 x 9 inch camera since it produces images that are in a square format. The values for the three IOP sets of the frame camera have been manually created according to the degrees of similarity described in the previous section. These values are listed in Table 5.4 and their degrees of similarity to IOP_I are given in Table 5.5.

Table 5.4: IOP values for the 9 x 9 inch Frame camera

(<u>Note</u>: Pixel size of the 9 x 9 inch Frame camera: 10.0 μm)

IOP Value	Three IOP sets of the 9 x 9 inch Frame		
	IOP_I	IOP_{II}	IOP_{III}
x_p (mm)	0.000000	-0.031333	0.015000
y_p (mm)	0.000000	-0.032141	0.012000
c (mm)	150.00000	150.01095	149.85120
K_1 (mm)	0.00	0.00	0.00

Table 5.5: Similarity of the three IOP sets used in reconstruction (IOP_I, IOP_{II}, and IOP_{III})

to the IOP set used in simulation (IOP_I) for the 9 x 9 inch Frame camera

(<u>Note</u>: If RMSE or $\sigma_o < 7.50$ μm, IOP sets considered similar)

Similarity Measure	Similarity of simulation IOP set to reconstruction IOP sets		
	IOP_I (RMSE or σ_o)	IOP_{II} (RMSE or σ_o)	IOP_{III} (RMSE or σ_o)
ZROT	Same (RMSE = 0.00 μm)	Different (RMSE = 32.04 μm)	Different (RMSE = 61.15 μm)
ROT	Same ($\sigma_o = 0.00$ μm)	Similar ($\sigma_o = 7.27$ μm)	Different ($\sigma_o = 59.73$ μm)
SPR	Same ($\sigma_o = 0.00$ μm)	Similar ($\sigma_o = 2.92$ μm)	Similar ($\sigma_o = 6.29$ μm)

As mentioned earlier, there are nine configurations or reconstructions performed for each image block. Other than the RMSE of the check points, the IOP values before and after the adjustment and the difference between the original EOP (from the simulation) and the estimated EOP (from the reconstruction) are reported. These values are provided to check any possible changes in the IOP and EOP after the adjustment is done. These reconstruction results of the two image blocks of the 9 x 9 inch Frame camera are provided below:

i. 6 image block − Figure 5.3 is a graph that shows the RMSE of the check points for all reconstructions using the three geo-referencing techniques and the three sets of IOP. The complete results (i.e. IOP change in the adjustment, RMSE of check points, and EOP difference) are provided in Tables 5.6 to 5.14.

   • For the indirect geo-referencing method, the RMSE of the check points are equivalent for all three IOP sets as shown by the results in Figure 5.3. Since all

three IOP sets are similar to the simulation IOP set (IOP_I) according to SPR where spatial and rotational offsets are allowed (See Table 5.5), the RMSE values should be close to the base comparison of IOP_I (0.160 m) for the indirect geo-referencing method. This is because spatial and rotational offsets are allowed in indirect geo-referencing and hence, the EOP (i.e. the position and orientation) of the bundles are expected to change in order to compensate for the IOP differences (See Tables 5.6 to 5.8).

- For direct geo-referencing with GPS, the use of IOP_I and IOP_{II} expectedly results in relatively equal RMSE values (0.266 m and 0.358 m, respectively) since these two sets are similar according to ROT where only rotational offsets are permitted (as in the case of direct geo-referencing with GPS). On the other hand, the use of IOP_{III} yields an RMSE that is higher (0.827 m) since IOP_{III} is not similar to IOP_I according to the ROT method. Based on the EOP differences (given by the mean and RMSE) provided in Tables 5.9 to 5.11, it can be seen that there was a change in the rotation angles (ω, φ, κ) and a relatively small shift in position (X_O, Y_O, Z_O).

- For direct geo-referencing with GPS/INS, the use of IOP_{II} and IOP_{III} results in RMSE values that are higher than the base comparison of IOP_I (0.131 m). However, it should be noted that the value obtained from IOP_{III} (0.989 m) is significantly larger than that from IOP_{II} (0.397 m). This is due to the fact that IOP_{III} has a lesser degree of similarity to IOP_I than does IOP_{II} according to the ZROT method (61.15 μm compared to 32.04 μm as shown in Table 5.5). In Tables 5.12 to 5.14, it can also be seen that the EOP has not significantly changed

(i.e. there is a low EOP difference) and reflects the 4 cm and 7″ measurement noise of the GPS and INS systems.
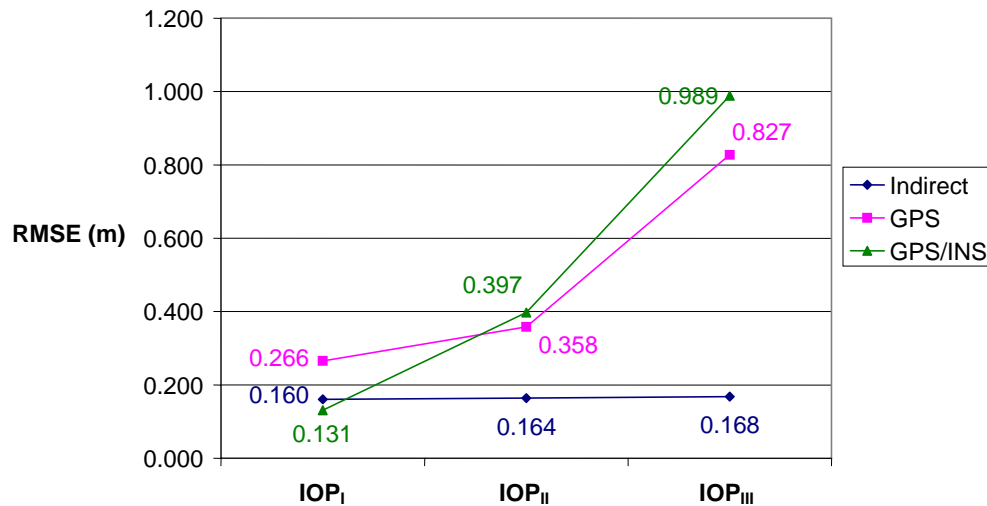
Figure 5.3: Quality of the reconstructed object space for the 6 image block of the 9 x 9 inch Frame camera

Table 5.6: Reconstruction results for the 6 image block of the 9 x 9 inch Frame camera - Indirect geo-referencing using IOP_I

		x_p (mm)		y_p (mm)		c (mm)	
Block Adjustment	IOP before	0.000		0.000		150.0000	
	IOP after	-6.240e-05		-7.551e-06		150.0000	
	σ_o	4.97e-03 mm					
Check Point Analysis		X (m)		Y (m)		Z (m)	
	Mean ± std_dev	0.013 ± 0.060		-0.030 ± 0.048		0.072 ± 0.119	
	RMSE	0.061		0.057		0.137	
EOP Analysis		ω (″)	φ (″)	κ (″)	X_O (m)	Y_O (m)	Z_O (m)
	Mean	9	-17	-4	-0.064	-0.082	0.093
	RMSE	20	22	15	0.099	0.123	0.102

Table 5.7: Reconstruction results for the 6 image block of the 9 x 9 inch Frame camera -

Indirect geo-referencing using IOP_{II}

		x_p (mm)		y_p (mm)		c (mm)		
Block Adjustment	IOP before	-3.133e-02		-3.214e-02		150.0109		
	IOP after	-3.130e-02		-3.213e-02		150.0109		
	σ_o	4.95e-03 mm						
Check Point Analysis		X (m)		Y (m)		Z (m)		
	Mean ± std_dev	0.011 ± 0.061		-0.032 ± 0.050		0.078 ± 0.117		
	RMSE	0.061		0.059		0.140		
EOP Analysis		ω (")	φ (")	κ (")	X_O (m)	Y_O (m)	Z_O (m)	
	Mean	8	-15	-5	-0.056	-0.077	0.025	
	RMSE	21	23	15	0.180	0.163	0.053	

Table 5.8: Reconstruction results for the 6 image block of the 9 x 9 inch Frame camera -

Indirect geo-referencing using IOP_{III}

		x_p (mm)		y_p (mm)		c (mm)		
Block Adjustment	IOP before	1.500e-02		1.200e-02		149.8512		
	IOP after	1.489e-02		1.198e-02		149.8512		
	σ_o	5.09e-03 mm						
Check Point Analysis		X (m)		Y (m)		Z (m)		
	Mean ± std_dev	0.013 ± 0.063		-0.030 ± 0.049		0.034 ± 0.142		
	RMSE	0.064		0.057		0.144		
EOP Analysis		ω (")	φ (")	κ (")	X_O (m)	Y_O (m)	Z_O (m)	
	Mean	8	-22	-4	-0.091	-0.074	1.047	
	RMSE	26	26	15	0.164	0.204	1.048	

Table 5.9: Reconstruction results for the 6 image block of the 9 x 9 inch Frame camera -

Direct geo-referencing (with GPS) using IOP_I

		x_p (mm)		y_p (mm)		c (mm)	
Block Adjustment	IOP before	0.000		0.000		150.0000	
	IOP after	-1.650e-04		-7.205e-10		150.0000	
	σ_o	5.22e-03 mm					
Check Point Analysis		X (m)		Y (m)		Z (m)	
	Mean ± std_dev	0.029±0.101		-0.025±0.135		0.187±0.081	
	RMSE	0.104		0.136		0.203	
EOP Analysis		ω (″)	φ (″)	κ (″)	X_O (m)	Y_O (m)	Z_O (m)
	Mean	-1	-3	-3	0.012	-0.016	0.021
	RMSE	14	17	9	0.038	0.051	0.029

Table 5.10: Reconstruction results for the 6 image block of the 9 x 9 inch Frame camera

- Direct geo-referencing (with GPS) using IOP_{II}

		x_p (mm)		y_p (mm)		c (mm)	
Block Adjustment	IOP before	-3.133e-02		-3.214e-02		150.0109	
	IOP after	-3.092e-02		-3.214e-02		150.0109	
	σ_o	5.43e-03 mm					
Check Point Analysis		X (m)		Y (m)		Z (m)	
	Mean ± std_dev	0.027±0.155		-0.051±0.149		0.255±0.123	
	RMSE	0.156		0.156		0.282	
EOP Analysis		ω (″)	φ (″)	κ (″)	X_O (m)	Y_O (m)	Z_O (m)
	Mean	-5	-3	31	0.012	-0.016	0.021
	RMSE	32	24	32	0.038	0.064	0.041

Table 5.11: Reconstruction results for the 6 image block of the 9 x 9 inch Frame camera

- Direct geo-referencing (with GPS) using IOP_{III}

		x_p (mm)		y_p (mm)		c (mm)	
Block Adjustment	IOP before	1.500e-02		1.200e-02		149.8512	
	IOP after	1.456e-02		1.200e-02		149.8512	
	σ_o	5.47e-03 mm					
Check Point Analysis		X (m)		Y (m)		Z (m)	
	Mean ± std_dev	0.031±0.133		-0.013±0.142		-0.798±0.097	
	RMSE	0.135		0.141		0.804	
EOP Analysis		ω (″)	φ (″)	κ (″)	X_O (m)	Y_O (m)	Z_O (m)
	Mean	0	-2	-19	0.012	-0.016	0.021
	RMSE	31	17	21	0.041	0.049	0.030

Table 5.12: Reconstruction results for the 6 image block of the 9 x 9 inch Frame camera

- Direct geo-referencing (with GPS/INS) using IOP_I

		x_p (mm)		y_p (mm)		c (mm)	
Block Adjustment	IOP before	0.000		0.000		150.0000	
	IOP after	-1.382e-04		2.826e-04		150.0000	
	σ_o	5.15e-03 mm					
Check Point Analysis		X (m)		Y (m)		Z (m)	
	Mean ± std_dev	0.023±0.040		-0.014±0.058		0.067±0.084	
	RMSE	0.046		0.059		0.107	
EOP Analysis		ω (″)	φ (″)	κ (″)	X_O (m)	Y_O (m)	Z_O (m)
	Mean	1	-1	-3	0.012	-0.016	0.021
	RMSE	4	6	5	0.028	0.034	0.023

Table 5.13: Reconstruction results for the 6 image block of the 9 x 9 inch Frame camera

- Direct geo-referencing (with GPS/INS) using IOP_{II}

		x_p (mm)		y_p (mm)		c (mm)	
Block Adjustment	IOP before	-3.133e-02		-3.214e-02		150.0109	
	IOP after	-2.921e-02		-3.095e-02		150.0109	
	σ_o	7.29e-03 mm					
Check Point Analysis		X (m)		Y (m)		Z (m)	
	Mean ± std_dev	0.024±0.128		-0.021±0.194		0.310±0.090	
	RMSE	0.129		0.194		0.322	
EOP Analysis		ω (″)	φ (″)	κ (″)	X_O (m)	Y_O (m)	Z_O (m)
	Mean	1	-1	4	0.012	-0.016	0.021
	RMSE	7	17	6	0.105	0.032	0.032

Table 5.14: Reconstruction results for the 6 image block of the 9 x 9 inch Frame camera

- Direct geo-referencing (with GPS/INS) using IOP_{III}

		x_p (mm)		y_p (mm)		c (mm)	
Block Adjustment	IOP before	1.500e-02		1.200e-02		149.8512	
	IOP after	1.378e-02		1.194e-02		149.8512	
	σ_o	5.55e-03 mm					
Check Point Analysis		X (m)		Y (m)		Z (m)	
	Mean ± std_dev	0.022±0.051		-0.011±0.049		-0.982±0.097	
	RMSE	0.055		0.050		0.986	
EOP Analysis		ω (″)	φ (″)	κ (″)	X_O (m)	Y_O (m)	Z_O (m)
	Mean	1	-1	-7	0.012	-0.016	0.021
	RMSE	4	4	8	0.055	0.044	0.023

ii. 32 image block – The complete analysis results of the reconstruction are provided in Tables 5.15 to 5.23. With regard to the RMSE check point analysis, the graph in

Figure 5.4 shows a trend similar to that of the 6 image block only for the indirect and direct with GPS geo-referencing techniques.

- For the indirect geo-referencing method, the RMSE of the check points are equivalent for all three IOP sets (0.108 m, 0.106 m, and 0.141 m).

- For direct geo-referencing with GPS, the use of IOP_I and IOP_{II} yields relatively equal RMSE values (0.089 m and 0.168 m, respectively) while the use of IOP_{III} is higher (1.015 m).

- For the direct geo-referencing technique with GPS/INS, the RMSE value for IOP_{II} is relatively equivalent (0.145 m) to the RMSE value for IOP_I (0.085 m), which was not expected since IOP_{II} is considered dissimilar to IOP_I according to the ZROT method (RMSE = 32.04 μm as shown in Table 5.5). This can be rationalized by the fact that the object space of a 32 image block is being reconstructed as opposed to a 6 image block. The 32 image block has significantly better geometry with respect to the bundles in space. Therefore, since the dissimilarity between IOP_I and IOP_{II} is caused by the difference in their corresponding principal point coordinate values (x_p, y_p), the bundle adjustment will instigate the derivation of estimates of x_p and y_p that will come close to the true values, which can be seen in Table 5.22. This change in the principal point coordinates results in a better fit of the bundles and a very accurate reconstructed object space. In the case of IOP_{III}, its dissimilarity with IOP_I is caused by the difference in their corresponding principal distances. Although the values for x_p and y_p improved (See Table 5.23), the principal distance did not. This is because there is no ground truth, which is required to allow the principal distance to

approach the true value in the bundle adjustment. For this reason, the RMSE values obtained from the use of IOP$_{III}$ remains higher (1.012 m and 1.015 m) even though a 32 image block is implemented.
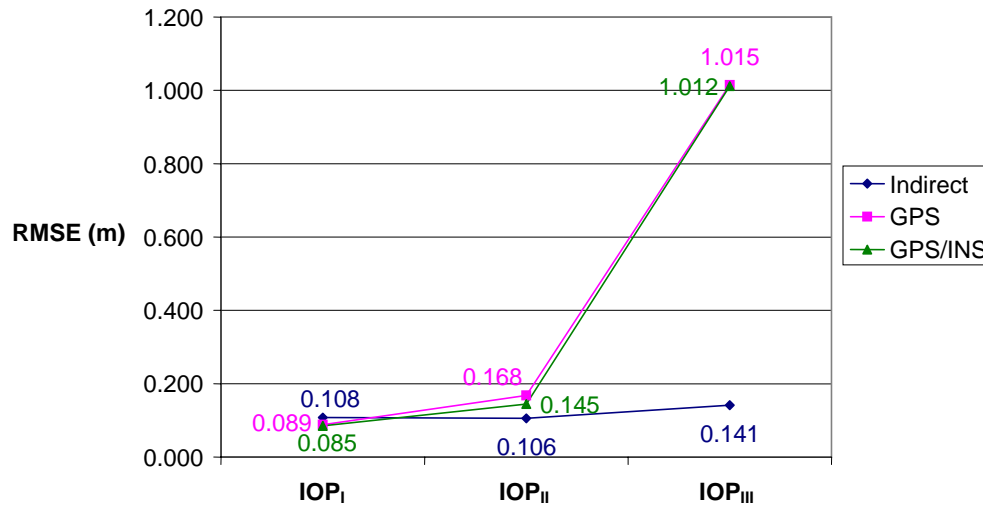
Figure 5.4: Quality of the reconstructed object space for the 32 image block of the 9 x 9 inch Frame camera

Table 5.15: Reconstruction results for the 32 image block of the 9 x 9 inch Frame camera - Indirect geo-referencing using IOP$_I$

		x_p (mm)		y_p (mm)		c (mm)	
Block Adjustment	IOP before	0.000		0.000		150.0000	
	IOP after	2.388e-05		-2.551e-05		150.0000	
	σ_o	5.07e-03 mm					
Check Point Analysis		X (m)		Y (m)		Z (m)	
	Mean ± std_dev	0.010±0.045		-0.005±0.046		-0.022±0.083	
	RMSE	0.046		0.046		0.086	
EOP Analysis		ω (″)	φ (″)	κ (″)	X_O (m)	Y_O (m)	Z_O (m)
	Mean	2	4	3	0.026	-0.011	-0.022
	RMSE	12	14	8	0.087	0.085	0.064

Table 5.16: Reconstruction results for the 32 image block of the 9 x 9 inch Frame camera

- Indirect geo-referencing using IOP$_{II}$

		x_p (mm)		y_p (mm)		c (mm)	
Block Adjustment	IOP before	-3.133e-02		-3.214e-02		150.0109	
	IOP after	-3.053e-02		-3.200e-02		150.0109	
	σ_o	5.16e-03 mm					
Check Point Analysis		X (m)		Y (m)		Z (m)	
	Mean ± std_dev	0.010±0.047		-0.003±0.048		-0.012±0.081	
	RMSE	0.048		0.048		0.081	
EOP Analysis		ω (″)	φ (″)	κ (″)	X_O (m)	Y_O (m)	Z_O (m)
	Mean	0	4	3	0.026	-0.004	-0.086
	RMSE	12	14	8	0.207	0.203	0.103

Table 5.17: Reconstruction results for the 32 image block of the 9 x 9 inch Frame camera

- Indirect geo-referencing using IOP$_{III}$

		x_p (mm)		y_p (mm)		c (mm)	
Block Adjustment	IOP before	1.500e-02		1.200e-02		149.8512	
	IOP after	1.465e-02		1.188e-02		149.8512	
	σ_o	5.09e-03 mm					
Check Point Analysis		X (m)		Y (m)		Z (m)	
	Mean ± std_dev	0.010±0.046		-0.004±0.046		-0.025±0.123	
	RMSE	0.047		0.046		0.125	
EOP Analysis		ω (″)	φ (″)	κ (″)	X_O (m)	Y_O (m)	Z_O (m)
	Mean	5	6	3	0.037	-0.026	0.972
	RMSE	14	17	8	0.147	0.124	0.975

Table 5.18: Reconstruction results for the 32 image block of the 9 x 9 inch Frame camera

- Direct geo-referencing (with GPS) using IOP_I

		x_p (mm)		y_p (mm)		c (mm)	
Block Adjustment	IOP before	0.000		0.000		150.0000	
	IOP after	-3.910e-04		3.075e-05		150.0000	
	σ_o	5.10e-03 mm					
Check Point Analysis		X (m)		Y (m)		Z (m)	
	Mean ± std_dev	-0.001±0.035		0.000±0.043		-0.014±0.068	
	RMSE	0.035		0.043		0.069	
EOP Analysis		ω (″)	φ (″)	κ (″)	X_O (m)	Y_O (m)	Z_O (m)
	Mean	2	0	0	0.000	-0.013	0.000
	RMSE	6	6	6	0.026	0.038	0.020

Table 5.19: Reconstruction results for the 32 image block of the 9 x 9 inch Frame camera

- Direct geo-referencing (with GPS) using IOP_{II}

		x_p (mm)		y_p (mm)		c (mm)	
Block Adjustment	IOP before	-3.133e-02		-3.214e-02		150.0109	
	IOP after	-2.298e-02		-3.154e-02		150.0109	
	σ_o	5.83e-03 mm					
Check Point Analysis		X (m)		Y (m)		Z (m)	
	Mean ± std_dev	0.002±0.069		-0.005±0.068		0.062±0.122	
	RMSE	0.069		0.068		0.137	
EOP Analysis		ω (″)	φ (″)	κ (″)	X_O (m)	Y_O (m)	Z_O (m)
	Mean	1	0	9	0.000	-0.013	0.000
	RMSE	44	12	14	0.073	0.040	0.032

Table 5.20: Reconstruction results for the 32 image block of the 9 x 9 inch Frame camera

- Direct geo-referencing (with GPS) using IOP_{III}

Block Adjustment		x_p (mm)		y_p (mm)		c (mm)		
	IOP before	1.500e-02		1.200e-02		149.8512		
	IOP after	1.041e-02		1.183e-02		149.8512		
	σ_o	5.32e-03 mm						
Check Point Analysis		X (m)		Y (m)		Z (m)		
	Mean ± std_dev	-0.002±0.044		0.003±0.051		-1.009±0.093		
	RMSE	0.044		0.051		1.013		
EOP Analysis		ω (″)	φ (″)	κ (″)	X_O (m)	Y_O (m)	Z_O (m)	
	Mean	3	0	-4	0.000	-0.013	0.000	
	RMSE	16	8	7	0.040	0.039	0.022	

Table 5.21: Reconstruction results for the 32 image block of the 9 x 9 inch Frame camera

- Direct geo-referencing (with GPS/INS) using IOP_I

Block Adjustment		x_p (mm)		y_p (mm)		c (mm)		
	IOP before	0.000		0.000		150.0000		
	IOP after	-2.982e-04		-2.060e-04		150.0000		
	σ_o	5.08e-03 mm						
Check Point Analysis		X (m)		Y (m)		Z (m)		
	Mean ± std_dev	0.000±0.029		-0.014±0.038		-0.002±0.069		
	RMSE	0.029		0.040		0.069		
EOP Analysis		ω (″)	φ (″)	κ (″)	X_O (m)	Y_O (m)	Z_O (m)	
	Mean	0	0	-1	0.000	-0.013	0.000	
	RMSE	4	4	4	0.022	0.028	0.016	

Table 5.22: Reconstruction results for the 32 image block of the 9 x 9 inch Frame camera

- Direct geo-referencing (with GPS/INS) using IOP_{II}

		x_p (mm)		y_p (mm)		c (mm)		
Block Adjustment	IOP before	-3.133e-02		-3.214e-02		150.0109		
	IOP after	-2.031e-02		-2.333e-02		150.0109		
	σ_o	6.48e-03 mm						
Check Point Analysis		X (m)		Y (m)		Z (m)		
	Mean ± std_dev	0.001±0.052		-0.013±0.056		0.097±0.074		
	RMSE	0.052		0.058		0.122		
EOP Analysis		ω (″)	φ (″)	κ (″)	X_O (m)	Y_O (m)	Z_O (m)	
	Mean	0	0	3	0.000	-0.013	0.000	
	RMSE	12	9	5	0.089	0.076	0.022	

Table 5.23: Reconstruction results for the 32 image block of the 9 x 9 inch Frame camera

- Direct geo-referencing (with GPS/INS) using IOP_{III}

		x_p (mm)		y_p (mm)		c (mm)		
Block Adjustment	IOP before	1.500e-02		1.200e-02		149.8512		
	IOP after	9.281e-03		8.425e-03		149.8512		
	σ_o	5.42e-03 mm						
Check Point Analysis		X (m)		Y (m)		Z (m)		
	Mean ± std_dev	-0.001±0.035		-0.015±0.045		-1.006±0.089		
	RMSE	0.035		0.048		1.010		
EOP Analysis		ω (″)	φ (″)	κ (″)	X_O (m)	Y_O (m)	Z_O (m)	
	Mean	0	0	-2	0.000	-0.013	0.000	
	RMSE	5	5	5	0.043	0.037	0.016	

2.   **Sony F707 (small/medium format) camera:**

Unlike the 9 x 9 inch Frame camera, image blocks with portrait and landscape orientations were simulated for the Sony F707. The values for the three IOP sets of the Sony camera are listed in Table 5.24 and their degrees of similarity to IOP_I are given in Table 5.25.

Table 5.24: IOP values for the Sony F707 camera

(<u>Note</u>: Pixel size of the Sony F707 camera: 4.0 µm)

IOP Value	Three IOP sets of the Sony F707		
	IOP_I	IOP_{II}	IOP_{III}
x_p **(mm)**	-0.085424	-0.096725	-0.104748
y_p **(mm)**	-0.060568	-0.074012	-0.069825
c (mm)	11.62237	11.61494	11.70275
K_1 **(mm)**	-0.001213	-0.001216	-0.001293

Table 5.25: Similarity of the three IOP sets used in reconstruction to the IOP set used in simulation (IOP_I) for the SonyF707 camera

(<u>Note</u>: If RMSE or σ_o < 3.00 µm, IOP sets considered similar)

Similarity Measure	Similarity of simulation IOP set to reconstruction IOP sets		
	IOP_I (RMSE or σ_o)	IOP_{II} (RMSE or σ_o)	IOP_{III} (RMSE or σ_o)
ZROT	Same (RMSE = 0.00 µm)	Different (RMSE = 12.74 µm)	Different (RMSE = 20.40 µm)
ROT	Same (σ_o = 0.00 µm)	Similar (σ_o = 1.70 µm)	Different (σ_o = 13.83 µm)
SPR	Same (σ_o = 0.00 µm)	Similar (σ_o = 0.45 µm)	Similar (σ_o = 1.97 µm)

There are nine configurations or reconstructions performed for each image block as was the case for the 9 x 9 inch Frame camera. The reconstruction results of the two image blocks of the Sony F707 in portrait orientation are provided below:

i. 6 image block – Figure 5.5 is a graph that shows the RMSE of the check points for the 6 block image of the SonyF707. The complete results (i.e. IOP change in the adjustment, RMSE of check points, and EOP difference) are provided in Tables 5.26 to 5.34. Based on the results shown in Figure 5.5, the RMSE values follow the same trend as the values in the 6 image block of the 9 x 9 inch Frame camera.

    - For the indirect geo-referencing method, the RMSE of the check points are almost equivalent for all three IOP sets (0.976 m, 0.963 m, and 1.339 m). The EOP changed in order to compensate for the IOP differences as can be seen in Tables 5.26 to 5.28.

    - For direct geo-referencing with GPS, the use of IOP_I and IOP_{II} yields relatively equal RMSE values (1.691 m and 1.801 m, respectively) while the use of IOP_{III} yields an RMSE that is much higher (15.277 m) since IOP_{III} has a much lower degree of similarity to IOP_I (13.83 μm as shown in Table 5.25) than do the other two sets. Based on the results in Tables 5.29 to 5.31, it can be seen that there is a significant change in the orientation of the bundles, but no change in position.

    - For direct geo-referencing with GPS/INS, the use of IOP_{II} and IOP_{III} results in RMSE values that are higher than the base comparison of IOP_I (0.928 m) since both these IOP sets are considered dissimilar to the simulation IOP set (IOP_I) according to the ZROT method. As expected, the EOP did not change to

compensate for the IOP differences since the position and attitude of the bundles are fixed by the GPS/INS data (See Tables 5.32 to 5.34).
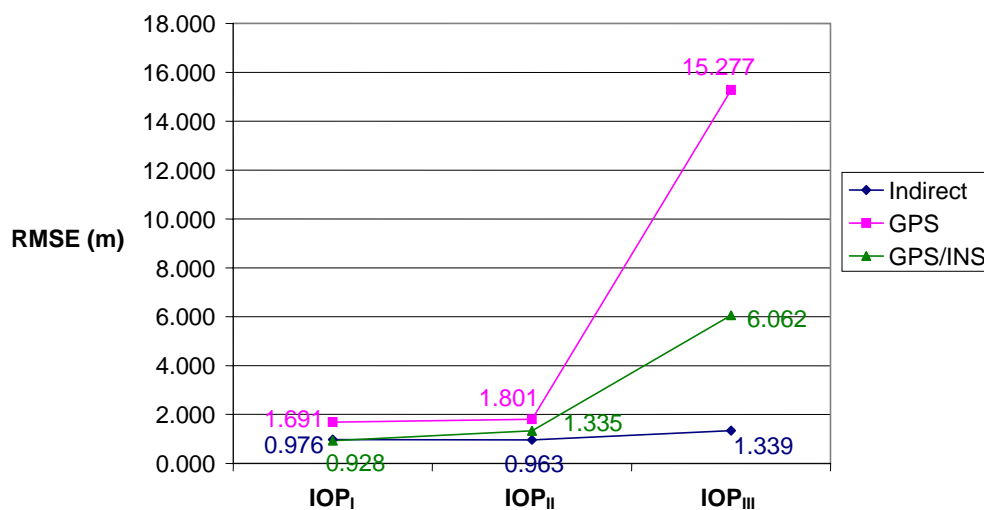
Figure 5.5: Quality of the reconstructed object space for the 6 image block of the SonyF707 camera

Table 5.26: Reconstruction results for the 6 image block of the SonyF707 camera - Indirect geo-referencing using IOP_I

		x_p (mm)		y_p (mm)		c (mm)	
Block Adjustment	IOP before	-8.542e-02		-6.057e-02		11.6224	
	IOP after	-8.533e-02		-6.060e-02		11.6224	
	σ_o	2.21e-03 mm					
Check Point Analysis		X (m)		Y (m)		Z (m)	
	Mean ± std_dev	0.073±0.210		0.019±0.146		-0.055±0.951	
	RMSE	0.220		0.145		0.940	
EOP Analysis		ω (″)	φ (″)	κ (″)	X_O (m)	Y_O (m)	Z_O (m)
	Mean	-55	-191	-5	-0.896	0.252	0.250
	RMSE	161	271	25	1.281	0.810	0.375

Table 5.27: Reconstruction results for the 6 image block of the SonyF707 camera -

Indirect geo-referencing using IOP_{II}

		x_p (mm)		y_p (mm)		c (mm)	
Block Adjustment	IOP before	-9.673e-02		-7.401e-02		11.6149	
	IOP after	-9.656e-02		-7.402e-02		11.6149	
	σ_o	2.23e-03 mm					
Check Point Analysis		X (m)		Y (m)		Z (m)	
	Mean ± std_dev	0.057±0.210		0.011±0.145		-0.032±0.939	
	RMSE	0.215		0.143		0.928	
EOP Analysis		ω (″)	φ (″)	κ (″)	X_O (m)	Y_O (m)	Z_O (m)
	Mean	-70	-208	-9	-0.986	0.324	0.936
	RMSE	201	272	28	1.372	0.968	0.985

Table 5.28: Reconstruction results for the 6 image block of the SonyF707 camera -

Indirect geo-referencing using IOP_{III}

		x_p (mm)		y_p (mm)		c (mm)	
Block Adjustment	IOP before	-1.047e-01		-6.983e-02		11.7028	
	IOP after	-1.045e-01		-6.977e-02		11.7027	
	σ_o	2.52e-03 mm					
Check Point Analysis		X (m)		Y (m)		Z (m)	
	Mean ± std_dev	-0.003±0.206		0.016±0.154		0.778±1.073	
	RMSE	0.204		0.153		1.314	
EOP Analysis		ω (″)	φ (″)	κ (″)	X_O (m)	Y_O (m)	Z_O (m)
	Mean	-9	-297	-11	-1.461	0.044	-5.312
	RMSE	165	436	46	2.228	0.938	5.337

Table 5.29: Reconstruction results for the 6 image block of the SonyF707 camera -

Direct geo-referencing (with GPS) using IOP$_I$

		x_p (mm)		y_p (mm)		c (mm)	
Block Adjustment	IOP before	-8.542e-02		-6.057e-02		11.6224	
	IOP after	-8.500e-02		-6.057e-02		11.6224	
	σ_o	2.25e-03 mm					
Check Point Analysis		X (m)		Y (m)		Z (m)	
	Mean ± std_dev	-0.049±0.398		-0.523±0.403		0.356±1.479	
	RMSE	0.397		0.658		1.506	
EOP Analysis		ω (″)	φ (″)	κ (″)	X_O (m)	Y_O (m)	Z_O (m)
	Mean	-132	14	128	0.012	-0.016	0.021
	RMSE	138	78	155	0.039	0.051	0.052

Table 5.30: Reconstruction results for the 6 image block of the SonyF707 camera -

Direct geo-referencing (with GPS) using IOP$_{II}$

		x_p (mm)		y_p (mm)		c (mm)	
Block Adjustment	IOP before	-9.673e-02		-7.401e-02		11.6149	
	IOP after	-9.614e-02		-7.401e-02		11.6149	
	σ_o	2.35e-03 mm					
Check Point Analysis		X (m)		Y (m)		Z (m)	
	Mean ± std_dev	-0.172±0.745		-0.542±0.570		-0.006±1.450	
	RMSE	0.757		0.782		1.435	
EOP Analysis		ω (″)	φ (″)	κ (″)	X_O (m)	Y_O (m)	Z_O (m)
	Mean	-134	32	297	0.012	-0.016	0.021
	RMSE	232	87	308	0.040	0.051	0.052

Table 5.31: Reconstruction results for the 6 image block of the SonyF707 camera -

Direct geo-referencing (with GPS) using IOP_{III}

		x_p (mm)		y_p (mm)		c (mm)		
Block Adjustment	IOP before	-1.047e-01		-6.983e-02		11.7028		
	IOP after	-1.041e-01		-6.983e-02		11.7028		
	σ_o	2.56e-03 mm						
Check Point Analysis		X (m)		Y (m)		Z (m)		
	Mean ± std_dev	-0.189±2.160		-1.065±3.891		14.448±2.039		
	RMSE	2.146		3.995		14.588		
EOP Analysis		ω (″)	φ (″)	κ (″)	X_O (m)	Y_O (m)	Z_O (m)	
	Mean	-180	32	365	0.012	-0.016	0.021	
	RMSE	501	423	379	0.039	0.051	0.060	

Table 5.32: Reconstruction results for the 6 image block of the SonyF707 camera -

Direct geo-referencing (with GPS/INS) using IOP_I

		x_p (mm)		y_p (mm)		c (mm)		
Block Adjustment	IOP before	-8.542e-02		-6.057e-02		11.6224		
	IOP after	-8.620e-02		-6.003e-02		11.6224		
	σ_o	2.14e-03 mm						
Check Point Analysis		X (m)		Y (m)		Z (m)		
	Mean ± std_dev	0.035±0.169		0.036±0.159		-0.144±0.896		
	RMSE	0.171		0.161		0.898		
EOP Analysis		ω (″)	φ (″)	κ (″)	X_O (m)	Y_O (m)	Z_O (m)	
	Mean	2	-1	-4	0.012	-0.016	0.021	
	RMSE	5	5	7	0.043	0.046	0.051	

Table 5.33: Reconstruction results for the 6 image block of the SonyF707 camera -

Direct geo-referencing (with GPS/INS) using IOP_{II}

		x_p (mm)		y_p (mm)		c (mm)	
Block Adjustment	IOP before	-9.673e-02		-7.401e-02		11.6149	
	IOP after	-8.834e-02		-6.817e-02		11.6149	
	σ_o	3.57e-03 mm					
Check Point Analysis		X (m)		Y (m)		Z (m)	
	Mean ± std_dev	0.019±0.243		-0.028±0.652		-0.403±1.082	
	RMSE	0.241		0.645		1.144	
EOP Analysis		ω (″)	φ (″)	κ (″)	X_O (m)	Y_O (m)	Z_O (m)
	Mean	2	-1	-2	0.012	-0.016	0.021
	RMSE	6	9	5	0.060	0.036	0.051

Table 5.34: Reconstruction results for the 6 image block of the SonyF707 camera -

Direct geo-referencing (with GPS/INS) using IOP_{III}

		x_p (mm)		y_p (mm)		c (mm)	
Block Adjustment	IOP before	-1.047e-01		-6.983e-02		11.7028	
	IOP after	-8.995e-02		-6.542e-02		11.7028	
	σ_o	4.56e-03 mm					
Check Point Analysis		X (m)		Y (m)		Z (m)	
	Mean ± std_dev	0.012±0.301		0.005±0.430		5.952±1.038	
	RMSE	0.298		0.426		6.040	
EOP Analysis		ω (″)	φ (″)	κ (″)	X_O (m)	Y_O (m)	Z_O (m)
	Mean	2	-1	-1	0.012	-0.016	0.021
	RMSE	5	12	5	0.071	0.039	0.053

ii. 32 image block – Figure 5.6 shows the RMSE check point analysis results of the reconstruction while the complete analysis results are provided in Tables 5.35 to 5.43. Based on the graph in Figure 5.6, the trends seen in the 32 image block of the SonyF707 are similar to that of the 32 image block of the 9 x 9 inch Frame camera.

- For the indirect geo-referencing method, the RMSE of the check points are equivalent for all three IOP sets.

- For direct geo-referencing with GPS, the use of IOP_I and IOP_{II} yields relatively equal RMSE values (1.346 m and 1.571 m, respectively) while the use of IOP_{III} is higher (6.403 m).

- For direct geo-referencing with GPS/INS, the RMSE value for IOP_{II} is relatively equivalent (0.974 m) to the RMSE value for IOP_I (0.777 m), while the RMSE value for IOP_{III} is significantly higher (6.105 m). The reason why the RMSE value for IOP_{II} is relatively equivalent to the RMSE value for IOP_I is because the 32 image block has significantly better geometry with respect to the bundles in space. Hence, the principal point coordinate values (x_p, y_p) come very close to the true values after the least squares adjustment (See Table 5.42), which results in a better fit of the bundles and consequently, a low RMSE. However, in the case of IOP_{III}, the RMSE values remain high (6.105 m and 6.403 m) because the dissimilarity between IOP_{III} and IOP_I is caused due to the difference between their corresponding principal distances, which do not change in the bundle adjustment. The principal distance does not change because there is no ground truth, which is required to allow the principal distance to approach the true value in the bundle adjustment. Based on the EOP differences provided in Tables 5.35 to 5.43, the

EOP change in a manner that is similar to the effects described for the 6 image block (i.e. it reflects the constraints imposed by the geo-referencing technique).
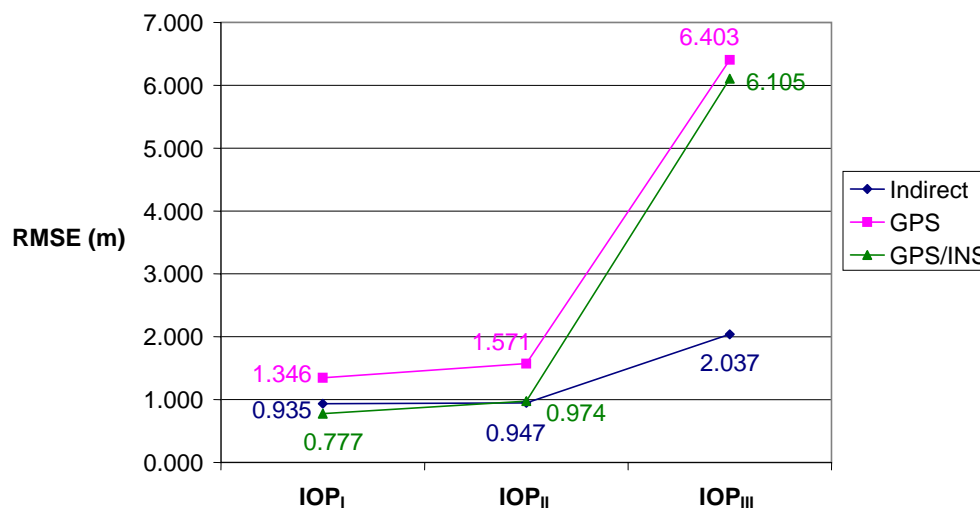
Figure 5.6: Quality of the reconstructed object space for the 32 image block of the SonyF707 camera

Table 5.35: Reconstruction results for the 32 image block of the SonyF707 camera - Indirect geo-referencing using IOP_I

		x_p (mm)	y_p (mm)	c (mm)		
Block Adjustment	IOP before	-8.542e-02	-6.057e-02	11.6224		
	IOP after	-8.561e-02	-6.058e-02	11.6224		
	σ_o	2.02e-03 mm				
Check Point Analysis		X (m)	Y (m)	Z (m)		
	Mean ± std_dev	0.064±0.169	-0.031±0.224	0.191±0.870		
	RMSE	0.180	0.226	0.889		
EOP Analysis		ω (″)	φ (″)	κ (″)	X_O (m)	Y_O (m)	Z_O (m)
	Mean	-39	-40	11	-0.134	0.187	0.126
	RMSE	165	202	53	0.995	0.878	0.273

Table 5.36: Reconstruction results for the 32 image block of the SonyF707 camera -

Indirect geo-referencing using IOP_{II}

		x_p (mm)		y_p (mm)		c (mm)	
Block Adjustment	IOP before	-9.673e-02		-7.401e-02		11.6149	
	IOP after	-9.628e-02		-7.384e-02		11.6149	
	σ_o	2.02e-03 mm					
Check Point Analysis		X (m)		Y (m)		Z (m)	
	Mean ± std_dev	0.068±0.172		-0.026±0.228		0.222±0.874	
	RMSE	0.185		0.230		0.900	
EOP Analysis		ω (″)	φ (″)	κ (″)	X_O (m)	Y_O (m)	Z_O (m)
	Mean	-38	-37	12	-0.112	0.182	0.818
	RMSE	221	232	54	1.059	0.874	0.854

Table 5.37: Reconstruction results for the 32 image block of the SonyF707 camera -

Indirect geo-referencing using IOP_{III}

		x_p (mm)		y_p (mm)		c (mm)	
Block Adjustment	IOP before	-1.047e-01		-6.983e-02		11.7028	
	IOP after	-1.041e-01		-6.975e-02		11.7027	
	σ_o	2.23e-03 mm					
Check Point Analysis		X (m)		Y (m)		Z (m)	
	Mean ± std_dev	0.073±0.225		-0.069±0.279		1.321±1.508	
	RMSE	0.236		0.287		2.003	
EOP Analysis		ω (″)	φ (″)	κ (″)	X_O (m)	Y_O (m)	Z_O (m)
	Mean	-16	-86	15	-0.350	0.035	-4.826
	RMSE	265	545	60	2.624	1.265	4.852

Table 5.38: Reconstruction results for the 32 image block of the SonyF707 camera -
Direct geo-referencing (with GPS) using IOP$_I$

		x_p (mm)		y_p (mm)		c (mm)	
Block Adjustment	IOP before	-8.542e-02		-6.057e-02		11.6224	
	IOP after	-8.516e-02		-6.057e-02		11.6224	
	σ_o	2.03e-03 mm					
Check Point Analysis		X (m)		Y (m)		Z (m)	
	Mean ± std_dev	0.344±0.383		-0.104±0.489		-0.049±1.141	
	RMSE	0.514		0.499		1.140	
EOP Analysis		ω (″)	φ (″)	κ (″)	X_O (m)	Y_O (m)	Z_O (m)
	Mean	-23	-68	-20	0.001	-0.013	0.000
	RMSE	78	94	126	0.032	0.049	0.039

Table 5.39: Reconstruction results for the 32 image block of the SonyF707 camera -
Direct geo-referencing (with GPS) using IOP$_{II}$

		x_p (mm)		y_p (mm)		c (mm)	
Block Adjustment	IOP before	-9.673e-02		-7.401e-02		11.6149	
	IOP after	-9.399e-02		-7.396e-02		11.6149	
	σ_o	2.07e-03 mm					
Check Point Analysis		X (m)		Y (m)		Z (m)	
	Mean ± std_dev	0.338±0.382		-0.108±0.518		-0.733±1.182	
	RMSE	0.510		0.529		1.389	
EOP Analysis		ω (″)	φ (″)	κ (″)	X_O (m)	Y_O (m)	Z_O (m)
	Mean	-25	-67	31	0.001	-0.013	0.000
	RMSE	275	163	134	0.032	0.049	0.040

Table 5.40: Reconstruction results for the 32 image block of the SonyF707 camera -

Direct geo-referencing (with GPS) using IOP$_{III}$

		x_p (mm)		y_p (mm)		c (mm)	
Block Adjustment	IOP before	-1.047e-01		-6.983e-02		11.7028	
	IOP after	-1.006e-01		-6.967e-02		11.7028	
	σ_o	2.38e-03 mm					
Check Point Analysis		X (m)		Y (m)		Z (m)	
	Mean ± std_dev	0.346±0.515		-0.229±0.618		6.157±1.512	
	RMSE	0.619		0.659		6.339	
EOP Analysis		ω (″)	φ (″)	κ (″)	X_O (m)	Y_O (m)	Z_O (m)
	Mean	-51	-70	77	0.001	-0.013	0.000
	RMSE	202	253	176	0.033	0.049	0.041

Table 5.41: Reconstruction results for the 32 image block of the SonyF707 camera -

Direct geo-referencing (with GPS/INS) using IOP$_I$

		x_p (mm)		y_p (mm)		c (mm)	
Block Adjustment	IOP before	-8.542e-02		-6.057e-02		11.6224	
	IOP after	-8.559e-02		-6.029e-02		11.6224	
	σ_o	2.04e-03 mm					
Check Point Analysis		X (m)		Y (m)		Z (m)	
	Mean ± std_dev	0.004±0.120		-0.025±0.181		0.070±0.744	
	RMSE	0.120		0.182		0.746	
EOP Analysis		ω (″)	φ (″)	κ (″)	X_O (m)	Y_O (m)	Z_O (m)
	Mean	-1	0	-2	0.001	-0.013	0.000
	RMSE	5	6	7	0.027	0.038	0.040

Table 5.42: Reconstruction results for the 32 image block of the SonyF707 camera -

Direct geo-referencing (with GPS/INS) using IOP_{II}

		x_p (mm)		y_p (mm)		c (mm)	
Block Adjustment	IOP before	-9.673e-02		-7.401e-02		11.6149	
	IOP after	-8.591e-02		-6.155e-02		11.6149	
	σ_o	2.39e-03 mm					
Check Point Analysis		X (m)		Y (m)		Z (m)	
	Mean ± std_dev	0.002±0.122		-0.024±0.192		-0.593±0.739	
	RMSE	0.122		0.194		0.947	
EOP Analysis		ω (″)	φ (″)	κ (″)	X_O (m)	Y_O (m)	Z_O (m)
	Mean	-1	0	-1	0.001	-0.013	0.000
	RMSE	5	6	7	0.028	0.039	0.040

Table 5.43: Reconstruction results for the 32 image block of the SonyF707 camera -

Direct geo-referencing (with GPS/INS) using IOP_{III}

		x_p (mm)		y_p (mm)		c (mm)	
Block Adjustment	IOP before	-1.047e-01		-6.983e-02		11.7028	
	IOP after	-8.627e-02		-6.108e-02		11.7028	
	σ_o	2.76e-03 mm					
Check Point Analysis		X (m)		Y (m)		Z (m)	
	Mean ± std_dev	0.003±0.126		-0.023±0.197		6.005±1.082	
	RMSE	0.125		0.198		6.101	
EOP Analysis		ω (″)	φ (″)	κ (″)	X_O (m)	Y_O (m)	Z_O (m)
	Mean	-1	0	-1	0.001	-0.013	0.000
	RMSE	5	7	7	0.030	0.039	0.041

The trends observed from the portrait configurations of the image block of the Sony F707

camera were consistent with those observed by the landscape configurations. Based on

these results, the expectation that one stability analysis method will be better suited over another depending on the implemented geo-referencing technique was verified. It also showed that the behaviour of the small format (Sony F707) and the large format (9 x 9 inch Frame) camera were the same. Furthermore, the results confirmed that the relative quality of the object space reconstructed from two sets of IOP will be equivalent if the IOP sets are deemed similar based on the condition that the constraints imposed by the similarity method are analogous with the constraints imposed by the geo-referencing technique implemented in the reconstruction.

CHAPTER 6

APPLICATIONS

6.1 Introduction

Low-cost digital cameras can be implemented in a number of diverse applications with respect to the generation of three-dimensional information. The process of calibration and stability analysis of such cameras must be done prior to the reconstruction of the object space of the involved application. The accuracy of the reconstruction is dependent on the accuracy and reliability of the IOP of the implemented camera. Thus, it is imperative that the camera is well-calibrated and analyzed for the stability of its IOP. Based on the experimental results in Chapter 4, it was found that all the tested digital cameras with the exception of the Nikon cameras maintained the stability of their IOP over a significant period of time. The applications investigated in this research include the measurement of facial features for personal identification, the generation of 3-D CAD models of buildings for archiving, and the reconstruction of a human torso for modeling spinal disorders. The procedures involved in these potential applications will be discussed in the following sections.

6.2 Facial Measurements

The core objective of making measurements of facial features on a human face is to identify the person by the geometry of the face. The generation of 2-D or 3-D models from measurements of the human face have wide-ranging applications that include video surveillance, lip reading systems, video teleconferencing, computer animation, virtual reality, and medical treatments (D'Apuzzo, 2002). For example, biometrics, which is the biological identification of a person, is increasingly being used as a more secure form of authentication than typing passwords, using finger prints, or using smart cards (3DBiometrics Inc., 2005). The most important considerations to take into account are the complexity and cost of the equipment, the accuracy of the measurements, and the time it takes to obtain the final product. The use of digital cameras for photogrammetric measurements offers an accurate, reliable, and cost-effective approach to derive 3-D coordinates of points on a face.

One of the key issues is the calibration of the implemented camera, which must be done prior to the derivation of 3-D coordinates. For the experiments conducted in this research, a Sony F707 camera was used. Since this a close-range application, a calibration test field for a 1.0 meter object distance was created. Three calibrations were carried out to obtain three different sets of IOP. Then each set is tested against another for similarity, Table 6.1. Based on the results in Table 6.1, it can be seen that all sets proved to be similar to one another and hence, any set can be utilized in the experiments. However, the comparison between Set 2 and Set 3 yielded a standard deviation of only 0.12 μm, which

is well below the 3.00 μm similarity threshold. For this reason, either Set 2 or Set 3 can be used in the experiments for the determination of facial feature coordinates.

Table 6.1: Similarity tests between three calibration sets of the SonyF707 camera

(<u>Note</u>: If $\sigma_o < 3.00$ μm, IOP sets considered similar)

1st IOP Set	2nd IOP Set	σ_o (μm)
Set1	Set2	2.57
Set1	Set3	2.49
Set2	Set3	0.12

Once the calibration and similarity comparison have been carried out, the task can proceed by capturing images, a left and a right image, of the person (subject). Both images should be taken at the same time to prevent any possible movement of the subject during the image capture. However, due to constraints on resources in this research, this was not done. The left and right images were captured one at a time in quick succession.

Another vital issue is to determine what features on the face should be measured such as areas, volumes or distances from different points on the face. Using the acquired images, the outside corners of each subject's eyes and the top central position of the subject's lip are measured to establish a triangle on the face as shown in Figure 6.1. The area of this triangle can be computed as a basis for identification. In these experiments, there were four stereo pairs captured for each of the four subjects, Figure 6.1. These four image sets of each subject were measured by four different operators to prove that the measurements were repeatable and consistent.

Subject 1 — Left Image, Right Image

Subject 2 — Left Image, Right Image
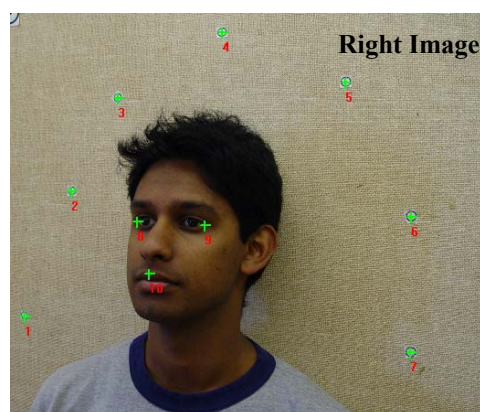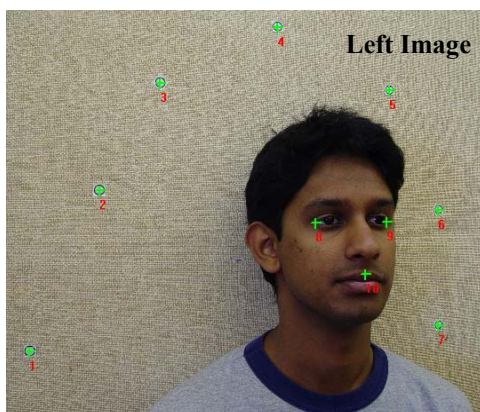
Subject 3 — Left Image, Right Image
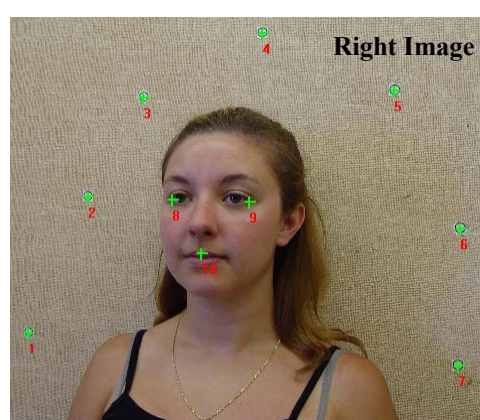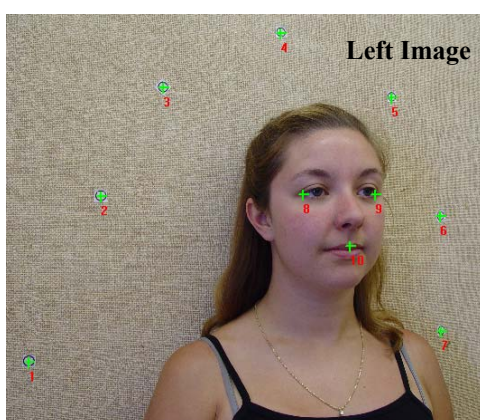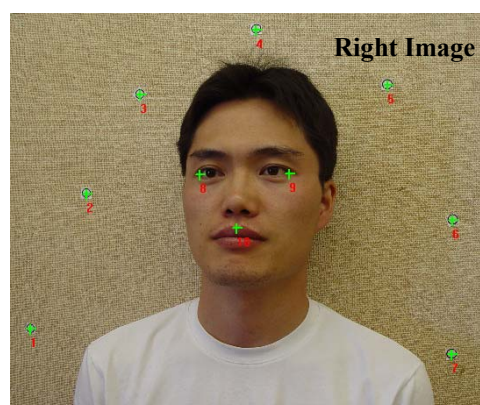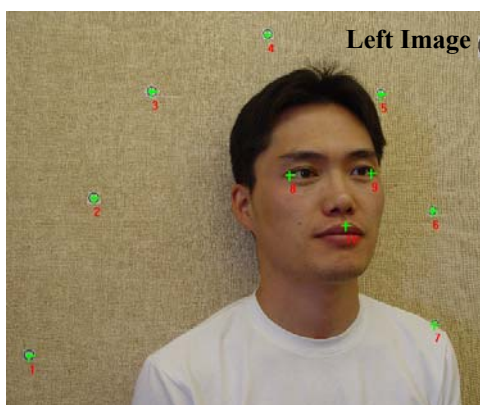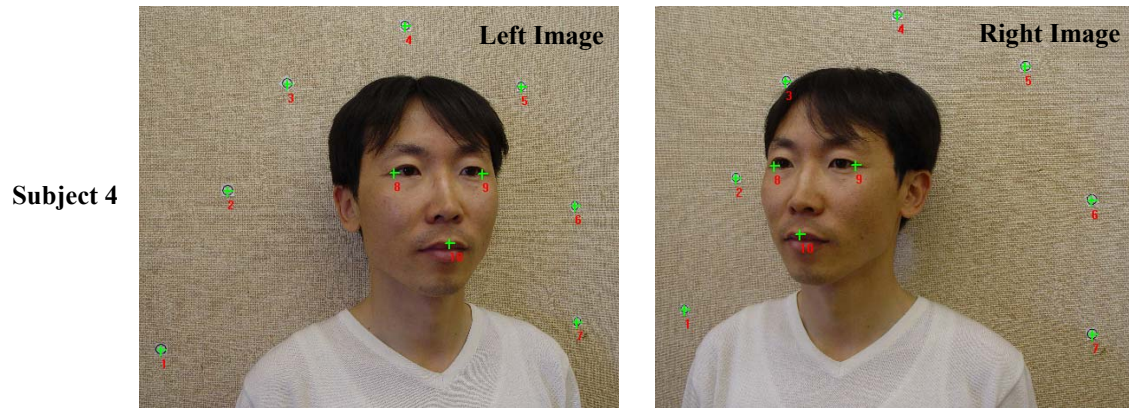
Figure 6.1: Left and right images of the four subjects showing the configuration of the

facial measurements

After making the measurements of the three facial points together with other tie points in

the image, the three-dimensional coordinates of the points are recovered from a bundle

adjustment procedure. Using the computed coordinates, the area occupied by joining

these points is then calculated, Equation 6.1.

$$Area = \frac{1}{2}\sqrt{\begin{vmatrix} y_1 & z_1 & 1 \\ y_2 & z_2 & 1 \\ y_3 & z_3 & 1 \end{vmatrix}^2 + \begin{vmatrix} z_1 & x_1 & 1 \\ z_2 & x_2 & 1 \\ z_3 & x_3 & 1 \end{vmatrix}^2 + \begin{vmatrix} x_1 & y_1 & 1 \\ x_2 & y_2 & 1 \\ x_3 & y_3 & 1 \end{vmatrix}^2}$$

(6.1)

Where (x_1, y_1, z_1), (x_2, y_2, z_2) and (x_3, y_3, z_3) are the 3-D coordinates of the three vertices

of the triangle needed to calculate the area of the face.

As mentioned earlier, each operator processed the datasets for all four subjects (i.e. 4

operators x 4 subjects x 4 datasets). For each of the four datasets of each subject, a facial

area was computed as well as the average and standard deviation of the four area values

derived by one operator. The standard deviation represents the dispersion around the

average facial area of one subject that is determined by one operator. The results of these computations can be seen in Table 6.2. When looking at the four areas computed for each subject by one operator, it is evident that all values are fairly close to each other. The standard deviations show that it is possible to determine a facial area with any dataset (i.e. a dataset acquired at any time). Therefore, once a facial area has been determined and recorded from one dataset, a match can be made to an area computed from a later dataset capture to identify the person with relatively good accuracy. However, in the four datasets for Subject 4, Operator 2 was not consistent in measuring the points since the standard deviation of the four areas was 0.92 cm^2. It can be seen that the other operators also found it difficult to identify features for Subject 4 based on the relatively high standard deviations of 0.39 cm^2, 0.45 cm^2, and 0.47 cm^2. This signifies that it is not apparent where the triangle point locations should be for subjects whose facial features do not have sharp or well-defined corners, which was the case for Subject 4.

Comparing the average area value for each subject, it can be seen that there is a relatively small difference between each operator's averages except for Subject 3. There is a wide range in the average values computed by each operator for Subject 3, which is (34.71 − 33.55 = 1.16 cm^2). The standard deviations of Subject 3 for all operators are relatively low, which indicates that the operators consistently picked the three triangle point locations consistently in each of their four datasets. Therefore, the large difference in their average areas signifies that the points one operator picked for the triangle point locations were not the same as the points that the other operator picked.

Table 6.2: Computed facial areas with each subject's average area and standard deviations

| Operator | Subject | Area (cm^2) | | | | | |
		Dataset 1	Dataset 2	Dataset 3	Dataset 4	Avg.	Std. Dev.
Operator 1	Subject 1	29.28	29.50	28.87	29.25	**29.22**	**0.26**
	Subject 2	26.98	26.78	26.88	26.55	**26.80**	**0.18**
	Subject 3	34.57	34.93	34.28	35.06	**34.71**	**0.35**
	Subject 4	38.09	37.52	37.16	37.75	**37.63**	**0.39**
Operator 2	Subject 1	29.93	29.00	28.85	29.63	**29.35**	**0.51**
	Subject 2	27.33	27.25	27.42	27.14	**27.28**	**0.12**
	Subject 3	33.67	33.31	33.34	33.88	**33.55**	**0.27**
	Subject 4	38.07	37.48	36.01	37.82	**37.35**	**0.92**
Operator 3	Subject 1	29.57	29.17	29.29	29.40	**29.36**	**0.17**
	Subject 2	27.18	27.43	27.54	27.09	**27.31**	**0.21**
	Subject 3	34.45	34.43	34.50	34.30	**34.42**	**0.09**
	Subject 4	38.04	37.67	37.13	38.09	**37.73**	**0.45**
Operator 4	Subject 1	29.67	30.24	29.68	29.92	**29.87**	**0.27**
	Subject 2	26.74	27.09	26.89	26.91	**26.91**	**0.15**
	Subject 3	34.10	33.82	33.62	33.89	**33.86**	**0.19**
	Subject 4	37.65	37.14	36.53	37.35	**37.17**	**0.47**

The results in Table 6.2 are graphically represented in Figure 6.2. It shows the computed facial areas of each subject from measurements made by the four operators. It can be seen that the area values of each subject are relatively close to one another and does not overlap with values of another subject. This is important since it signifies that a person can be uniquely identified based on an area of the face. However, two or more people can have the same facial area, which would not provide a unique solution. Hence, to make

this application more comprehensive, incorporating a combination of distances, areas and volumes to identify the person could be explored.
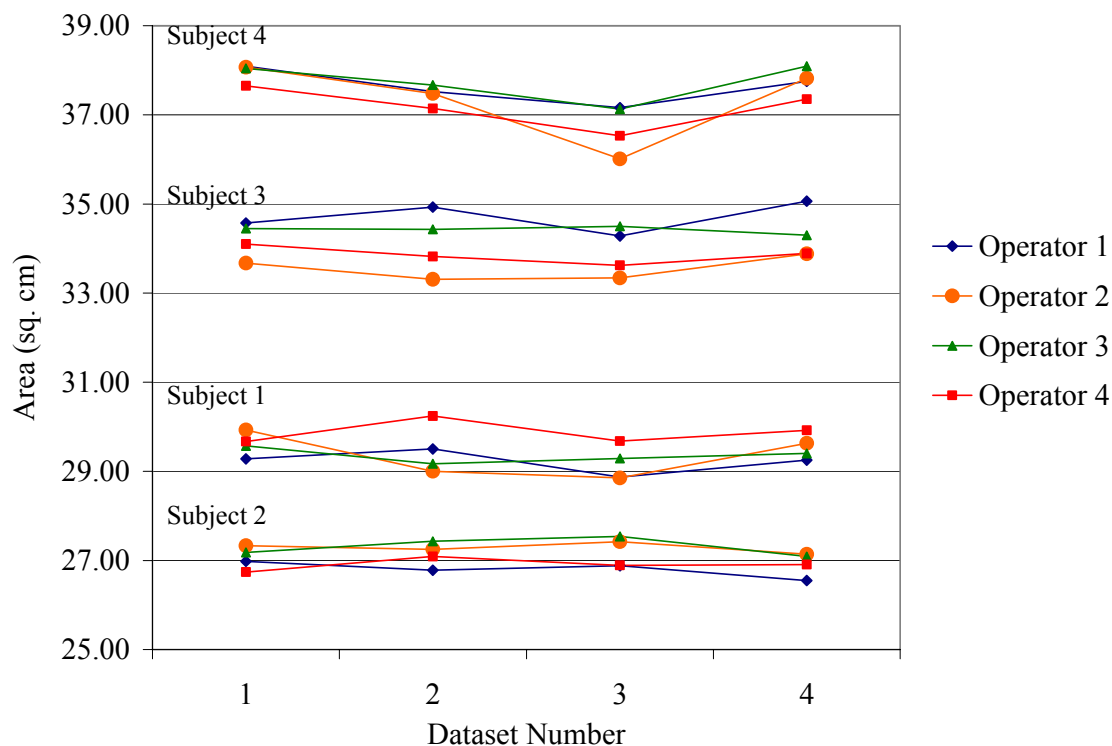
Figure 6.2: Computed facial areas of all four subjects from measurements made by four operators

Another source of further enhancement could involve the automation of facial feature measurements. Currently, points on the face and in the surrounding area are manually measured by an operator. An automated process could be incorporated by developing some kind of image matching algorithm that can easily identify points on the face and measure them. This could help establish corresponding points in the two images in a fast, accurate, and reliable manner. In addition, a projected grid on the face could offer an

easier way to make the measurements, Figure 6.3. The vertices of the grid can be measured since they will reflect the same point in both images.
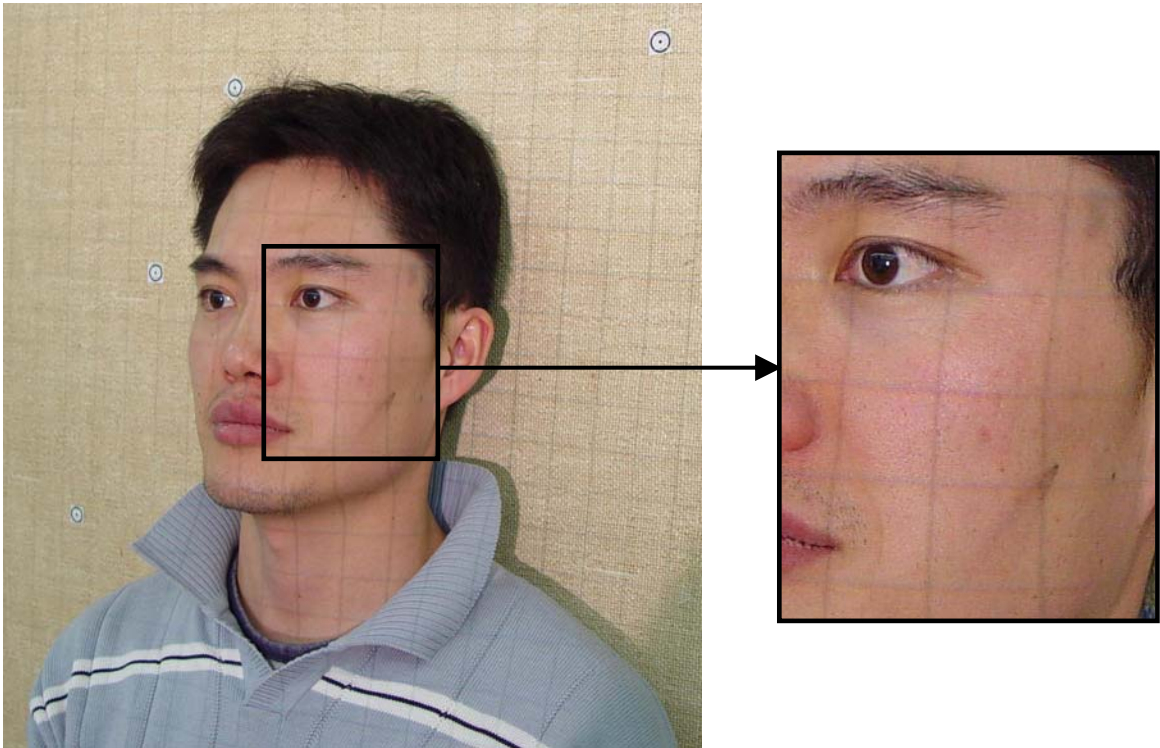
Figure 6.3: A projected grid on the face for easier measurement of facial features

6.3 3-D CAD Model Generation

Utilizing imagery to generate three-dimensional CAD models is useful in a wide variety of applications such as architecture, archaeology, building inspections, and archiving of historical sites (Habib et al., 2004). This research investigates the use of a low-cost digital camera to create a three-dimensional model of a building. Figure 6.4 shows two real images of the building that was used in this experiment. As described in section 6.2, calibration and similarity tests of the implemented camera must be conducted to ensure

the accurate reconstruction of the object. In the calibration process, the object distance should reflect the distance from the point of exposure to the building.

Figure 6.4: Two real images captured of the building

A Sony F707 camera was employed in this experiment to capture sixty convergent and overlapping images around the building, Figure 6.5. This is followed by making measurements of carefully selected points on the building in the acquired imagery. It is crucial that an adequate number of points are selected for the reconstruction of the building. These point measurements are then introduced into the bundle adjustment process in order to estimate their ground coordinates. In the adjustment, an arbitrary datum is chosen as reference for the object space and the scale is established by incorporating a few measured distances. The accuracy of the derived point coordinates from the adjustment is tested by computing the distance between them and comparing these distances with the ones measured in the field, Table 6.3. These measured (check) distances were not used in the bundle adjustment procedure. As can be seen in Table 6.3, there is approximately a 1-4 mm difference between the computed and measured distances.
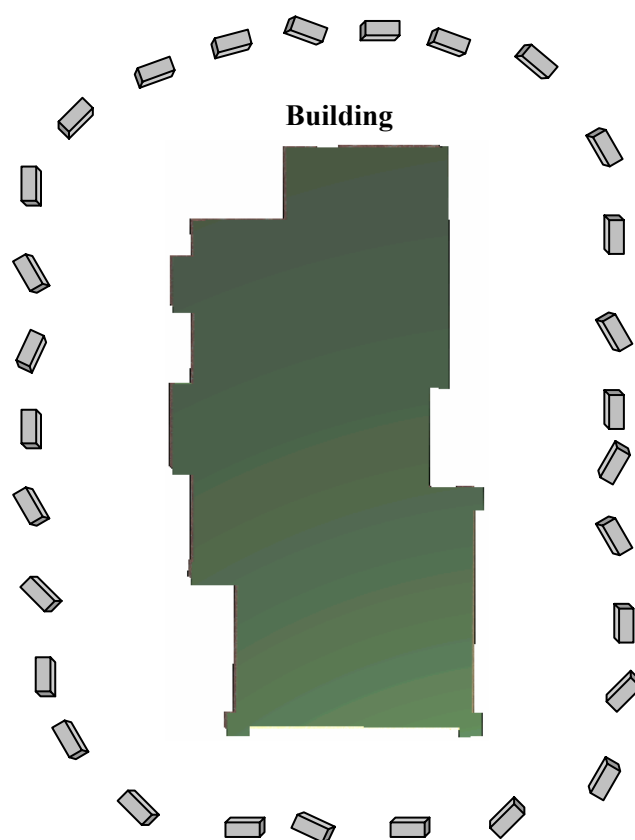
Building

Figure 6.5: Location of convergent and overlapping images surrounding the building

Table 6.3: Comparison between measured / field distances and computed / photogrammetric distances

Point 1	Point 2	Measured Distance (m)	Computed Distance (m)	Difference (mm)
H001	H004	18.08	18.0825	2.5
G018	G008	7.85	7.85186	1.9
G008	G009	11.84	11.8418	1.8
G015	G012	12.21	12.2106	0.6
G015	G002	12.495	12.4924	2.6
G017	G007	4.67	4.6659	4.1

Once coordinates of the points are computed, they are then imported into a CAD modelling program like AutoCAD. The points have to be joined to create a wire-frame model of the building, Figure 6.6 (a). However, this wire-frame model is simply a network of vertices and edges. There is no surface to which colors and textures can be applied. Real-world textures can only be applied to solid objects. Hence, a solid model of rectangular boxes has to be created using the wire-frame model, Figure 6.6 (b).
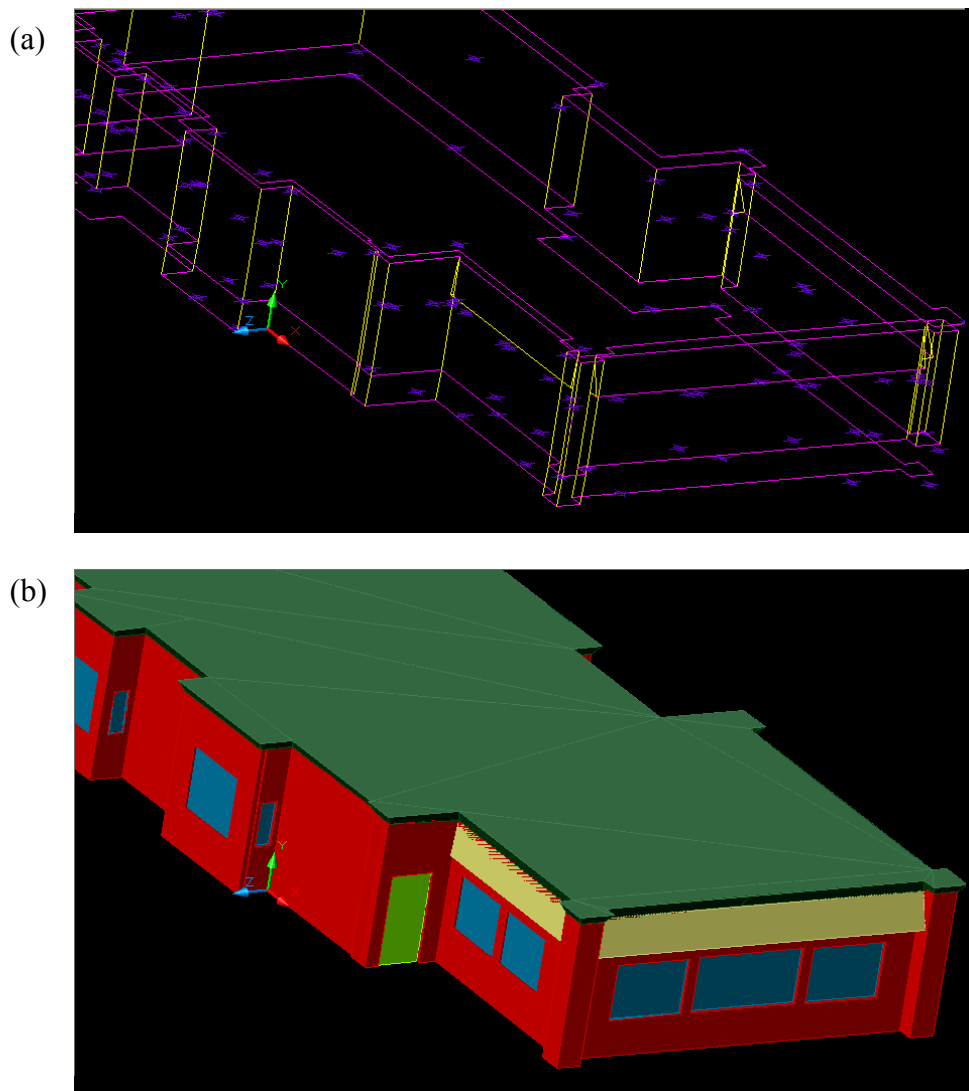
Figure 6.6: (a) A wire-frame model and (b) a solid model of the building in AutoCAD

As shown in Figure 6.6 (b), the solid model can only have basic colors. However, a rendered surface with real-world surface texture can be generated from this solid model. The built-in capability of AutoCAD allows texture material and lighting to be added to each individual solid object. Once material is added to all objects, the solid model shown in Figure 6.6 (b) can be converted into a rendered surface as shown in Figure 6.7. This modelling method provided in AutoCAD is reliable and has varying degrees of flexibility with respect to the level of detail.

Figure 6.7: The final reconstructed 3-D CAD model of the building with real-world
surface textures

6.4 Medical Imaging

Photogrammetric techniques are commonly and increasingly being used in the modeling and reconstruction of body parts like spines, rib cages, and bones. The objective is to implement non-invasive measurements to assess medical conditions like scoliosis, which is a disorder that is characterized by a deformity in the spine, Figure 6.8 (Robu et al, 2004). A 3-D reconstruction of an artificial scoliotic human torso is used to help in the diagnosis, analysis, and treatment (design of custom braces) of scoliosis. In the work of

(Robu et al., 2004), a Coordinate Measuring Machine (CMM) is utilized to measure markers on the torso to derive 3-D positions of these targets. A CMM is a high-end measuring system designed to move a measuring probe to determine coordinates of points on an object with very high precision and accuracy. The goal of this investigation is to check the potential use of photogrammetric measurements, which is a more convenient, faster, and cost-effective approach than using a CMM. Furthermore, it provides non-contact 3-D measurements that can achieve accuracies that come close to those taken by a CMM.
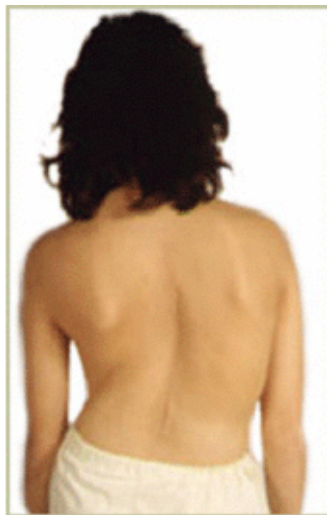
Figure 6.8: A person with a spinal deformity called scoliosis (Robu et al, 2004)

In the experiments conducted in this research, photogrammetric methods are used to measure and determine coordinates of the targets on the artificial torso and compare these derived coordinates to those determined by the CMM. There were two cameras utilized in the experiments, a Sony F707 and a Rollei. One set of images were captured using the Sony F707 and two sets of images were captured using the Rollei. For each image set,

approximately sixteen overlapping images are captured at locations surrounding the torso, Figure 6.9.
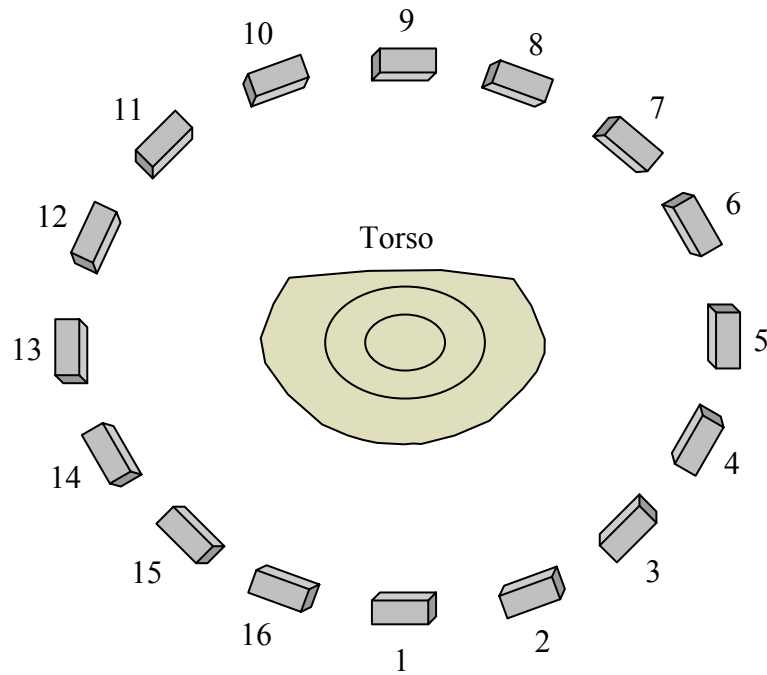
Figure 6.9: Location of sixteen overlapping images surrounding the torso (top view)

To establish the datum in the bundle adjustment procedure for reconstruction, some nearby points in the area that are not on the torso are arbitrarily fixed. The scale in the datum is established by incorporating a few measured distances on or around the torso. The fixed points, the target points on the torso, and other tie points in the surrounding area are then measured in the imagery, Figure 6.10. It is important that there are a suitable number of tie points measured in the surrounding area to tie the images together.
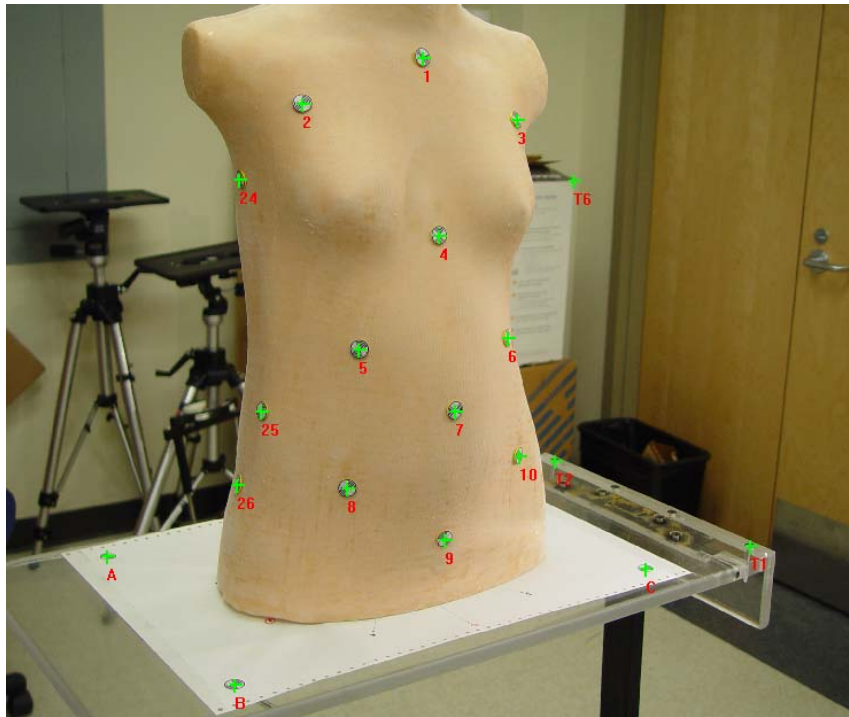
Figure 6.10: Measurement of targets on an artificial human torso and tie points in the surrounding area

After the measurements are carried out, the coordinates of the targets can be derived in a reconstruction procedure. The accuracy of the measurements is represented by the variance component (σ_o) obtained in the adjustment. In these experiments, two operators measure the targets to confirm the repeatability and consistency of the measurements. The derived photogrammetric coordinates are then converted into the CMM coordinate system using a 3-D similarity transformation. This transformation is performed so that the two measurement techniques can be compared by computing the root mean square error (RMSE) of the differences between the photogrammetric and CMM coordinates. The derived photogrammetric coordinates are also used to compute distances between them and these distances are compared to those derived from the CMM coordinate

measurements. These coordinate and distance differences as well as the measurement accuracies are presented in Table 6.4. The results show that there is approximately a 1.0 mm difference between corresponding coordinates and distances of the photogrammetry and CMM measurements. It is known that the CMM attains accuracies that are on the micron level (0.5 – 1.0 μm), whereas the results in Table 6.4 signify that photogrammetric measurements attains accuracies that are on the mm level. However, it is important to note that photogrammetric techniques are cheaper, more convenient, and offers the potential of being faster if measurements can be automated.

Table 6.4: Torso measurement accuracy and RMSE difference comparison between photogrammetry and CMM measurements

Dataset	Operator	σ_0 (mm)	RMSE Difference (mm)	
			Coordinates	Distances
SonyF707 – Set 1	Operator 1	2.55e-003	0.926	0.943
	Operator 2	2.51e-003	0.956	1.017
Rollei – Set 1	Operator 1	2.65e-003	1.132	1.002
	Operator 2	2.58e-003	1.120	0.915
Rollei – Set 2	Operator 1	3.28e-003	1.170	1.134
	Operator 2	4.84e-003	1.203	1.125

Similar to the generation of a 3-D CAD model of a building as discussed in section 6.3, a 3-D model of the torso can also be generated using the derived target coordinates. As shown in Figure 6.11 (a), a 3-D surface model can be created using a mesh. A mesh is a type of grid that essentially consists of a series of grouped polygons to represent the surface. It will give the surface a more curved appearance while still being made to pass through the derived target points. Another benefit of using a mesh is that real-world

surface textures can be added to it similar to solid objects. Figure 6.11 (b) shows the final

rendered surface model of the torso after adding the textures.
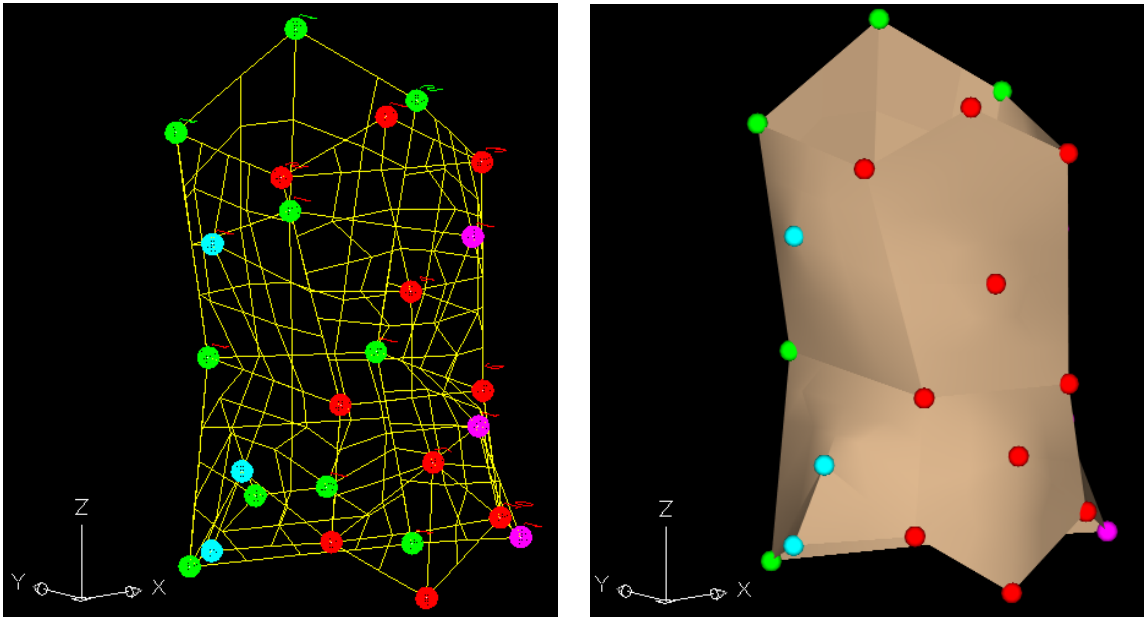
Figure 6.11: (a) A 3-D mesh model and (b) a rendered model of the torso in AutoCAD

As discussed in section 6.2, measurements made in the image are manually done. An

automated process involving image matching could make for an easier and quicker way

to make the measurements. This could also be further enhanced by projecting a grid on

the image to locate points more easily.

CHAPTER 7

CONCLUSION AND FUTURE WORK

7.1 Conclusion

The presented research outlined an efficient approach for calibration, and four meaningful measures for evaluating the stability of off-the-shelf digital cameras. A description of an easy-to-establish calibration test field and the utilized digital cameras was illustrated. Furthermore, the short-term and long-term stability of these cameras under various operational and procedural settings were demonstrated.

In this research, calibration was done using straight line linear features and signalized points (Habib et al., 2002-a). Deviations from straightness in image space straight lines were attributed to various distortion parameters. The automatic extraction and measurement of lines were done using image processing techniques. In the calibration procedure, various conditions could be altered, and the IOP estimates of the tested digital cameras were not dependent on the manipulation of these conditions.

The presented research outlined four new methodologies for evaluating the stability of both analog and digital cameras. These methodologies are based on evaluating the degree

of similarity between reconstructed bundles defined by two sets of IOP, which are derived from two calibration sessions. Each method imposes constraints regarding the relative position and attitude of the compared bundles in space. In the MIS method, the principal distance from the two IOP sets are considered equal, and its similarity measure is simply given by the RMSE of the offset values between distortion-free coordinates that are derived from the principal point coordinates. In the ZROT method, the principal distance is incorporated to help reconstruct two bundles that have parallel image coordinate systems and share the same perspective center. Since the two bundles are fixed in the same position and orientation, it provides a very strict measure of similarity. Like the MIS method, the ZROT method's similarity measure is also given by the RMSE of the spatial offset. In the ROT method, the two bundles are allowed to rotate relative to each other until the best coincidence is achieved and therefore, is not as conservative as the ZROT method. In the SPR method, both spatial and rotational offsets are allowed between the two bundles while observing their quality of fit at a specified type of object space. Hence, this method provides the most relaxed measure of similarity when a terrain with low height variation with respect to the flying height is assumed. Since a terrain with low height variation leads to a high correlation between the IOP and EOP, the EOP changes to absorb the differences between the two IOP sets to produce a good fit at the object space. On the other hand, a terrain with high height variation reduces any possible correlation between the IOP and EOP, and thus the EOP does not change to compensate for the differences in IOP. For the ROT and SPR methods, the similarity measure is characterized by the standard deviation of the spatial offset (σ_o) between the two bundles along the image plane. For all four measures of similarity, if the RMSE or σ_o lies within

the range defined by the expected image coordinate measurement accuracy (one-half to two-thirds of the pixel size of the implemented camera), the two IOP sets are considered similar.

It should be noted that the four stability measures are general enough that they can be applied to digital as well as analog cameras intended for mapping applications. These measures would allow amateur users of digital cameras to evaluate their stability. In addition, the developed measures do not require additional field work to evaluate camera stability and the statistical properties of the available IOP sets are not needed.

Each of these four methods of stability analysis limits the position and orientation of the compared bundles in a different way. Hence, it was verified that each method will be applicable for a specific geo-referencing technique. The ZROT method would be ideal for direct geo-referencing with GPS and INS data since the position and attitude of the bundles are fixed. The ROT method allows rotation between the bundles, which would make it ideal when only GPS data is used in the bundle adjustment. Finally, the SPR method would make it ideal for indirect geo-referencing since spatial and rotational offsets are permitted, and hence the position and attitude of the bundles can be estimated in the adjustment. Based on these relationships, if two IOP sets are similar according to a certain similarity method, the relative quality of the object space that is reconstructed based on the corresponding geo-referencing technique using either IOP set will also be similar. A simulated (large format) frame camera and a Sony F707 (small/medium format) camera were used to test this hypothesis. Both cameras showed the same behaviour and confirmed the hypothesis with respect to one stability analysis method

being better suited over another for a certain geo-referencing technique based on similar constraints.

There were ten amateur and professional digital cameras tested for the stability of their IOP. Each type of camera had different characteristics and resolutions. The analysis of these cameras revealed that the IOP remained stable over the thirteen-month period. The only exception was the stability of the Nikon cameras, which showed poor long-term as well as short-term stability. The reason for this is not known, although it is possible that there may be an issue with the lens design. For one of the failed Nikon cameras, the stability was tested using the ZROT, ROT and SPR (with two object space configurations) similarity measures. It was found that the ZROT and ROT methods yielded similarity measures that were closer to that obtained from the SPR method when a terrain with a high height variation relative to the flying height was assumed. The most relaxed similarity measure was obtained when a terrain with low height variation relative to the flying height was assumed since the EOP changed to absorb the differences in IOP.

In addition to analyzing stability, IOP sets were compared to other sets that were obtained in the same calibration session, but had different calibration conditions/settings. These conditions included changing certain settings on the camera, changing the size of the test field, and altering the number of estimated parameters in the calibration procedure. Based on the experimental results, it was found that changing the focusing method of the Sony F707 and removing the lens and filter of the Canon camera did not affect their short-term stability. The experiments also revealed that the IOP estimates are not dependent on the test field size; rather, they are dependent on the percentage of the image occupied by the

test field. In addition, the comparison of IOP from calibration datasets where a different number of distortion parameters was estimated indicated that K_1 adequately describes the distortion parameters associated with most of the tested cameras. The only exceptions were the Rollei and Sony P9 cameras. The test field did not occupy a sufficient percentage of the image for the Rollei camera and the Sony P9 could have had a significant de-centric lens distortion component, which is why K_1 did not adequately describe all the distortion parameters associated with these two cameras. It is important to note that estimating only K_1 will be true only for cameras with a narrow angular field of view.

Applications involving the measurement of facial features, the three-dimensional reconstruction of a building for archiving, and the modelling of a torso for medical treatments demonstrated the usefulness of the presented calibration techniques and similarity measures. The computation of areas on the face based on many captured datasets, subjects, and four different operators measuring them proved that the measurements were repeatable and consistent. Furthermore, it showed that the computed areas were distinctive, which is important when attempting to uniquely identify a person. The reconstruction and the generation of a 3-D CAD model of a building showed that the procedure was straightforward and accurate. The accuracy of the reconstruction procedure was tested by computing the distance between derived point coordinates from the photogrammetric adjustment and comparing these distances with the ones measured in the field. It was found that there was approximately a 1-4 mm difference between the computed and measured distances. The reconstruction and modelling of the artificial

scoliotic human torso also achieved very good accuracies. In the conducted experiments, photogrammetric methods were used to measure and determine coordinates of targets on the artificial torso and compare these derived coordinates to those determined by a CMM, which is a highly accurate and expensive measuring system. The experimental results proved that photogrammetric measurements is not as accurate as measurements taken by a CMM, but comes very close. However, the use of photogrammetric measurements offers a non-contact means of deriving 3-D coordinates that is more convenient, faster and cost-effective.

7.1.1 Precautions for Calibration and Stability Analysis Procedures

Based on the experimentation conducted for the calibration and stability analysis tests, there are a few occurrences to watch for or precautions to take:

- Determine the number, position and orientation of images to be taken of the test field, and make sure they are taken in a pre-determined order.

- If the test field is two-dimensional, take convergent imagery by tilting the camera slightly to get angled images, which strengthens geometry and reduces correlation between unknown parameters.

- When taking the images, make sure that a good percentage (80-100%) of the image is occupied by the test field.

- Make sure there is an ample amount of light shining from different directions on the test field. If the light is not adequate, shadows will be created in the images, which will hinder the automatic extraction of the lines.

- Observe the imagery for blurriness. If there is such an image, delete and re-take another one. If blurry images are used, lines and points will be difficult to identify and they may be measured inaccurately.

- The points and lines must be identified with care. Common errors that occurred during experimentation were the incorrect labelling of points and the inaccurate specification of the end points of lines.

- For certain cameras like the Canon, be careful when taking off and putting on components. If it is not done properly, it could affect the internal characteristics of the camera.

- If an improper configuration is used for calibration, high residual values might be generated in the bundle adjustment. To find the source of the problem, analyze correlations among unknowns in the adjustment procedure. Remove all correlated parameters except one and re-run the calibration to determine the error source.

7.2 Recommendations for Future Research

The proposed measures of similarity are effective in comparing two IOP sets derived from two calibration sessions. However, a possible future initiative could be directed towards finding a way to compare more than two sets of IOP at one time. Since the

current methods only allow two IOP sets to be compared, this is not efficient when datasets from many calibration sessions are available.

With regard to the applications of the low-cost cameras, the current process of making measurements is manually done by an operator, which proves to be quite tedious. An enhancement that could make measurements easier is the projection of a grid on the object of interest. In the case of facial feature or torso measurements, a projected grid could offer an easier way to accurately measure a certain point. The automation of the measurements is also potentially useful research that is worth investigating. This automation process could involve a type of image matching algorithm that can easily identify points on the object and accurately measure them.

REFERENCES

3DBiometrics - The Technology Web Page. http://www.3dbiometrics.com/. Accessed on: February 20, 2005.

Ayache N., and O. Faugeras, 1989. Maintaining representations of the environment of a mobile robot, *IEEE Transactions on Robotics Automation*, 5 (6), 804-819.

Bräuer-Burchardt C., and K. Voss, 2001. A new algorithm to correct fish-eye and strong wide-angle-lens-distortion from single images, *Proceedings of the 2001 International Conference on Image Processing*, October 7-10, 2001, Thessaloniki, Greece, Volume 1, pp. 225-228.

Brown D., 1966. Decentric distortion of lenses, *Journal of Photogrammetric Engineering & Remote Sensing*, 32 (3): 444-462.

Brown D., 1971. Close range camera calibration, *Journal of Photogrammetric Engineering & Remote Sensing*, 37 (8): 855-866.

Canny J., 1986. A computational approach to edge detection, *IEEE Transactions on Pattern Analysis and Machine Intelligence*, 8 (6): 679-698.

Chen S., and W. Tsai, 1991. A systematic approach to analytic determination of camera parameters by line features, *Pattern Recognition*, 23(8): 859-877.

D'Apuzzo N., 2002. Modeling Human Faces with Multi-Image Photogrammetry, *Three-Dimensional Image Capture and Applications V Proceedings of SPIE*, San Jose, California, Vol. 4661.

Faugeras O., M. Hebert, 1986. The Representation, Recording, and Locating of 3-D Objects, *The International Journal of Robotics Research*, Vol. 5, No. 3, pp. 27-52.

Fraser C., 1997. Digital camera self-calibration, *ISPRS Journal of Photogrammetry and Remote Sensing*, 52(4): 149-159.

Fryer J., 1996. Camera calibration, *Close range Photogrammetry and machine vision*, (K.B. Atkinson, editor), Whittles Publishing, Caithness, Scotland, pp. 156-180.

Guoqing Z., U. Ethrog, F. Wenhao, and Y. Baozong, 1998. CCD camera calibration based on natural landmarks, *Pattern Recognition*, 31(11): 1715-1724.

Habib A., 1998. Motion parameter estimation by tracking stationary three-dimensional straight lines in image sequences, *ISPRS Journal of Photogrammetry and Remote Sensing*, 53 (3), 174-182.

Habib A., M. Morgan, and Y. Lee, 2002-a. Bundle Adjustment with Self-Calibration using Straight Lines, *Journal of Photogrammetric Record*, 17(100): 635-650.

Habib A., S. Shin, and M. Morgan, 2002-b. New Approach for Calibrating Off-The-Shelf Digital Cameras, *ISPRS Symposium of PCV'02 Photogrammetric Computer Vision*, Graz, Austria, 9-13 September, Unpaginated CD Rom.

Habib A., M. Ghanma, R. Al-Ruzouq, and E. Kim, 2004. 3-D Modeling of Historical Sites Using Low-Cost Digital Cameras, *XXth ISPRS Congress*, Istanbul, Turkey, Commission 5, SS4-CIPA-Low-Cost Systems in Recording and Managing the Cultural Heritage, pp.570.

Habib A., and M. Morgan, 2003. Linear Features in Photogrammetry, Invited Paper, *Geodetic Science Bulletin*, 9 (1): 3-24.

Habib A., and M. Morgan, 2004. Stability Analysis and Geometric Calibration of off-the-shelf digital cameras, Accepted for publication in the *Journal of Photogrammetric Engineering & Remote Sensing*.

Heuvel F., 1999-a. A line-photogrammetric mathematical model for the reconstruction of polyhedral objects, *Videometrics VI, Proceedings of SPIE*, Vol. 3641, 60-71.

Heuvel F., 1999-b. Estimation of interior orientation parameters from constraints on line measurements in a single image, *Proceedings of International Archives of*

Photogrammetry and Remote Sensing, Thessaloniki, Greece, 7-9 July, 32 (5W11): 81-88.

Hough, 1962. Methods and Means for Recognizing Complex Patterns, U.S. Patent 3,069,654.

Koch K., 1999. Parameter Estimation and Hypothesis Testing in Linear Models, *Second Edition, Springer-Verlag*, Berlin, Heidelberg, 333p.

Kraus K., 1993. *Photogrammetry Volume 1*. Dümmler Verlag, Bonn., pp.277-279.

Kraus K., 1997. Choice of Additional Parameters, *Photogrammetry Volume 2 – Advanced Methods and Applications*, Fred. Dümmlers Verlag, Bonn, pp. 133-136.

Mikhail E., and K. Weerawong, 1994. Feature-based photogrammetric object construction, *Proceedings of the 1994 ASPRS/ACSM Annual Convention & Exposition*, Reno, Nevada. Pages 407-417.

Mulawa D., and E. Mikhail, 1988. Photogrammetric treatment of linear features. *International Archives of Photogrammetry and Remote Sensing*, 27(B10): III383-III393.

Prescott B., and G. McLean, 1997. Line-Based Correction of Radial Lens Distortion, *Graphical Models and Image Processing*, 59(1): 39-47.

Roberts, 1988. A New Representation of a Line, *Proceedings of International Conference on Computer Vision and Pattern Recognition*, pp. 635-640.

Robu D., P. Poncet, R. Zernicke, J. Ronsky, 2004. Assessment of 3D Reconstruction of Scoliotic Human Torso using Imaging Techniques and Stereo-Radiography, *GEOIDE 6th Annual Scientific Conference*, Hull, Quebec, poster presentation.

Shortis M., C. Ogleby, S. Robson, E. Karalis, and H. Beyer, 2001. Calibration Modelling and Stability Testing for the Kodak DC200 Series Digital Still Camera, *Proceedings*

of SPIE on Videometrics and Optical Methods for 3D Shape Measurements, San Jose, CA, 22-23 January 2001, Volume 4309, pp. 148-153.

Tommaselli A., and J. Lugnani, 1988. An alternative mathematical model to collinearity equations using straight features. *Proceedings of International Archives of Photogrammetry and Remote Sensing*, Kyoto, Japan, Commission III, 27 (B3). 842 pages: 765-774.

Tommaselli A., and C. Tozzi, 1992. A filtering-based approach to eye-in-hand robot vision, *Proceedings of International Archives of Photogrammetry and Remote Sensing*, Washington, USA, Commission V, 29 (B5). 950 pages: 182-189.

Tommaselli A., and A. Poz, 1999. Line based orientation of aerial images, *Proceedings of the ISPRS Conference on Automatic Extraction of GIS Objects from Digital Imagery*, Munich, Germany, 32(3-2W5), 143-148.